Velocity dependent rheologies in seismotectonic scale modelling: Characterization and Implementation in a new analogue modelling scheme

Dissertation

zur Erlangung des Grades eines

Doktors der Naturwissenschaften (Dr. rer. nat.)

am Fachbereich Geowissenschaften
der Freien Universität Berlin

vorgelegt von

Michael Rudolf

aus Offenburg

Berlin, 2018

Erstgutachter: Prof. Dr. Onno Oncken
Freie Universität Berlin & GeoForschungsZentrum Potsdam
Zweitgutachterin: Prof. Dr. Francesca Funiciello
Università Degli Studi Roma Tre, Rome, Italy

Tag der Disputation: 08.01.2019

Erklärung

nach §7 (4) der Promotionsordnung des Fachbereichs Geowissenschaften and der Freien Universität Berlin:

Hiermit erkläre ich, dass die vorliegende Dissertation ohne unzulässige Hilfe Dritter und ohne Benutzung anderer als der angegebenen Literatur angefertigt wurde. Die Stellen der Arbeit, die anderen Werken wörtlich oder inhaltlich entnommen sind, wurden durch entsprechende Angaben der Quellen kenntlich gemacht. Diese Arbeit hat in gleicher oder ähnlicher Form noch keiner Prüfungsbehörde vorgelegen.

Berlin, Juni 2018

Zusammenfassung

Große Erdbeben stellen eine signifikante Gefahr für Gebäude und Menschen entlang großer Plattengrenzen dar. Obwohl die absolute Zahl von besonders großen Beben (Moment Magnitude $M_w > 7.0$) klein ist, sind sie für einen Großteil der Todesfälle durch seismische Aktivität und ihre Auswirkungen (Tsunamis, Erdrutsche,...) verantwortlich. Das seltene Auftreten führt zu unvollständigen, statistischen Modellen, welche auf relativ wenigen Datenpunkten basieren. Daher sind die Bedingungen und Prozesse, welche zu Erdbeben dieser Größe führen noch nicht komplett verstanden. Um die bisher bestehenden Erdbebenkataloge zu ergänzen, modelliere Ich experimentell seismotektonische Prozesse. Die Dynamik, Kinematik und Statistik von Erdbeben wird durch vereinfachte Labormodelle von Blattverschiebungen simuliert. Die Experimente werden von analytischen Überlegungen begleitet und sollen zukünftig als Testobjekte für numerische Simulationen dienen. Zu diesem Zweck beschreibt die vorliegende Arbeit die Entwicklung eines neuen Schemas zur Analogmodellierung und gibt Vorschläge zu dessen späteren Verbesserung.

In einem ersten Schritt werden die rheologischen Eigenschaften verschiedener Silikonpolymere untersucht, um deren Eignung zur langjährigen Verwendung und Anwendbarkeit in seismotektonischen Modellen zu prüfen. Silikonpolymere unterschiedlicher Zusammensetzung und Herkunft werden mit modernen, rheometrischen Analyseverfahren auf ihre Tauglichkeit geprüft. Alle getesten Silikone zeigen einen Umschlag von Newtonischer zu exponentieller Rheologie mit steigender Scherrate. Dies führt zu einer verringerten effektiven Viskosität, welches analog zum Verhalten der duktilen Unterkruste ist. Somit verwende Ich eines der Silikone als Analogmaterial für die duktile Unterkruste, welche eine Maxwell-Rheologie unter dem Einfluss von seismotektonischer Deformation zeigt. Desweiteren zeigt sich, dass Silikonöle aufgrund ihrer besonderen Langzeitstabilität und chemischen Ähnlichkeit über mehrere Produktionschargen, besonders gut für die angedachten Experimente eignen.

Um die spröden Reibungseigenschaften von Störungzonen zu modellieren, verwende Ich Glasperlen, welche unter den angepeilten Laborbedingungen einen ausgeprägten Haftgleiteffekt zeigen. Intensive Materialprüfungen legen nahe, dass sehr stark vereinfachte, granulare Störungszonen aus Glasperlen, bereits eine große Vielfalt von verschiedenartigen Gleitphasen (analoge Erdbeben) hervorruft. Mittels Ringscherversuchen wird eine große Menge von abwechselnden Haft- und Gleitphasen simuliert. In Abhängigkeit der Rahmenbedingungen zeigt die analoge Störungszone langsames Kriechen, oszillierendes Rutschen und schnelles Gleiten. In manchen Versuchen kann eine zeitliche Separation von kleinen, langsamen Ereignissen und großen, schnellen Ereignissen beobachtet werden. Dies entsteht sehr wahrscheinlich durch das Zusammenspiel verschiedener, mikromechanischer Prozesse welche die granulare Packungsdichte beeinflussen und verändern. Desweiteren, wird das Wiederauftreten und die Magnitude der analogen Beben stark von transienten und langsamen Prozessen während der Haftphase

beeinflusst.

Die untersuchten analogen Erdbeben, sind häufig mehrere Größenordungen schneller als die Belastungsrate und die Prozesse während der Haftphase. Auch die zeitliche Separation und deren Folgen sind sehr wichtig für das Verhalten des Gesamtsystems. Folglich muss das Experiment kontinuierlich über den gesamten Zyklus überwacht werden. Dies wird durch Bilder und Kraftmessungen gewährleistet, welche während dem Experiment aufgenommen und im Anschluss mittels Bildkorrelation ausgewertet werden. Da die Gesamtdauer eines Experiments zum Teil mehrere Stunden umfasst und die notwendige Aufnahmegeschwindigkeit der Bilder bei über 10 Hz liegt, entstehen während eines Experimentes sehr große Datenmengen, welche nur zu einem geringen Prozentsatz für die weitere Analyse benötigt werden. Um dies zu Vermeiden wurde ein dynamischer Auslösermechanismus entwickelt, welcher die Menge der Daten um fast 95% reduziert. Als Vorlage zum Algorithmus dient die Kraftmessung, welche die Scherkräfte während des Experiments aufzeichnet. In Kombination mit einem dynamisch ansteuerbaren Zwischenspeicher für Bilddaten im Aufnahmerechner werden lediglich die für die Auswertung relevanten Bilder extrahiert und für die Analyse gespeichert.

Die Ergebnisse der Experimente zeigen eine gute Übereinstimmung mit bestehenden Studien und analytischen Beschreibungen der Deformation entlang von Störungszonen. Zukünftig soll das Analogexperiment mit den Ergebnissen aus dieser Studie weiter verbessert werden und numerische Simulationen sollen zur Vergleichsprüfung herangezogen werden.

Abstract

Large earthquakes along lithospheric fault zones associated with major plate boundaries pose a significant threat to structures and people. Although the number of large earthquakes (moment magnitude $M_w > 7.0$) is low, they still account for the majority of fatalities caused by seismic activity and associated consequences (tsunamis, landslides,...). Their scarcity leads to incomplete statistiscal models that rely on few data points. As a result, the conditions and processes that lead to earthquakes of this size are still not completely resolved. To improve the current real-world earthquake catalog, I attempt to model seismotectonic deformation experimentally. Simplified laboratory sized analog models of strike-slip and subduction zones are used to reproduce the dynamics, kinematics and statistics of earthquakes. The laboratory experiments are accompanied by analytical considerations and will serve as a testbed for numerical simulations. For this purpose a new analogue modelling scheme is designed in this thesis and improved based on the findings.

In a first step, the rheological properties of several silicone polymers are studied to evaluate their suitability for long-term laboratory use and usefulness for seismotectonic analogue models. Silicone polymers of differing composition and origin are tested with state of the art rheometric methods. All tested silicones show a transition from Newtonian to power-law rheology with increasing shear rate. As a result, the effective viscosity drops in a similar manner to the lower crust. Consequently, I use one of the tested silicone oils as an analogue for the lower crust, which is assumed to show Maxwell behaviour under the influence of seismic activity. A further advantage of the silicone oils is their long-term stability and chemical similarity over multiple batches.

To model the frictional behaviour of a fault zone I used glass beads, which exhibit rate-and-state-friction under the targeted experimental conditions. Intensive material tests have shown, that a very simplified granular fault zone, only consisting of glass beads, can already show a large number of slip behaviours. Many stick-slip cycles are produced using an annular shear cell. Depending on the experimental parameters, such as loading rate and stiffness, the granular fault zone shows creep, oscillating slip and stick-slip. In some cases a characteristic separation of small slow events and large fast events is observed. This is proposed to be the result of competing micromechanical processes that lead to the reorganization of the granular packaging. Furthermore, the recurrence and magnitude of the larger events is strongly affected by transients and slow events during the interseismic phase.

The analogue earthquakes in this study are several orders of magnitude faster than the interseismic loading rate. The separation of scales which was found for the granular stick-slip events and the resulting effect on the system behaviour requires continuous monitoring of the experiment over the complete seismic cycle. This is done using digital image correlation of images taken during the experiment. Because the duration of each experiment is in the order

of a few hours, and the required acquisition rate for the fastest processes is in the order of several Hz, the amount of data generated per experiment is very high. To circumvent this, a dynamic triggering algorithm is developed to reduce the amount of data by almost 95%. The shear stress during an experiment is used as an input for the triggering system. In combination with a dynamically accessible buffer of images on the monitoring computer, only images that show relevant information are extracted.

A comparison of the experimental findings with existing studies shows a good agreement with natural examples and several analytical descriptions of fault zones. As a next step the experimental setup is going to be developed further with the findings from this thesis and numerical simulations are going to be used for cross-validation.

Contents

Chapter 1

Introduction

1.1 Motivation and Problem Statement

Large lithospheric scale fault zones present a major source of seismic hazard. These fault zones are capable of generating large earthquakes (moment magnitude $M_w > 6.0$) because of their large spatial extend. Although on average 210 earthquakes $M_w > 6.0$ occur per year [Spence et al., 1989], individual regions have much longer recurrence intervals of several hundreds of years. For example, the recurrence time inferred from turbidite sequences along the Cascadia subduction zone (Northwest coast of US), for $M_w > 8$ is roughly between 200 and 400 years where as the world average is 1 year [Gomberg, 2018]. Many of the seismically active regions are within zones of high population density, e.g. San-Andreas Fault (California, USA). As a result, they pose a direct threat to many people worldwide [Allen, 2007, Bilham, 2004]. Therefore, it is important to study the seismotectonic activity of large lithospheric fault zones, to increase the knowledge of the processes and slip behaviour involved.

Earthquakes and lithospheric fault zones show self-similar patterns on different temporal and spatial scales with a complex interplay of parameters and variables [Aki, 1967, Denolle and Shearer, 2016]. This results in complex self-organizing system dynamics which makes it very difficult to model numerically or to describe analytically [Sornette and Sornette, 1989, Caruso et al., 2007]. As the recurrence interval of such large events is very long, not many events are available to make a statistically significant statement about the probability of earthquake occurence in small regions. Most studies rely on paleoseismic evidence and a few historical observations, summarised in earthquake catalogues. As a result it remains ambiguous whether the current statistical models (Burridge-Knopoff, Olami-Feder-Christensen, Gutenberg-Richter, Omori) are suitable to describe and explain the complexity of earthquake occurence [Marković and Gros, 2014]. On a global scale, where many faults interact, the Gutenberg-Richter relation may be a good tool to estimate earthquake recurrence. For a single fault the statistics may differ significantly [Schwartz and Coppersmith, 1984, Ben-Zion, 2008, Wesnousky, 1988]. To make a better estimation of the long-term statistics and evolution of the seismic activity of large lithospheric fault zones, longer time series are needed.

In this thesis I simulate multiple seismic cycles on a single strike-slip fault, to provide a better basis to test recurrence models and numerical codes. I develop two new analogue modelling schemes which are going to be accompanied by numerical simulations in the future. The design of these new modelling schemes requires the search for adequate materials and evaluation of their

usability by measuring the material properties (Chapter 2 & 3). To quantify the experimental results, adequate measuring techniques have to be applied (Chapter 4), and the results have to be compared with natural observations and numerical simulations to verify the integrity of the analogue model (Chapter 5).

1.2 Lithospheric Fault Zones

The following sections outline several characteristics of large lithospheric fault zones that are the objective of this thesis. Firstly, a general introduction to faults is given, followed by a brief description of important aspects of dynamic fault behaviour over time which are going to be used as a basis for the models presented in this thesis.

1.2.1 Faults in the Earth's Lithosphere

The Earth's lithosphere is segmented by a wide range of structural discontinuities, termed faults, along which displacement is possible [Hyndman and Hyndman, 2016, Handy et al., 2007]. Deformation is accommodated regionally through local slip along the fault. These faults are geometric features of varying size (mm to km) and shape. In general, they are approximated as surfaces in a much larger three dimensional block, because they have a much smaller vertical extend compared to their lateral length. Although, being much thinner than the adjacent blocks of host rock, they often alter the bulk properties of the total system. In relation to the surrounding material their physical properties, such as strength or hydraulic transmissivity, can differ dramatically, which makes them a very important part of the total system.

Faults are not homogeneously distributed in the earth's lithosphere, but localise in regions of high strain as a result of strain partitioning and strength reduction due to weakening [Goetze and Evans, 1979, Kirby, 1985]. These fault zones develop on the basis of preexisting zones of weakness, such as material contrasts or areas of high differential stress, over the duration of several millions of years. They consist of a cascade of smaller faults which form a much bigger fault zone, usually along a plate boundary (Figure 1.1) [Eberhart-Phillips et al., 2003].

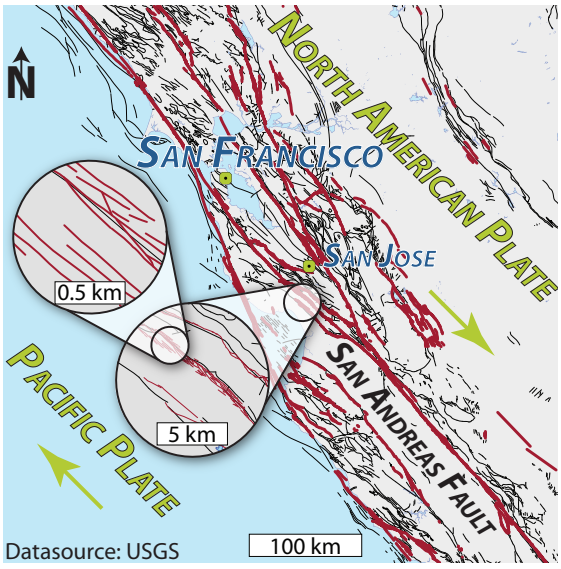

Figure 1.1: A small segment of the San-Andreas fault as an example for the self-similarity of fault networks. Thin black lines show all mapped faults in the region and in dark red active faults (Quarternary) are highlighted. Map data is taken from the open GIS-Webserver by the U.S. Geological Survey and California Geological Survey [2006].

Generally, faults are classified according to the relative motion of the adjacent crustal

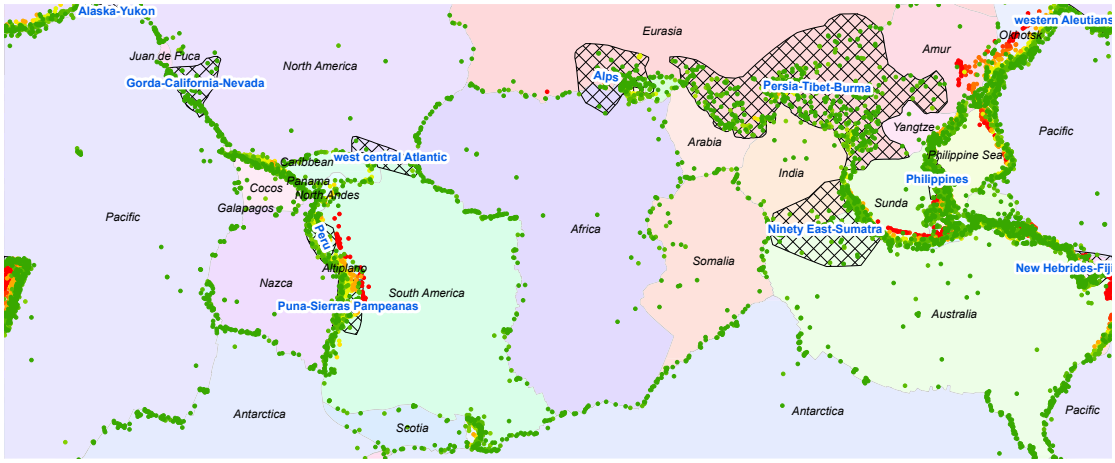

Figure 1.2: Distribution of global seismicity (**M**>5.5) from 1900 to 1999 extracted from the centennial catalogue by Engdahl and Villaseñor [2002]. The hatched areas indicate major zones of crustal deformation, labeled in blue. The colour scale indicates the gradually increasing depth of the earthquakes with green = shallow (<20 km) and red = deep (>500 km). Source map database: Bird [2003], Ahlenius [2014].

blocks. The two endmembers are strike-slip faults, with predominately horizontal, or along strike movement, and dip-slip faults, with predominately vertical, or along dip movement, either normal or reverse. The pure endmembers are rarely found in nature, because the majority of faults show both components and are actually oblique-slip faults. But in most cases one component is dominant and therefore used for terminology.

On a lithospheric scale three types of plate boundaries are found:

Divergent boundaries: Zones of rifting, e.g. center of Mid-Atlantic Ridge or East African Rift

Convergent boundaries: Subduction zones and continental collision, e.g. Andes or Himalaya

Transform boundaries: Zones of relative motion, e.g. San Andreas Fault

All lithospheric scale faults show all kinds of smaller faults, but are dominated by the average trend of the plate boundary. All plate boundaries show seismic activity of different intensity and frequency [Engdahl and Villaseñor, 2002]. This is easily visible in the global distribution of seismicity (Figure 1.2). The main difference in the seismicity of the various plate boundaries is the focal mechanism, indicating the type of fault, and the depth distribution of seismic activity. Subduction zones are characterised by seismic events extending into high depths ($\gg$ 100 km, also called Benioff-zone), especially where the subducted slab is dehydrating or tearing apart. Transform faults show a less deep seismicity and typically do not exceed depths of 100 km. Furthermore, the steep dip of strike-slip zones leads to a strong concentration of seismicity at one location along the fault line, whereas for subduction zones the shallow dip spatially separates the deep seismicity from the shallow part. This thesis is focussed on the shallow to intermediate depth seismicity of transform and continental strike-slip faults including the lower crustal aseismic motion.

1.2.2 Multiscale Character of Fault Slip

In addition to the multiple spatial scales, a fault zone is showing a large variety of slip behaviours with variable velocities and total magnitudes [Bürgmann, 2018, and references therein]. Seismic

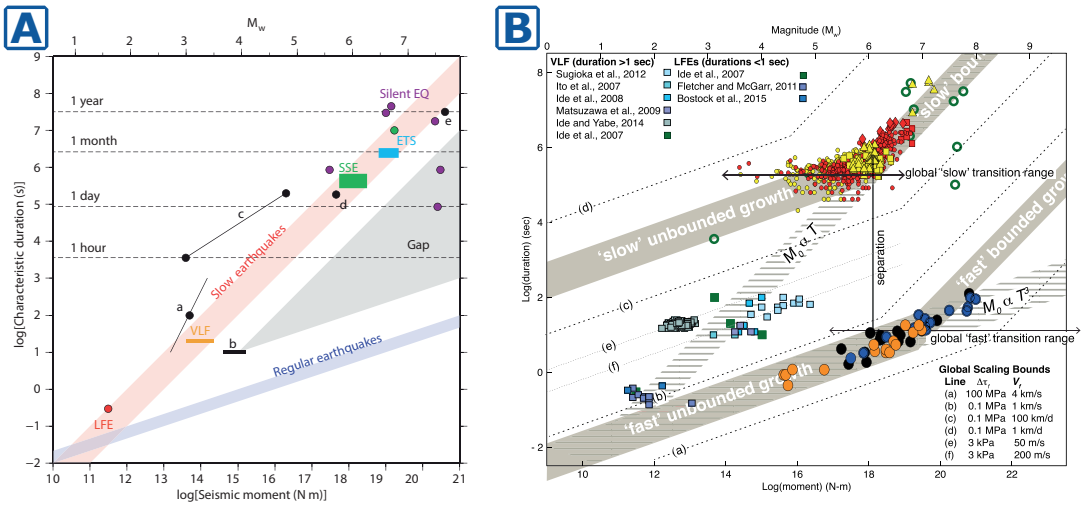

Figure 1.3: Scaling of slip events according to scalar moment M_0 and duration t. (A) Different types of slip events and their scaling behaviour after Ide et al. [2007]. Black bars and dots present averaged observations. Abbreviations used: LFE (low frequency events), VLF (very low frequency), SSE (slow slip events), ETS (episodic tremor and slip), EQ (earthquake). (B) Extension of Figure 1.3A by Gomberg et al. [2016]. The blue to gray coloured squares show VLF and LFE. The black, orange and blue dots represent crustal earthquakes. The red and yellow cluster in the top center are slow slip events from Cascadia (red) and Japan (yellow). Dark green circles and squares are the measurements used by Ide et al. [2007].

slip, referred to as an earthquake, is only a small part of the slip spectrum. Figure 1.3A shows the types of slip, categorised by the seismic moment release over the characteristic duration [Ide et al., 2007, Gomberg et al., 2016]. Ide et al. [2007] found two scaling relationships stating that for fast slip events (e.g. earthquakes) magnitude scales as $M_0 \propto T^3$, whereas slow slip events (e.g. very low frequency events) scale as $M_0 \propto T$, indicated as gray striped areas in Figure 1.3B. Adding new observations to this scaling plot, Gomberg et al. [2016] showed that the differing scaling exponents are an inherent result of rupture growth on a rectangular fault patch under unbounded and bounded conditions.

Similar scaling behaviours for varying locations and varying materials indicate that the underlying mechanism is similar for many different faults. Furthermore, Gomberg et al. [2016] conclude that a continuous distribution of slip modes may be present, but has a bimodal character due to the presence of two distinct power-law scales. This may be the expression of a two-fold rheology of faults, being elastic-velocity-weakening and viscous-velocity-strengthening. In addition, natural observations and laboratory studies show that an individual fault zone can show multiple slip modes, implying a similar physical process [Marone and Scholz, 1988, Ferdowsi et al., 2013].

1.2.3 The Seismic Cycle

Earthquakes usually occur repeatedly on the same fault, very often showing similar characteristics. This is due to cyclic reloading and unloading of the fault as a result of far field stresses [Avouac, 2015, and references therein]. The chronological sequence that ultimately leads to an earthquake is divided into three distinct phases, termed 'seismic cycle' (Figure 1.4) [see also Handy et al., 2007].

Interseismic phase: Time of relative quiescence during which the fault is (partially) locked and elastic strain is building up.

Coseismic phase: Gradual unlocking of the seismogenic patch and sudden release of stored energy in an earthquake through rapid shallow slip.

Postseismic phase: Seismic activity on neighbouring segments and viscoelastic relaxation by slow deep slip activity on ductile segments of the fault.

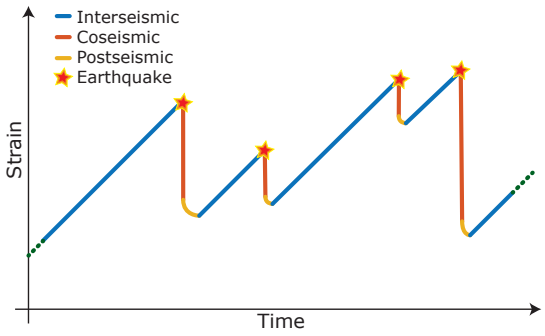

Figure 1.4: Schematic sketch showing the built-up of elastic strain on a single fault during the interseismic phase which is released in an earthquake. This is followed by a non-linear stress decrease originating from the viscoelastic rheology of the ductile part of the fault.

When this was initially observed by Reid [1910], it was thought that this can be used as a simple time-predictable model to forecast the next earthquakes (also see section 3.3.5) which was not possible. Due to extrinsic influences, such as other faults, the stresses on a fault patch and also the material properties may show transient behaviour and therefore a prediction is not possible [Avouac, 2015, Scholz and Gupta, 2000]. Additionally, the fault's surface is segmented into several patches that have different parameters. As a result, a single fault may exhibit earthquakes of different magnitude, depending on the number of rupturing patches, and variable recurrence times [Field et al., 2014]. In some cases the transient behaviour may lead to variable slip modes, e.g. slow slip events that precede major ruptures [Obara and Kato, 2016]. Large lithospheric fault zones are divided into several smaller faults that may branch away from the main direction of strike, leading to a complex network of interacting faults which may synchronise and trigger each other [Scholz, 2010, Scholz and Gupta, 2000].

1.2.4 Mechanics of Large Lithospheric Faults

The slip behaviour of fault zones is mainly defined by the mechanical reaction to deformation, which in turn is described by the material properties. The lithosphere is vertically stratified showing layers of different composition with distinct mechanical properties [Bürgmann and Dresen, 2008]. Continental lithosphere, crust and upper mantle, in a strike-slip environment is characterised by alternating elastic-frictional and viscoelastic-plastic layers (Figure 1.5). The upper crust (0-≈20 km) shows elastic response to stress (controlled by the quartzo-feldspathic composition). Faults are localised to narrow zones with pressure dependent frictional behaviour which are the hosts of earthquakes. The strength of the upper crust is defined by the friction on the active faults and governed by Byerlee's law [Byerlee, 1978]. The lower crust has higher temperatures (300-500°C) leading to a change in deformation mechanism to viscoelastic creep of wet quartz and wet feldspar reducing the effective strength to a much smaller level than in the upper crust. Seismic activity is smaller and limited to microseismicity and tremors. Below the crust the composition changes to mafic, olivine-dominated, material which increases the strength to a much higher level. This results from the rheology of olivine in these conditions, leading to a

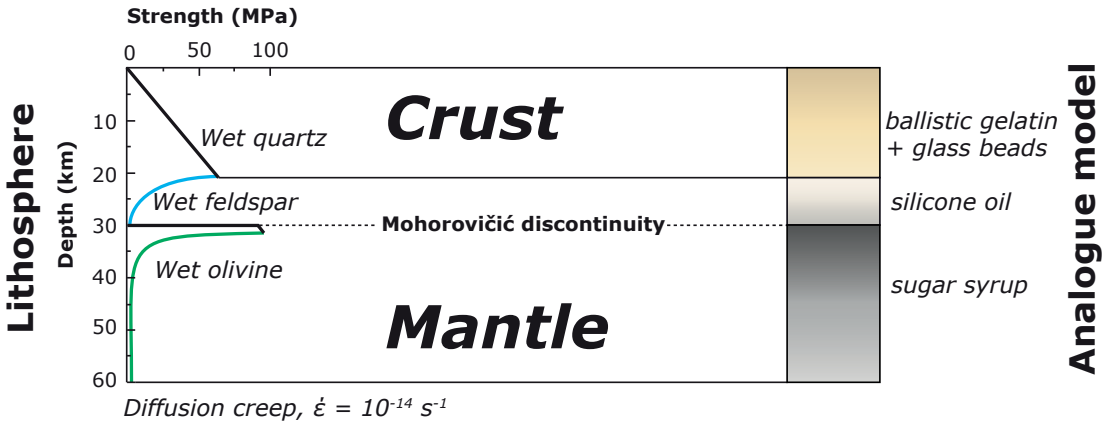

Figure 1.5: Typical strength profile for continental lithosphere under strike-slip conditions and low strain rates [flow law by Bürgmann and Dresen, 2008], and the analogue material equivalent. This profile assumes a lithosphere that is perturbed by large fault zones with a small grain size ('Banana split model'). The upper part of the crust is dominated by elasto-frictional rheology whereas the lower crust shows a gradual decrease in strength with increasing depth. The change from quartzo-feldspathic to olivine dominated material at the Moho increases strength because of the elastic response of olivine under these conditions. This rapidly decays to a very low strength in the lower mantle.

thin brittle layer combined with a highly viscous segment. Below this small strength peak, the strength rapidly decays to a very low level, transitioning into the mainly viscous to viscoelastic rheology of the mantle. The latter strength peak is very prominent in old and relatively cool lithospheres where the upper mantle is much colder than usual, whereas in young lithosphere the mantle is still too hot and contains a small amount of melt (e.g. along oceanic transform faults).

Due to viscoelastic effects in the lower crust and the upper mantle, the rheology is transient in these layers (Figure 1.6) [Bürgmann and Dresen, 2008, Handy et al., 2007]. During large slip events in the upper crust, the strain rate in the lower layers also increases. As a result, the material changes the dominant deformation mechanism and the effective viscosity is decreased by three orders of magnitude in the mantle up to 200 km away from the earthquake for several decades [Freed et al., 2006]. In my models, I simplify the rheology to a combination of three layers (Figure 1.5, right), omitting the upper mantle transient peak.

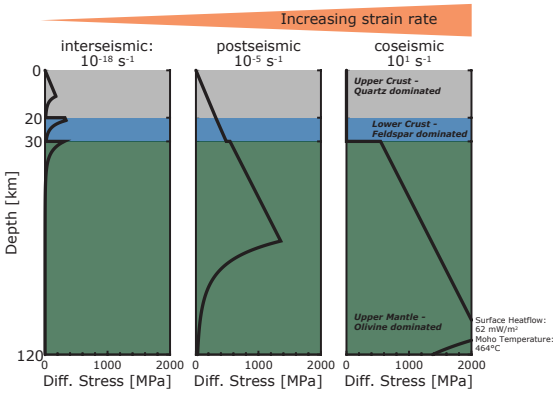

Figure 1.6: Simplified evolution of lithospheric strength with increasing strain rate. The computation assumes a homogeneous change of strain rate over the complete depth range, which of course is not reasonable, but shows the behaviour of the respective material at higher rates. Seismic rates between 10^{-2} and 10^{1} s^{-1} are expected to penetrate into the lower crust, at maximum to a depth of 18 to 20 km for a typical strike-slip fault [Handy et al., 2007]. The diagrams are generated with the XMas-Tree matlab script by S. Brune (pers. comm.).

During the interseismic phase the strength is mainly governed by slow creeping mechanisms,

such as diffusion creep and dislocation glide (non-linear segments in Figure 1.6). At higher shear rates, brittle deformation becomes more dominant which shows a linear increase with depth, because it is temperature independent and linearly scales with normal stress. At coseismic rates, the rate-and-state dependent friction leads to a decay in strength due to the dynamic weakening, resulting in a complete loss of strength in the crustal parts.

1.2.5 Open Questions and Ambiguities

The previous sections give a brief introduction into seismic, statistical and geological observations along lithospheric fault zones. These observations come from several branches of geoscience (e.g. seismology, field geology, remote sensing), each bringing their own limitations into the dataset. As a consequence, a lot of findings are ambiguous or apparently contradicting. In the following, I outline some key issues that are the main driving factors in this thesis.

Seismic vs. Aseismic Fault Slip To estimate the seismic hazard of an active fault, it is necessary to know the partitioning of slip into seismic and aseismic slip [Avouac, 2015]. Of particular interest is the stability of interseismic coupling and long-term loading rate. Recent geodetic observations have shown that the seismic coupling may change over time, resulting in a complex locking pattern that alters the recurrence behaviour of the individual faults in the specific area [Philibosian et al., 2014, Prawirodirdjo et al., 2010, Schurr et al., 2014, Moreno et al., 2010, 2011]. Furthermore, several fault zones show slow slip events (SSEs) which sometimes precede larger earthquakes and are aseismic [Kato et al., 2012, Obara and Kato, 2016]. It is unclear to what extend the spatial and temporal distribution of such events influences the seismic behaviour of a fault. Are they simply the expression of triggered slip due to elevated stresses around seismogenic zones, or are they an inherent component of the seismic cycle [Bürgmann, 2018]? And how big is the influence of the scale of this variability? Are small, local perturbations of the system enough to trigger large scale instabilities?

The Concept of self-organized Criticality In general, the models and equations that describe the empirical data are power-laws, such as the Gutenberg-Richter relation that describes the earthquake frequency as a function of magnitude. These power-laws are assumed to be the expression of a self-organizing critical system (SOC). Many of the widely accepted scaling relations for earthquake time series, e.g. Omori laws, are in accordance with the expected behaviour of a SOC, but are only able to describe the statistical properties of the phenomena [Marković and Gros, 2014]. This also applies to a certain extend to the rate-and-state framework, which is defined as an heuristic concept and the physical explanation for the coefficients in the formulas are unclear [Dieterich, 2007]. However, this does not imply that the models, or some included parameters, are not related to physical processes. In many cases they are clear simplifications of the observed complexity in nature and contain reasonable assumptions. The current descriptions of earthquake time series may therefore provide a good basis to explain some physical phenomena. What remains ambiguous is whether the SOC models are good enough to explain the observables, while being robust against increasing complexity, e.g. by adding interaction between faults, postseismic deformation, or complex networks [Zhang et al., 2009, Marković and Gros, 2014]. And are the findings for one SOC-system applicable to a system that shows similar characteristics as suggested by Uhl et al. [2015] or Denisov et al. [2016]? This is a crucial point for the use of a SOC based analogue model to simulate the seismic behaviour along

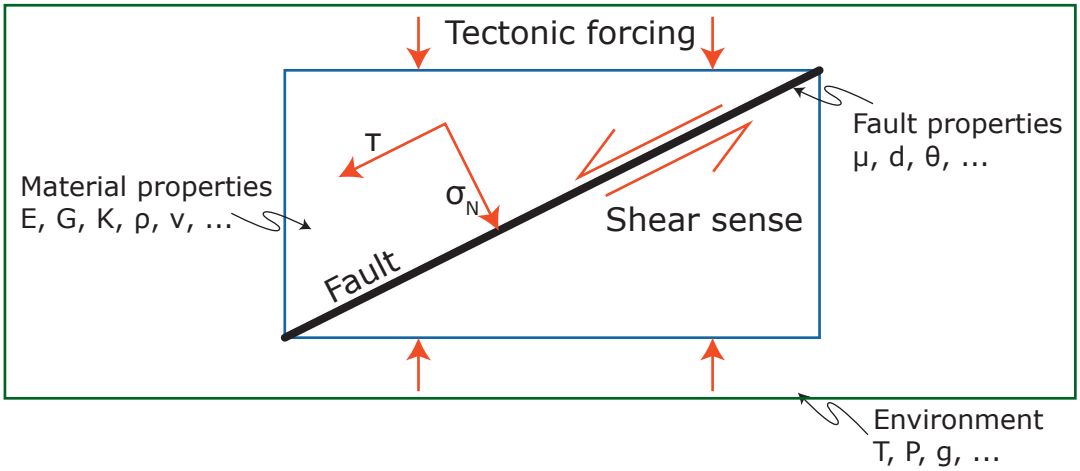

Figure 1.7: Schematic drawing of a single fault system and parameters that are relevant for the description.

large fault zones, because clearly some of the physical processes that act within the model and the prototype are very different.

1.3 The Rate-and-State Framework

Slip in the upper crustal part of a lithopheric fault zone is modulated by the frictional properties of the fault zone. Observations from nature and rock friction experiments indicate a transient non-linear response of stress to velocity increases [Dieterich, 2007]. The rate-and-state framework provides a heuristic approach to approximate the dynamic parameters during an earthquake which depend on slip, slip rate, normal stress, and the history of slip and normal stress.

1.3.1 Friction

To a very simple approximation the shear stress τ along a planar surface is directly proportional to the normal stress σ_N acting upon it (Figure 1.7). With the linear friction coefficient μ:

$$\tau = \mu \, \sigma_N \tag{1.1}$$

Usually, a Coulomb friction model is assumed for brittle failure with a constant coefficient of friction $\mu \approx 0.6-0.7$. For systems that switch from stationary (interseismic) to sliding (coseismic) two different friction types have been established [Rabinowicz, 1951, 1956, 1965]. The friction needed to activate a slip system μ_s, called the static friction, and the friction acting during sliding μ_d, the dynamic friction. Experimental observations show that the strength needed to initiate slip is depending on the hold time (Figure 1.8A) for rock surfaces and fault gouge. This leads to larger peaks in slide-hold-slide tests for a longer loading period (Figure 1.8B). This effect is explained by a time dependent healing effect, that increases the effective contact area of the two sliding interfaces [Marone, 1998, Dieterich and Kilgore, 1994, Beeler et al., 2003].

The friction evolves as a function of time (here expressed in θ), cohesion C and velocity V

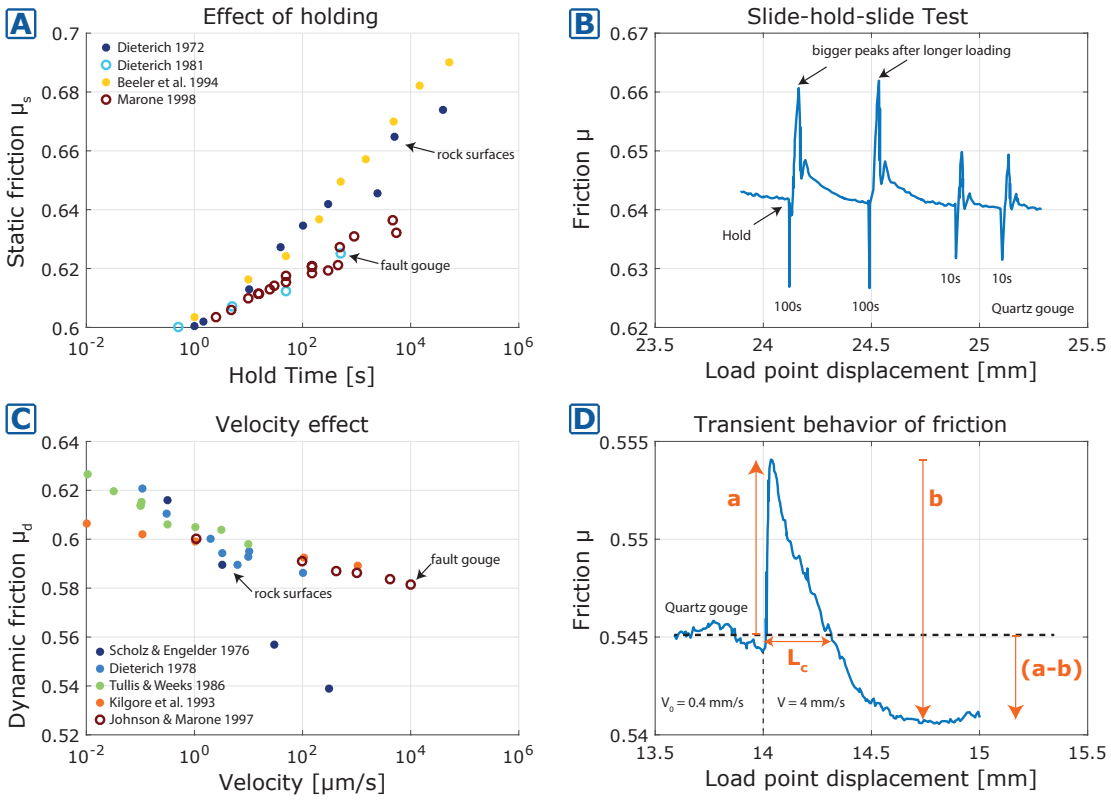

Figure 1.8: Experimental results from slide-hold-slide tests [modified after Marone, 1998]. (A): The strength of the fault zone increases with increasing hold time. The effect is more pronounced for rock surfaces than for fault gouges. (B): Typical curve of a slide-hold-slide test showing reloading peaks after 100 s and 10 s. The peaks are picked and shown as datapoints in (A). (C): Dynamic friction decreases as the sliding velocity increases. This shows the velocity weakening behaviour of fault gouges and rock surfaces. (D): Evolution of friction during a velocity stepping test. When the quartz gouge is sliding under stable conditions a velocity step leads to a transient response in friction. This response is approximated by the frictional properties a, b, and L_c (Equation 1.3).

[Dieterich, 1978]:

$$\tau = [\mu(|V|, \theta)|\sigma_N| + C]\frac{V}{|V|} \tag{1.2}$$

This mechanism has not yet been derived from first principles and therefore remains a heuristic concept, depending on measurements and natural observations. Several experimental studies on various materials show this frictional behaviour which is not limited to rock friction, but also occurs in soils, engineered structures and many abrasive processes [Dieterich, 1979a,b, Ruina, 1981, Heslot et al., 1994, Scholz, 1998].

The evolution of friction is a function of velocity V, normal stress σ_N and the friction parameters a, b, L_c, and θ (Figure 1.8) [Dieterich, 2007, and references therein]:

$$\mu(|V|, \theta) = \mu_0 + a\, ln\frac{|V|}{V_0} + b\, ln\frac{V_0}{L_c}\theta \tag{1.3}$$

The frictional parameters describe several characteristics of the frictional response to a velocity perturbance $\frac{|V|}{V_0}$ and are explained in Table 1.1. $|V|$ here denotes the new absolute velocity and V_0 the velocity for which the reference friction μ_0 has been measured.

Table 1.1: The frictional properties and their respective causes and effects [Dieterich, 2007, Scholz, 2002, Marone, 1998, Heslot et al., 1994].

Variable	**Name**	**Description**
a	Direct effect	Immediate response to a velocity perturbance, may be positive or negative depending on the material.
b	State effect	Difference between peak response, defined by a, and the new steady state level of friction.
L_c	Critical slip distance	Characteristic slip distance over which the friction evolves. This seems to depend on surface roughness and gouge characteristics.
θ	State variable	A characteristic time interpreted to be a measure of contact dynamics [Dieterich and Kilgore, 1996]. Shows a characteristic evolution over time approximated using experimentally derived laws (Equations 1.4 and 1.5).

While the parameters a, b, and L_c are constants related to material properties, the state variable θ shows a characteristic evolution over time. As it has not been derived from physical properties it is usually measured as an empirical approximation of the response of friction to a velocity step. Equation 1.4 is the so called ageing law [Ruina, 1983] and defines θ as the age of the contacts [Linker and Dieterich, 1992]:

$$\dot{\theta} = 1 - \frac{|V|}{L_c}\theta \tag{1.4}$$

This law reaches the new value of friction relatively slowly compared to the slip law (Equation 1.5) which better approximates the initial strong decay of friction in experiments (Figure 1.9).

$$\dot{\theta} = -\frac{|V|}{L_c} ln\left(\frac{|V|}{L_c}\theta\right) \tag{1.5}$$

1.3.2 Stability of Slip and Application to Nature

A system which exhibits rate-and-state dependent friction can be in various states of stability. Each state shows characteristic system behaviour and additionally depends on the system stiffness K and the mean stress σ [Heslot et al., 1994]. The stability is determined using several parameters that can be experimentally derived (Figure 1.10A). A single fault, or a network of faults, can show all stages of stability because the determining parameters are spatially distributed on a fault (Figure 1.10B). This is also expressed in the depth distribution of earthquakes (Figure 1.10C).

1.4 Seismotectonic Analogue Model

Several approaches to model seismogenic plate boundaries exist. Rosenau et al. [2017, and references therein] identify three different classes of analogue earthquake models:

- Highly simplified **'spring-slider models'** provide insight into the influence of friction and serve as a well described basis for many numerical codes.
- **'Fault block models'** with elastic blocks that are in frictional contact that are often used to model rupture dynamics.
- Complex **'Seismotectonic scale models'** with various geometries and scaled properties. These models attempt to model larger fault systems and a variety of phenomena associated to earthquakes (e.g. ground motion, tsunami generation).

In this thesis I use a combination of a fault block model (experiment 'RST') and a seismotectonic scale model (experiment 'BOX'). Both setups use the same materials (gelatine and glass beads) but the fault block model is able to visualize details of slip along a very generalized fault zone over multiple seismic cycles, whereas the seismotectonic scale model shows a more realistic deformation of a free (earth's) surface including slip in a viscoelastic layer below.

As already mentioned, the spatial and temporal scales of seismotectonics along large lithospheric fault zones are much bigger than what can be achieved on a laboratory scale. The total extend of a lithosphere fault zone can span several hundreds of kilometers, with only a fraction of it slipping during an earthquake [Scholz, 2002]. Furthermore, an earthquake or slow slip event happens over a duration of a few minutes to a few days, while the recurrence times can be several hundreds of years [Gomberg et al., 2016].

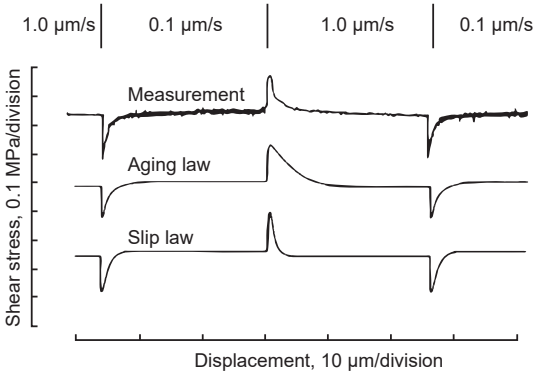

Figure 1.9: Comparison of experimental findings with the two proposed evolution laws for the state variable θ (Equations 1.4 and 1.5). Figure modified after Linker and Dieterich [1992].

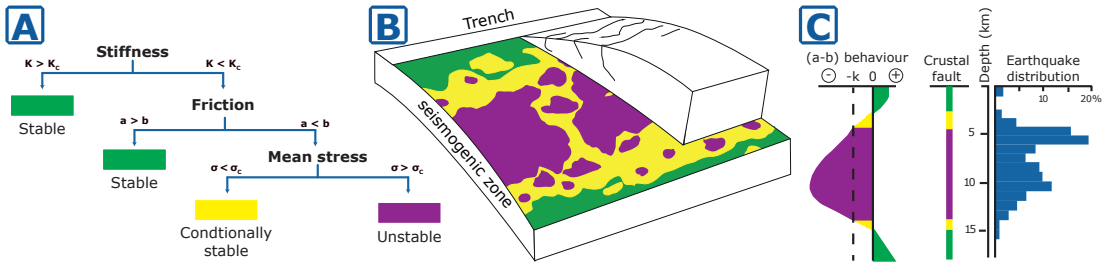

Figure 1.10: Simplified bifurcation diagram for slip stability and distribution of stability zones and related properties. (A): Decision tree for the stability of slip by comparing the system stiffness K, frictional variables a and b, and the mean stress σ on the fault. (B): Schematic distribution of stability regions along a subduction zone. (C): The left graph shows the change of (a-b) over the extend of a crustal fault zone, color coded with the according stability. The left most plot shows the earthquake depth distribution along the San Andreas fault close to Parkfield. [compiled from: Scholz, 1998, Marone and Scholz, 1988, Byrne et al., 1988, Hyndman and Wang, 1993, Bilek and Lay, 2002, Schwartz and Rokosky, 2007, Bachmann et al., 2009]

Several studies, use actual rocks to measure the short-term deformation mechanisms that act in such a fault zone [e.g. Dieterich, 1979a, Tullis and Weeks, 1986, Marone, 1998, Linker and Dieterich, 1992, Lockner and Okubo, 1983, Di Toro et al., 2011, Scuderi et al., 2017, Beeler et al., 2014]. Other experiments derive the long-term rheology of rocks at elevated temperatures and pressures [Bürgmann and Dresen, 2008, Kohlstedt et al., 1995]. These models are suitable to derive and develop the basic framework of the behaviour of rock under laboratory conditions. Both types of experiments, serve as input into various numerical models, providing the equations as well as the parameters for the simulations. The majority of rock deformation experiments do not allow to directly monitor the deformation during the experiments, only the bulk deformation of the sample is measureable. In some cases, acoustic emissions allow for indirect recording of the rupture propagation during the experiment [e.g. Goebel et al., 2014]. This lack of observations is mainly due to technical limitations, as most of the experiments are carried out at pressures in the MPa range and temperatures of more than 200°C.

Analogue experiments use materials that are similar to rocks, but do not need very high pressures or high temperatures to show this behaviour. Depending on the scaling (Section 1.4.1) some of the materials can be chosen to have certain advantageous properties, such as transparency. Additionally, the materials are chosen such that the experiments can be run under ambient conditions at temperatures of around 25°C and easily achievable pressures of less than 20 kPa. Furthermore, they are simplified systems, which may lack certain features that may be important in the prototype. For example my experiments to not include hydromechanical effects because of major technical problems. They are discussed to be major driving forces in reaching the critical failure stress and also the locking patterns in nature [Handy et al., 2007, Moreno et al., 2011]. The use of a hydromechanically coupled model would require an analogue material that is correctly scaled with respect to the rheology of water, which is hard to find [Davy et al., 2010, Bunger et al., 2005].

1.4.1 Scaling and Similarity

The choice of material in the presented setups depends on the material properties of the natural prototype (e.g. elasticity) in combination with desired experimental properties (e.g. transparency). To provide the necessary material characteristics the scaling follows the laws

of similarity defined by Hubbert [1937]. If a model shows geometric, dynamic, and kinematic similarity to the prototype (similitude) it is considered properly scaled and thus the results can be transferred from the model to the prototype [Rosenau et al., 2017]. Scaling the analogue model follows consistent scaling laws that transfer the dimensions (mass, length, time) of the prototype to the model. This is achieved by analytic approaches [Weijermars et al., 1993] or dimensional analysis and resulting dimensionless numbers [Buckingham, 1914]. In this study dimensionless numbers are used for scaling the parameters. In addition, the 'dyadic' time scaling by Rosenau et al. [2009] is used to scale quasi-static and inertial processes differently.

For all parameters the average assumed range of parameters is given to provide a rough estimation of the errors associated with scaling and the uncertainties in quantification of some parameters (Table 1.2). The scaling is carried out with all possible combinations of parameters and resulting minimum and maximum scaling parameters are established. In the following the subscripts 'model' and 'proto', denote the respective values of model and prototype, and an asterisk denotes the scaling factor.

Table 1.2: Overview of key parameters and dimensionless numbers used to scale the model. From the scaling factors all other variables can be calculated, e.g. model recurrence times.

Scaled Variables					Model			Prototype			Scaling Factor	
Parameters		Dimensions			Minimum	Maximum	Unit	Minimum	Maximum	Unit	Minimum	Maximum
Gravity	g		L	T^2		9.81	m/s^2		9.81	m/s^2		1.00
Thickness	d		L		0.05	0.06	m	13	18	km	$2.78 \cdot 10^{-6}$	$4.62 \cdot 10^{-6}$
Density	ρ	M	L^3		1100	1200	kg/m^3	2690	2740	kg/m^3	0.40	0.45
Stresses (lithostatic)	σ	M	L^{-1}	T^{-2}	540	706	Pa	343	484	MPa	$1.12 \cdot 10^{-6}$	$2.06 \cdot 10^{-6}$
Elasticity (Young's Modulus)	E	M	L^{-1}	T^{-2}	100	200	kPa	80	90	GPa	$1.11 \cdot 10^{-6}$	$2.50 \cdot 10^{-6}$
Viscosity	η	M	L^{-1}	T^{-1}	21000	23000	Pa s	10^{19}	10^{22}	Pa s	$2.30 \cdot 10^{-18}$	$2.10 \cdot 10^{-15}$
Time (static)	t_s			T		1.00	s	22.37 min	63.59	d	$1.82 \cdot 10^{-7}$	$7.45 \cdot 10^{-4}$
Time (dynamic)	t_d			T		1.00	s	465.47	600.00	s	$1.66 \cdot 10^{-3}$	$2.14 \cdot 10^{-3}$
Loading rates	v_L		L	T^{-1}	0.05	1.00	mm/s	3.0	15.0	mm/a	$1.05 \cdot 10^{5}$	$1.05 \cdot 10^{6}$
Coseismic slip velocity	v_d		L	T^{-1}	1.67	21.48	mm/s	1.0	10.0	m/s	$1.67 \cdot 10^{-4}$	$2.15 \cdot 10^{-2}$
Dimensionless numbers					Minimum	Maximum		Minimum	Maximum			
Ramberg number	Ra				11.73	40.36		0.94	9161.09			
Smoluchowski number	Sm				$2.70 \cdot 10^{-3}$	$7.10 \cdot 10^{-3}$		$3.80 \cdot 10^{-3}$	$6.00 \cdot 10^{-3}$			
Froude number	Fr				$2.20 \cdot 10^{-3}$	$3.07 \cdot 10^{-2}$		$2.40 \cdot 10^{-3}$	$2.80 \cdot 10^{-2}$			
Cauchy number	Ca				$1.53 \cdot 10^{-8}$	$5.54 \cdot 10^{-6}$		$2.99 \cdot 10^{-8}$	$3.42 \cdot 10^{-6}$			

The first parameter that is used for scaling is the length scale. The thickness of the elastic layer is set to be $L_{model} = 5$ to 6 cm and shall correspond to an elastic thickness of the lithosphere of $L_{proto} = 13$ to 18 km. The resulting scaling factor L^* is $2.78{\cdot}10^{-6}$ to $4.62{\cdot}10^{-6}$.

From the length scale follows the strength scaling, which is defined by the gravitational stress at the bottom of the elastic block. This is expressed in the Smoluchowski number Sm (Equation 1.6) which relates gravity with a characteristic strength, e.g. elasticity. In this case, I assume that gravity is constant, thus g^* =1. Because the material of the upper 15 km of crust is assumed to be granitic ($\rho^{proto} \approx 2.7$ g/cm^3), the strength scaling depends on the analogue material's density ρ^{model}. The choice of material at this stage affects all other scaling relationships, the expected displacements, and velocities of the earthquakes. Several transparent elastic materials are available and have been considered for this study (Section 1.4.2.1).

$$Sm = \frac{\rho g h}{C} \tag{1.6}$$

As a result of these considerations, the material chosen as analogue of the upper crust is a high-concentration pigskin gelatine which has a density of ρ_{gel} =1.10 to 1.2 g/cm^3. The allowed Young's modulus E therefore ranges from 89 to 185 kPa which lies in the experimentally determined range for gelatine (100 to 200 kPa at 23°C). This results in a stress scaling of P^* =$1.11{\cdot}10^{-6}$ to $2.50{\cdot}10^{-6}$. Gelatine is nearly ideal elastic with a phase shift angle of δ >0.95 [Di Giuseppe et al., 2009]. The weak viscous component is not relevant on the experimental time scales and only leads to a weak permanent deformation of the sample after several experimental cycles (3-4 days age).

To calculate the possible viscosities for the viscoelastic layers, the Ramberg number Ra is used (Equation 1.7). This dimensionless quantity relates the gravitational stress with the viscous stresses induced by slow deformation of the viscous layer. This scaling relation is dependent on the assumed viscosity of the lower mantle (10^{19} to 10^{22}Pa s).

$$Ra = \frac{\rho g h^2}{\eta v_s} \tag{1.7}$$

Consequently, the allowed range of viscosities in the model is very high and spans five orders of magnitude. The lowest possible viscosity is around 3 Pa s (e.g. honey), whereas the highest possible viscosity is 900 kPa s (e.g. pitch). For my models I choose a chemically inert silicone oil with viscoelastic Maxwell rheology and a zero-shear viscosity of 22 kPa s (Chapter 2).

The dyadic time scale differentiates a static long time scale T_s^* and a dynamic short time scale T_d^* [Rosenau and Oncken, 2009]. The dyadic time scale is required because on longer time scales, quasi-static gravitational forces are more dominant (high Ramberg number), whereas on short time scales inertia is important. The long time scale is derived by combining the Ramberg Ra and Smoluchowski numbers Sm:

$$T_s^* = \frac{\eta^*}{\sigma^* L^*} \tag{1.8}$$

The silicone viscosity is 22 kPas and as a result 1 second in the model scales to 22.37 min to 63.59 days in nature, depending on the presumed viscosity of the lower crust. Furthermore, the loading rate in the model should lie between 0.13 μm/s and 2.15 mm/s. The rates that are used for this setup are 0.05 to 1.00 mm/s.

In contrast T_d^* is given by the Froude number Fr, using a dynamic velocity v_d, gravity g and

a characteristic length l:

$$Fr = \frac{v_d}{\sqrt{gl}} \tag{1.9}$$

Because gravity is the same for both systems and velocity is given as a length over time, the time scaling is the square root of the length scale:

$$T_d^* = \sqrt{L^*} \tag{1.10}$$

This results in a time scale of 1 second in the model at dynamic velocities is 465 to 600 s in nature. As a rule of thumb we use a threshold for the dynamic velocity which is twice the loading rate of the experiment. Other possible methods to determine the dynamic velocity threshold is to use the value where the number of picked slip events stabilizes [Corbi et al., 2013] which can be problematic if the time series contains slow and fast slip events. First tests with pure glass beads have shown that a broad range of slip events are to be expected, depending on loading rate and stiffness (Section 3).

Another dimensionless parameter that is used to characterize the model is the Cauchy number Ca (Equation 1.11). It relates the dynamic stress of high velocity displacements to the elasticity. The Cauchy number in model and prototype are within the same orders of magnitude (10^{-8} to 10^{-6}).

$$Ca = \frac{\rho v^2}{E} \tag{1.11}$$

As a result from the scaling procedure above, I find which the dimensionless quantities that describe the experimental system, range within the same orders of magnitude for model and prototype (Table 1.2). Therefore, I assume that the experiment shows geometric, dynamic and also kinematic similarity with the prototype under the assumption that all of the governing parameters were considered. All other parameters, such as recurrence times, or rupture velocity, are calculated from the derived scaling relationships. Friction μ and weakening $(a-b)$ are already dimensionless parameters and do not need to be scaled.

1.4.2 Analogue Materials

1.4.2.1 Elastic Material

Gelatine has been chosen as an analogue material because it matches best the requirements that are given by the scaling. Furthermore, it is birefringent which helps to qualitatively describe the state of stress in the material. Other possible materials are described in the following, listing their prime advantages and disadvantages.

Transparent thermoplastics, such as PMMA (acrylic glass), Homalite or polycarbonate, are frequently used as analogues of rupture propagation and also for studying stick-slip dynamics [Rosakis et al., 1999, Schubnel et al., 2011]. The density of these thermoplastics is around 1.2 g/cm^3 which results in a strength scaling of P^* =1.89·10$^-$6. This requires a Young's modulus E_{model} that is six orders of magnitude smaller than for rocks. Typical estimates for the Young's modulus of the upper crust are around 85 GPa (E_{proto} ≈8.5·10^{10}Pa) which means that E_{model} has to be in the kPa range. Consequently, thermoplastics are ruled out due to their elasticity being also in the GPa-range ($E_{polycarbonate}$ ≈2.0 GPa). Additionally, typical rupture speeds are very close to seismic rates and thus not suitable for the analogue model.

Silicone rubbers, which are cross linked and hardened silicone oils (e.g. used in sanitary installations), have a density close to 1.0 g/cm^3 and elasticities in the range of several kPa. They are also available with various elastic properties and are adaptable to the setup. A major drawback is the price of silicone rubbers. During the development of a new experimental setup, the final dimensions and geometries are not known, especially during the first technical tests. This requires the possibility to dynamically change the plate geometry depending on the outcomes. Furthermore, the preparation of clear and transparent silicone rubber blocks of adequate size is rather difficult (e.g. a vacuum chamber for bubble removal). As a consequence, silicone rubbers are preferred materials for a second phase of the experiments when the final setup and geometries are set.

Hydrogels of organic compounds, like Carbopol®, have recently been introduced as an analogue for the non-Newtonian behaviour of rocks [Di Giuseppe et al., 2015]. Carbopol® is a material that has excellent transparency and the physical parameters density (ρ_{carbo} =1.0 g/cm^3) and Young's modulus (E_{carbo} =200 to 1000 Pa) are close to what is required by the length scale. But the overall rheology of Carbopol® does not fit with the required ideal elastic rheology of the upper crust. Carbopol® is a Herschel-Bulkley material that is a solid at rest and becomes a liquid after a yield stress is reached. In liquid state, it is shear thinning and the viscosity decreases with increasing shear rate. This behaviour is more suitable to model the localization in the lower crust, where ductile behaviour is common. Additionally, the preparation requires several safety precautions and some hydrogels are toxic which should be avoided if possible.

Fracture Toughness and Elasticity In some cases slip within a fault increases the stresses at the tip of the fault to values that exceed the yield stress of the surrounding rock. This leads to the formation of new fractures and faults, or extends the existing fracture in direction of the rupture. Because the fracture toughness of gelatine is much lower in relation to the elastic properties, it does not correctly scale with the upper lithosphere. As a consequence, I use pre-cut surfaces with open sides to prevent stress accumulation at the tips of the fault zone. So no new fractures are formed during an experiment, which otherwise would influence the kinematic similarity of the model and the prototype.

1.4.2.2 Frictional Material

Slip in the upper crust is localised in brittle shear zones filled with granular material. They show purely frictional behaviour that is dominated by grain-scale processes and comminution of rock material. As an analogue for crustal fault gouge, I use spherical quartz glass beads with a diameter of 300 to 400 μm. Previous studies demonstrated that glass beads exhibit rate-and-state dependent friction when sheared or compressed [e.g. Mair et al., 2002, Cui et al., 2017]. In my experimental setup the mean stress is much lower (kPa instead of MPa), but extensive tests and a systematic study showed, that the glass beads also show unstable slip behaviour at low normal loads (Chapter 3). Other possible stick-slip materials were also considered, but some show a slip-weakening that is too high (e.g. rice) or are not suitable for use with gelatine (e.g. salt). Especially food based analoge materials, are very susceptible to minor changes in humidity and can vary strongly from one package to the other (e.g. polenta, starch) because the grain size distribution or composition may change. The glass beads are specifically manufactured with constant properties (pure quartz glass) and the grain size distribution does not change much. The very homogeneous grain size distribution and very similar shape of glass beads is

advantageous for stick-slip instability [Mair et al., 2002]. Furthermore, they are not deformed or comminuted during the experiments which leads to constant material properties over long experimental durations.

1.4.2.3 Viscous and Viscoelastic Materials

Several viscous and viscoelastic materials are needed for the analogue model. On the one hand, aqueous glucose solution (Newtonian fluid) detaches the bottom layer of the model from the box, which is comparable to the 'sticky air' in numerical simulations. A viscoelastic paste (thixotropic and shear-thinning, Korasilon paste MB2-285) separates the elastic blocks from the indenter and provides free sliding conditions along the edges. To model the lower crust, which is viscoelastic, I use a silicone oil (Maxwell fluid, Korasilon fluid G30M)

To minimize boundary effects, the BOX setup uses the gelatine blocks together with a viscoelastic layer below. One side of the model is attached to the sidewall of an acrylic tank with viscoelastic paste. The paste allows the block to move parallel to the edge, but its stickiness fixes the gelatine to the sidewall. The opposing edge is fixed to a moveable backwall with the same paste. The two other edges are free surfaces that are in open contact with the surrounding medium (sugar solution). The backwall is moved with two parallel actuators and the force needed to push the plate is measured with an attached force transducer. The possible convergence speed ranges from 200 nm/s to 4 mm/s. Further details of the machine and box are given in [Ritter et al., 2016a].

The layered model is floating in a bath of aqueous glucose solution (ρ =1.3 g/cm^3) which has a higher density than the gelatine (ρ ≈1.1 g/cm^3) and silicone oil (ρ =1.0 g/cm^3). Potassium sorbate (c =1 g/L) serves as a preservative, to prevent the fermentation of the sugar solution. The pH of the solution is equilibrated with citric acid (c ≈1 g/L) to be around pH 3 which is necessary for conservation with potassium sorbate. Both chemicals in similar concentration are in use as additives in the food industry (e.g. in drink syrups) and do not alter the properties of gelatine [Cole, 2000]. As a result the solution is stable over several months. Other non-toxic, heavy solutions or liquids either dry out the gelatine during the experiment (salt water, glycerol) or are too expensive (caesium formate, drilling brine) in the necessary quantities (>100 L).

1.5 Experimental Setup

1.5.1 Fault block model (RST)

This setup is based on the ring shear tester RST.pc01 by Schulze [1994] which is designed to study the frictional properties of granular materials at ambient conditions and pressures typical for industrial applications (< 100kPa), such as silo design. It uses an annular, direct shear cell which is rotated at velocities ranging from 0.05 to 30 mm/min. A lid placed on top of the sample material is held in place by two bars that are connected to force transducers. A moveable weight attached to a lever pulls the lid onto the sample and thereby applies constant normal loading. The publication shown in chapter 3 features this configuration combined with springs to measure the frictional properties of the glass beads that are used in this study. More details on the apparatus are found in Schulze [1994, 2003] and Panien et al. [2006]

For the analogue modelling of earthquakes, the lid and shear cell is replaced by annular gelatine blocks, either planar or conical. This makes the top of the machine transparent and

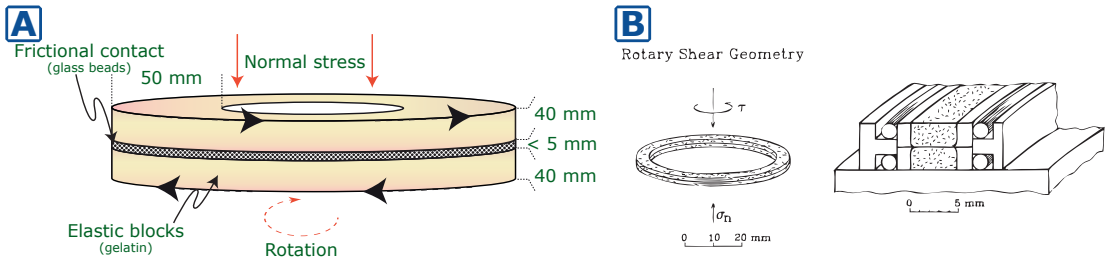

Figure 1.11: (A) Schematic representation of the RST-setup. (B) Schematic representation of a high-pressure rotary shear apparatus [taken from Tullis and Weeks, 1986]

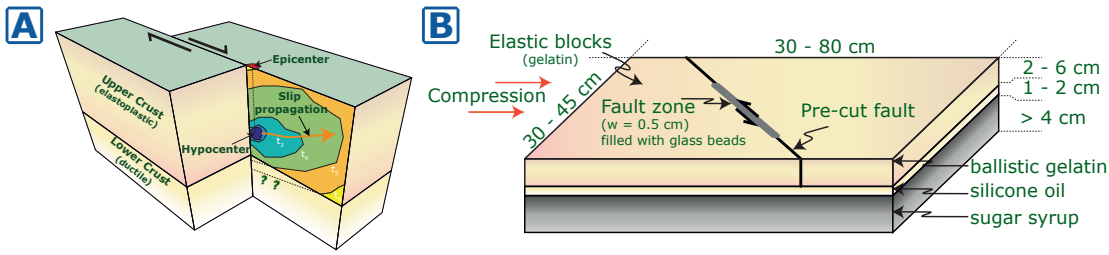

Figure 1.12: Conceptural model of a strike slip fault and experimental representation. (A): Simplified rheological stratification of the upper 20-25 km of continental lithosphere. Earthquakes nucleate within the upper brittle parts of the crust and propagate through the fault zone. The lower crust reacts viscoelastically and shows either brittle failure (for very large shear rates) or postseismic creep. (B): Analogue model representation of the fault system as a predefined single fault zone that is embedded between two gelatine blocks.

ruptures that propagate in the shear zone can be observed with a camera system. Geometrically this setup is very similar to the high-pressure rotary apparatus used by Tullis and Weeks [1986] (Figure 1.11). A more detailed explanation of the setup is found in section 4.3 and 5.1.1.

1.5.2 Scale model (BOX)

The seismotectonic scale model follows the simplified geometry of a strike-slip zone (Figure 1.12). Two elastic blocks are separated by a frictional plastic layer that exhibits rate-and-state-friction with a thinner layer of viscoelastic material below (Figure 1.5). The aim of this setup is to model the surface displacement field associated with a rupture and to validate the model with naturally observed deformation patterns.

The fault blocks are made from a quadratic gelatine block (30 x 30 x 5 cm) with a preformed fault zone. Preforming of the fault zone is achieved with a 24 by 0.5 cm wide teflon sheet that is cast into the block. The rest of the shear zone is cut with a knife. The cut segments are coated with a very thin layer of glass beads, whereas the broader fault zone is completely filled with glass beads. This provides creep on the cut segments, and stick-slip conditions in the seismogenic part of the fault zone.

Geometrically the setup is similar to classical uniaxial compression tests with a predefined zone of weakness, but also features a rheological layering that most of these tests lack. Other analogue studies exist that employ similar geometries or rheological stratification. The foam block models by Brune [1973] provide a strike slip type setting but lack a rheological stratification. Another set of experiments build up on foam blocks lying on top of silicone oil in a Riedel type shear box [Caniven et al., 2015]. The Riedel configuration has a strong boundary condition,

that leads to localization of deformation along the velocity discontinuity. Both types are able to produce stick-slip events and generate scaled analogue earthquakes. In both cases, shear and normal stresses are directly applied to the sample by moving the blocks from the sides with U-shaped holders.

1.5.3 Gelatine Preparation

In this study the elastic lithosphere is modelled by highly concentrated pig-skin gelatine (>20 wt%, 280 Bloom, 30 mesh, by Italgelatine S.p.A.). The gelatine is prepared according to typical standards for ballistic gelatine by soaking the dry gelatine powder in cold, deionized water and then smelting it [Kneubuehl, 2008]. It is recommended to first insert the dry gelatine into the melting pot and then add the cold water. The mixture should be stirred immediately after the water is added, as the gelatine quickly swells forming clumps of dry gelatine. When the mixture has reached a texture similar to stiff fruit mush it is left to swell for one hour at room temperature. Then it is molten within a water bath at 60°C. This preparation technique is different from the preparation procedure suggested by Di Giuseppe et al. [2009] because mixing the dry gelatine with hot water produced too many clumps and also the material tends to burn along the bottom very fast.

The low temperature and the casting as soon as the gelatine is molten, prevents a strong degeneration, and therefore loss of structural strength, during the heating process. Before moulding the blocks, bubbles and foam on the surface are removed with a spatula. This procedure is repeated when the gelatine has been poured into the moulds. Within minutes a thin film of hardened gelatine forms on top of the liquid gelatine. This helps to remove the remaining bubbles. If a thin residual layer of foam is present after removing the majority of bubbles, the surface is sprayed with a small amount of ethanol which lowers the surface tension of the gel and bursts most of the remaining bubbles. Because the gelatine is still very warm, the ethanol evaporates within minutes and does not negatively affect the jellification process. After the gelatine is solidified, it is stored for at least 12 hours at 7°C to ensure full jellification [Di Giuseppe et al., 2009]. In addition to the blocks, three cylindrical samples are cast and measured in an uniaxial compression apparatus to determine the elasticity.

1.5.4 Monitoring and Analysis

Quantification of the experimental results requires continuous monitoring of several parameters during the experiment. To monitor deformation a camera system is used, which acquires images at variable size and framerate. Furthermore, force transducers measure the stresses that act on the models. For the ring shear tester experiments a detailed explanation of the monitoring system, which includes a dynamic framerate trigger, is given in chapter 3 and 4 of this thesis. Here a general and technical description of the camera systems are given, as well as a short introduction to the MatLab^{TM}scripts used to analyze the data. The scripts are found in the data publications associated with the publications in this thesis [Rudolf et al., 2016a, unpublished].

1.5.4.1 Camera system and digital image correlation

The choice of camera depends on the required spatial and temporal resolution. Usually, a high spatial resolution is only possible with a lower temporal resolution and vice versa, mainly due

to the amount of data produced per second of recording. The cameras used for monitoring the experiments are shown in Table 1.3.

Table 1.3: List of cameras that were used for the experiments. The framerate is given for the maximum resolution. For many cameras it is possible to increase the frame rate by decreasing bit depth and spatial resolution, e.g. the MX4M runs at rates over 700 Hz at a resolution of 2048×500 Px and 8 bit.

Name	Spatial resolution [Px]	Max. framerate [Hz]	Bit depth [bit]
Imager MX4M	2048×2048	37 - 185	8 - 12
Phantom VEO-640L	2560×1600	1400	10
Imager SCMOS 5.4M	2560×2160	50	16
Imager proX 11M	4008×2672	5	16

All cameras take grayscale images with the bit depth defining the amount of grayscale values that can be recognized ($8bit = 2^8 = 265$ grayscale values, $16bit = 2^{16} = 65536$ grayscale values). The bit depth of an image should always be used as extensively as possible, i.e. have a very high contrast. This means that white parts of the image should have the highest possible values, and black parts should have values close to zero. By adjusting the exposure time, lighting conditions and surface cover, the optimal settings are found. The contrast should be well above the noise level of the camera sensor.

To calculate the deformation, I am using the digital image correlation (DIC) technique supplied by LaVision DaVis (version 8 and higher). The least squares matching technique (LSM) matches the undeformed image with the deformed image [Fleet and Weiss, 2006, Gruen, 1985]. The images are divided into subsets, starting from one or multiple seeding points. The deformation is estimated by iteratively using an affine transformation of the deformed image until no improvements are made. Afterwards, the new coordinates are interpolated using a bilinear or spline-6 interpolation, because the pixels in the deformed image can lie on non-integer values [LaVisionGmbH, 2017]. Additionally, the resulting vector fields can be post processed with an outlier filter and a smoothing filter. A main advantage of the LSM technique is the faster computing time and the higher spatial accuracy, compared to a Fast-Fourier-Transfomation (FFT) based method. The FFT method is more accurate for very small displacements over a large spatial extend and is less susceptible to noise, because the subsets for calculation can be very big (512x512 px).

1.5.4.2 Vector post processing with MatLab

From the vector fields several parameters can be extracted. For example, the slip area is needed to calculate the moment magnitude of the analogue earthquake. Because the area covered by a displacement vector is known, the slip area can now be calculated with the number of vectors. This gives a more accurate estimation of magnitude than by only measuring the stress drop. Other important features extracted from the vector fields are the displacement profiles along and across the fault.

Furthermore, the annular displacement fields of the RST experiments are projected using a simple Cartesian to spherical coordinate transformation. This results in a good visualization of the rupture process that is similar to typical outcomes of rupture models that were derived from slip inversions (Chapter 5 and A.3). A more detailed explanation of the post processing steps is given in the Appendix A and A.3.

Chapter 2

Rheological benchmark of silicone oils used for analog modeling of short- and long-term lithospheric deformation

M. Rudolf[1], D. Boutelier[2], M. Rosenau[1], G. Schreurs[3] O. Oncken[1]

[1]*Lithosphere Dynamics, Helmholtz Centre Potsdam, German Research Centre for Geosciences (GFZ), Telegraphenberg, D-14473 Potsdam, Germany* [2]*School of Environmental and Life Sciences, University of Newcastle, University Drive, Callaghan, NSW2308, Australia* [3]*Institute of Geological Sciences, University of Bern, Switzerland*

This chapter has been peer-reviewed and published in ***Tectonophysics*** as:
Rudolf, M.; Boutelier, D.; Rosenau, M.; Schreurs, G.; Oncken, O. Rheological benchmark of silicone oils used for analog modeling of short-and long-term lithospheric deformation Tectonophysics, Elsevier, 2016, `https://dx.doi.org/10.1016/j.tecto.2015.11.028`

Individual Contributions:

M. Rudolf planned and performed the research, measured and analysed the data, and wrote the research paper. D. Boutelier and G. Schreurs were involved in the analysis and writing, and provided older measurement data. M. Rosenau was involved in planning the research, analysing the results and writing. O. Oncken was involved in supervising the research and writing.

Keypoints

- Viscoelastic silicone oils are suitable for modeling short and long-term tectonics.
- Temporal scaling can be estimated using Maxwell relaxation and Deborah number.
- Variability and aging effects are small compared to variation in natural systems.
- Continuous assessment of properties is advised for prolonged use of silicone oil.

2.1 Abstract

Analog models of tectonic processes at various scales commonly use silicone polymers to simulate viscous flow in the lower crust and mantle. To achieve dynamic similarity with the natural prototype and to improve comparability between analog models, better knowledge of the rheology of commonly used silicones is required. In this study, we present a rheological benchmark of silicones used in various laboratories. Rheometric tests, including rotational and oscillatory tests, were performed and the viscoelastic behavior of silicone is quantitatively described. We found that silicone oils show a transition from Newtonian viscous to power-law, shear thinning behavior around shear rates of 10^{-2} to $10^{-1}s^{-1}$. The viscosity of chemically similar silicones varied between $2 - 3 \times 10^4$ Pa s. Maxwell relaxation times are about 0.1-0.2 seconds. Such a behavior is able to mimic slow to fast deformation mechanisms in the ductile regime, such as diffusion and dislocation creep as well as viscoelastic relaxation processes. Temperature and aging effects are verified, but can be considered minor with respect to the uncertainty in rheological properties in the natural prototype. Nevertheless, to assure comparability between models and proper scaling the exact properties and conditions should be reported.

2.2 Introduction

Polydimethylsiloxane (PDMS), also known as silicone oil and sometimes simply called silicone, is widely used in the analog tectonic modeling community. It is able to model viscous deformation of rocks in the earth's crust and mantle [e.g. Brun, 2002]. PDMS is a synthetic, transparent polymer which is easy to handle, and is available at a wide range of viscosities. Its rheology is mainly controlled by both the molecular chain structure and chain length.

The rheology of silicones and their applicability in analog models were first discussed by Weijermars [1986a] and Weijermars and Schmeling [1986]. Accordingly, silicones can be considered linear-viscous (Newtonian) under laboratory strain-rates ($< 10^{-2}s^{-1}$), comparable to geological rates in nature ($< 10^{-14}s^{-1}$) and non-Newtonian, i.e. strain rate thinning (power-law behavior) at higher strain rates. Such a two-fold behavior is, in principal, desirable since viscous deforming rocks in general show a strain rate controlled switch in deformation mechanisms and associated rheology [Burov, 2011, and references therein]. The deformation mechanism changes from diffusion creep (Newtonian) at low strain rates to dislocation creep (power-law) at high strain rates. Dislocation creep occurs, for example, in lower crustal mylonitic shear zones, facilitating both the original and sustained strain. Dislocation creep is also inferred to control viscoelastic relaxation of the lower crust or upper mantle after large earthquakes [e.g. Bürgmann and Dresen, 2008]. Most of the previous analog tectonic models using silicones have been designed to simulate longterm tectonic deformation processes where Newtonian behavior

is adequate [e.g. Davy and Cobbold, 1991, McClay et al., 1998, Wu et al., 2009, Dooley and Schreurs, 2012]. The recent interest in simulating geologically "fast", short-term processes such as seismic cycle deformation [e.g. Rosenau et al., 2009, Corbi et al., 2011, Caniven et al., 2015], requires quantification of the non-Newtonian and viscoelastic properties of silicone.

Ten Grotenhuis et al. [2002] were the first to demonstrate the full rheological complexity of silicone. Accordingly, the power-law behavior in silicone at high strain rate is linked to molecular viscoelastic relaxation processes mimicking dislocation creep and relaxation processes in nature. With this perspective in mind, we present a new assessment of the rheological properties of silicone oils by means of a rheological benchmark study using a variety of silicones employed in different laboratories. We use state-of-the-art rheometry to constrain a range of rheological variability amongst the different silicones used by the laboratories. Moreover, we study the viscoelastic behavior of silicones over a wide range of strain rates to lay a foundation for silicone use in short- to long-term "cross-scale" analog models. This paper is a companion to a benchmark study on granular materials [Klinkmüller et al., 2016] in the same GEOMOD 2015 conference special issue. As such, we neither attempt to give a review on the use of silicones in analog models nor do we present a rigorous material science paper. Instead we present and briefly discuss a wealth of new data on silicones used by the community to establish comparability between the models from different laboratories. The wide range of strain rates employed in this benchmark study will further explore the suitability of silicone in analog models of the seismic cycle, associated viscous deformation, and other geologically fast processes.

2.3 Material and sample description

PDMS is a chemically inert and non-toxic silicone oil that has numerous uses in industry, cosmetics and pharmacy. Polymerization of dimethyldicholorsilane ($Si(CH_3)_2Cl_2$) with water produces chains of dimethylsiloxane [$SiO(CH_3)_2$] which is the main constituent of PDMS [Mark et al., 2005]. The average length of the polymer chains defines the resulting viscosity of the silicone oil. Longer polymers tend to entangle faster when sheared and therefore result in a higher viscosity. The rheological behavior over a broad shear rate regime is mainly the result of the polymer length distribution. Furthermore, polymer chains can be cross-linked with additives, such as boric acid, to produce different rheological behaviors. Therefore, it is important to state which type and brand of PDMS was used because this material is available in many different varieties.

The samples tested in this study consist of eight different polymers from seven different laboratories (Table 2.1). Five of the eight samples are pure silicones: SGM36, G30M, KOR2000, PEN219, and SIL4-2901, whereas the remaining three samples are filled silicones. Two of the filled silicone samples are so-called silly putties of different color (black SIPk and yellow SIPy) and the third one is a special shock absorber material (listed as "SHOCK").

The most commonly used PDMS in analog modeling is Dow Corning SGM36, which is a viscoelastic fluid (see Weijermars [1986a] for a comprehensive summary of the physical properties). SGM36 is chemically equivalent to SILASTIC® 4-2901 that is now available as XIAMETER® RBG-0901. Five samples of SGM36 from different laboratories were tested. To distinguish the origin of the samples, a three letter abbreviation is added to each sample (Table 2.1).

G30M and KOR2000 are both representatives of KORASILON® M-type fluids produced by

K. Obermeier GmbH. They have a shorter molecular length and therefore lower viscosities than SGM36 [Obermeier, 2014].

Silly putties are dimethyl- and polydimethylsiloxanes that have been cross-linked with boric acid at elevated temperatures [PBDMS in Weijermars and Schmeling, 1986]. Silly putties are commonly available as toys of various colors and properties (e.g. magnetic or phosphorescent). We tested yellow and black silly putty called "Intelligente Knete / Thinking Putty" by Crazy Aaron Enterprises Inc. These materials are viscoelastic with a very pronounced transition from viscous to elastic. The third filled silicone that was tested, SHOCK, is an ingredient for shock absorbing materials. It is normally used for flexible protective gear for motorcyclists. The material is called d3o® and was provided by D3O Lab.

The shelf life for most of the materials is given as 24 months. The samples from outside GFZ were collected from the different laboratories and first tested in 2008 in the framework of the GEOMOD conference of that year. At the time of collection, the samples had been already stored for an unknown period in the various laboratories. Since then, they have been stored at GFZ Potsdam in closed containers under dark and dry laboratory conditions. These samples are remeasured in 2015. Therefore, all samples from which we provide the results of this paper have exceeded their official shelf life by at least 6 years. This might be viewed as problematic because of potential material-aging controlled property changes. We argue instead that the samples actually reflect realistic material states in analog laboratories where expensive materials like PDMS are usually stored and re-used over multiple years. Furthermore, the current measurements in comparison to the original 2008 measurements can give a valuable insight into the effect of aging on decadal scale. To further constrain the aging effect we additionally compare the results from two batches (2009 and 2011) of G30M that are in use at GFZ Potsdam under different storage conditions.

2.4 Rheometric methods

In most studies the viscosity is examined as the main rheological parameter [see references in Ten Grotenhuis et al., 2002]. Ten Grotenhuis et al. [2002] were the first to fully describe the rheology of polymers by means of its dynamic moduli, i.e. the so called storage modulus G' (describing the elastic behavior) and the loss modulus G" (describing the viscous behavior), under varying strain and shear rate conditions. Here we adopt the methodology of Ten Grotenhuis et al. [2002] and obtain (1) the shear rate and temperature dependency of viscosity at low shear rates with a controlled shear rate test and (2) the dynamic moduli with oscillatory tests.

2.4.1 Rotational tests

For shear rates below $\dot{\gamma} = 10^{-2}s^{-1}$ controlled shear rate (CSR) tests are used. During a CSR test, the sample is sheared at a given shear rate and the corresponding shear stress τ is monitored. A viscosity curve is calculated which shows the viscosity over the given shear rate regime. The zero-shear viscosity η_0 is approximated by the logarithm of the viscosity equation with the power-law coefficient n:

$$log_{10}\tau = n\, log_{10}\dot{\gamma} + log_{10}\eta_0 \tag{2.1}$$

A variation of the CSR test is the temperature sweep. The sample is sheared at constant shear rate of $\dot{\gamma} = 0.01s^{-1}$ and the temperature is increased from 10 °C to 40 °C to show the temperature dependence of the material under typical experimental conditions. The duration of the measurement is 300 s per point and the whole temperature range is covered by 10 points.

The temperature dependency of viscosity is described by an Arrhenius-style equation using a hypothetic viscosity at infinitely high temperature $\eta_{T\to\infty}$, the universal gas constant $R = 8.31445\frac{J}{mol\,K}$ and the activation energy E_A (Equation 2.2). The activation energy describes the energy needed for the molecules to change their place in the molecular structure.

$$\eta(T) = \eta_{T\to\infty} \cdot e^{\frac{E_A}{RT}} \tag{2.2}$$

With exception to the temperature sweep tests, all measurements have been conducted at 23°C. For the rotational experiments the shear rate $\dot{\gamma}$ ranges from $10^{-6}s^{-1}$ to $10^{-2}s^{-1}$.

2.4.2 Oscillatory tests

Oscillatory tests, also called 'dynamic mechanical analysis', are used to determine the properties of all types of viscoelastic materials. The measuring procedure allows an easy and fast determination of the rheological behavior and characteristic parameters at variable shear stresses and shear rates [Mezger, 2006].

The basic underlying principle is to apply a sinusoidal oscillation of shear strain γ_A with a specified angular frequency ω to a sample. The angular frequency describes the frequency of the oscillatory excitation which results in a deformational response. The oscillatory motion can be described as a function of shear strain over time $\gamma(t)$ (Figure 2.1 A-C). The applied shear strain γ_A leads to a sinusoidal shear stress curve $\tau(t)$ that is needed to deform the sample. The equations that describe γ and $\dot{\gamma}$ as a function of time during the experiment are as follows [Mezger, 2006]:

$$\gamma(t) = \gamma_A \, sin\, \omega t \tag{2.3}$$

$$\dot{\gamma}(t) = \gamma_A \, \omega \, cos\, \omega t \tag{2.4}$$

For ideal elastic materials the resulting shear stress curve is described by Hooke's law [$\tau(t) \propto \gamma(t)$] which describes an immediate deformational response to stress. This means that the shear strain curve is in phase with the shear stress curve (Figure 2.1 A). In contrast to ideal elastic materials, ideal viscous materials show Newtonian flow behavior [$\tau(t) \propto \dot{\gamma}(t)$] meaning that they show a time delayed response to deformation. As a result the shear strain curve is out of phase with the shear stress curve but in phase with the shear rate curve (Figure 2.1 B). Viscoelastic materials show a mixture of both behaviors (Figure 2.1 C)

The dual behavior of a viscoelastic material leads to two parameters that describe the viscous and elastic proportion on the overall response to shear strain. The elastic part is represented by the storage modulus G' which is a measure of the energy stored in the system during deformation. The viscous part is denoted by the loss modulus G" showing the energy that is lost during permanent deformation [Nelson and Dealy, 1993]. Both can be combined using the imaginary number i to give the complex dynamic modulus G*. It is defined by the storage modulus G' and

Table 2.1: Materials used in this study and their laboratory of origin.

Laboratory	Material	Abbreviation
Federal University of Ouro Preto	SGM36	UOP
German Research Centre for Geosciences	G30M	GFZ
	SHOCK	GFZ
	SIPk	GFZ
	SIPy	GFZ
Royal Holloway University	SGM36	RHU
University Bern	G30M	UBE
	KOR2000	UBE
	PEN219	UBE
	SGM36	UBE
University Lille	SGM36	LIL
University of Toronto	SIL4-2901	UTO
University Parma	SGM36	UPA

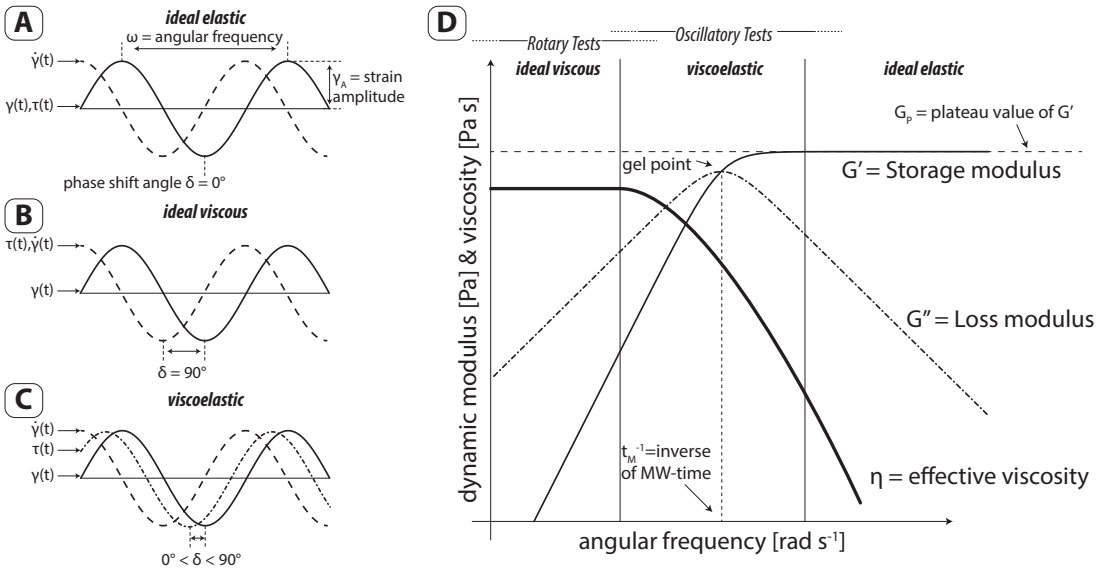

Figure 2.1: The left column (A to C) shows the shear strain $\gamma(t)$, shear rate $\dot{\gamma}(t)$, and resulting stress $\tau(t)$ during a frequency sweep test. The right image shows a theoretical frequency sweep test including the usual shear rate ranges for the different tests. (A) For ideal elastic behavior the stress is in phase with the shear strain. This is due to the immediate elastic response to deformation. (B) For ideal viscous behavior the stress is in phase with the shear rate resulting from the time-delayed deformational response. (C) For viscoelastic behavior the stress curve is out of phase with both shear strain and shear rate. The phase shift between the stress curve and shear strain curve is showing the viscoelastic character (Table 2.2). (D) Theoretical behavior of a simple Maxwell material during a frequency sweep test.

the loss modulus G" in the complex plane:

$$G^* = G' + iG'' \tag{2.5}$$

For rheological characterization the relation between $\tau(t)$ and $\gamma(t)$ is examined. The phase shift between $\tau(t)$ and $\gamma(t)$ is described as the phase shift angle δ which is 0° for ideal elastic and 90° for ideal viscous behavior (Table 2.2). Viscoelastic (VE) materials show both behaviors simultaneously which results in a phase shift between 0 and 90° (Figure 2.1 C). The phase shift can be calculated using the loss factor $tan\,\delta$ which is the ratio between storage and loss modulus:

$$tan\delta = \frac{G''}{G'} \tag{2.6}$$

Table 2.2: Material parameters and their values in the respective rheological regime.

ideal viscous flow	viscoelastic liquid	gel point	viscoelastic gel or solid	ideal elastic solid
$\delta = 90°$	$90° < \delta < 45°$	$\delta = 45°$	$45° > \delta > 0°$	$\delta = 0°$
$tan\delta \to \infty$	$tan\delta > 1$	$tan\delta = 1$	$tan\delta < 1$	$tan\delta \to 0$
$(G' \to 0)$	$G'' > G'$	$G' = G''$	$G' > G''$	$(G'' \to 0)$

The value of the loss factor characterizes the behavior of the material at a given shear strain or shear rate (Table 2.2). This is especially important when using analog models that span a range of shear rates. For $tan\,\delta > 1$ the material shows a VE liquid behavior and for $tan\,\delta < 1$ the material shows VE solid behaviors. $tan\,\delta = 1$ is the so called gel point which denotes the transition between the two behaviors.

Figure 2.1-D depicts the typical behavior of a Maxwell type viscoelastic material like PDMS. Such a material is a nearly ideal viscous liquid at low frequencies and a nearly ideal elastic solid at high frequencies (Figure 2.1-D). A transitional, viscoelastic regime is present at intermediate frequencies. The effective viscosity decreases as the elastic response starts to gain importance.

2.4.2.1 Amplitude sweep

Amplitude sweeps are used to determine the limit of the linear viscoelastic range (LVE-range) γ_{LVE}. The LVE-range is the strain regime where Hooke's and Newton's law are valid. Outside the LVE-range the deformation mechanisms of silicone oils are complex and may depend on deformation history [Ten Grotenhuis et al., 2002, Boutelier et al., 2008]. Therefore, the material cannot be described with viscosities and elasticity.

During the amplitude sweep tests the strain is increased from $\gamma_A = 10^{-4}$ to a maximum of 10^3 at an angular frequency of $\omega = 1rad\,s^{-1}$.

γ_{LVE} is determined by oscillatory tests with successively increasing strain amplitudes at constant angular frequency and temperature. For low strain values the dynamic moduli curves show a linear behavior. Increasing the strain amplitude above γ_{LVE} leads to a non-linear decrease in G' and G". Following the set of instructions given in Di Giuseppe et al. [2012] γ_{LVE} is determined as the value for G' where the next value deviates more than 10% from the value that is predicted from a linear approximation of the constant γ values.

2.4.2.2 Frequency sweep

To determine the shear rate dependency of G' and G" and therefore of the viscoelastic behavior, frequency sweeps are performed. During a frequency test the material is sheared at varying shear rates to a constant strain. These tests are suitable for high shear rates that are above $10^{-2}s^{-1}$ because the forces are lower than for a rotational test in the same shear rate range. Furthermore, the viscoelastic behavior for different shear rates is determined from the loss factor $tan\,\delta$.

Frequency sweep tests are conducted with $\gamma = 0.05$ which is in the linear viscoelastic range for all measured silicone oils. γ is reduced to 10^{-3} for the SHOCK material because it has a lower LVE range. The angular frequency ω varies from $0.05\,rad\,s^{-1}$ to $500\,rad\,s^{-1}$.

As a result from the frequency sweep the gel point of the silicone can be calculated. This is done by interpolating the phase angle between the measurement points. The use of a spline interpolation preserves the slope of the curve. The interpolation reduces the step size and allows a more precise localization of the gel point. The procedure is done using a MATLAB algorithm that searches for the first interpolated point where tan $\delta =< 1$.

2.4.3 Rheological models

To analyze the measurements from rotational and oscillatory tests we use two constitutional models: the Cross model for generalized Newtonian fluids and the Maxwell model for viscoelastic fluids.

2.4.3.1 Cross model

The Cross model for generalized Newtonian fluids can be used to evaluate shear rate dependency of viscosity of unfilled polymers [Mezger, 2006]. Using the Cox-Merz rule [Cox and Merz, 1958] it is possible to combine the effective viscosity from the CSR tests and the complex viscosity from the frequency sweep. The resulting $\eta(\dot{\gamma})$-curve is fit by the Cross equation:

$$\eta(\dot{\gamma}) = \frac{\eta_0}{(1 + \lambda_c\dot{\gamma})^p} \tag{2.7}$$

The plateau value of the viscosity at low shear rates η_0 is an approximation of the viscosity at zero-shear. The transitional shear rate $\dot{\gamma}_c$ from Newtonian to power-law is λ_c which is provided by its reciprocal $\dot{\gamma}_c$. The decrease of viscosity at high shear rates is characterized by a power-law coefficient p. A Cross fluid shows a Newtonian behavior below $\dot{\gamma}_c$ and power-law behavior beyond $\dot{\gamma}_c$.

2.4.3.2 Maxwell model

To describe viscoelastic behavior of a fluid the simplest model is that of a viscous damper (dashpot) coupled in line with an elastic module (spring) known as the single Maxwell element. In a dynamic test of a single Maxwell viscoelastic fluid the dynamic moduli are defined by:

$$G' = G_p \frac{\omega^2\lambda_M^2}{1 + \omega^2\lambda_M^2} \tag{2.8}$$

$$G'' = G_p \frac{\omega\lambda_M}{1 + \omega^2\lambda_M^2} \tag{2.9}$$

A Maxwell material is characterized by the Maxwell relaxation time λ_M which is the ratio of zero shear viscosity η_0 and the shear modulus G_p. The Maxwell relaxation time λ_M is calculated using the inverse of the angular frequency at the gel point because at the gel point $G' = G''$ and from equations 2.8 and 2.9 follows:

$$\lambda_M = \frac{1}{\omega} \tag{2.10}$$

At time periods shorter than λ_M the material is dominated by elastic behavior while at time periods above λ_M the material is dominated by viscous deformation. The relation between observational time period and λ_M is known as the dimensionless Deborah number:

$$De = \frac{\lambda_M}{t_p} \tag{2.11}$$

A single Maxwell material is characterized by a single Maxwell element with one viscosity and one elastic modulus. This is a strong simplification of the actual rheology of most studied materials, especially if a wide range of strain rates is tested. In detail, the silicone oils are better characterized by a generalized Maxwell model being a number of single Maxwell elements coupled in parallel. Such a more complex material does not have a single relaxation time but a spectrum of relaxation times depending on the length distribution of molecular chains. The generalized Maxwell model is repeatedly used in numerical geodynamic modeling [e.g. Del Negro et al., 2009] and is incorporated in commonly used geodynamic software, such as PyLith [Aagaard et al., 2007]. Commonly, two or three Maxwell relaxation times are used to model the relaxation of the individual rheological layers in the model, e.g. one λ_M for the upper mantle. The Maxwell relaxation time spectrum can be obtained from the measurements using software such as ReSpect [Takeh and Shanbhag, 2013]. For this study, we exclude the application of a generalized Maxwell model into the scaling which is beyond the scope of our aims (detailed relaxation time spectra for each sample, along with the single Maxwell model result, are available in the supplementary material).

2.5 Rheometric setup

The rheological properties of the samples are determined using oscillatory and rotational tests on a Physica MCR301 rheometer produced by Anton Paar GmbH. For the pure silicone oils a parallel-plate setup with sandblasted surfaces is chosen (Figure 2.2). Only the filled silicones are tested with serrated parallel-plates because they lose their adherence to the sandblasted plates at high shear rates. The diameter of the plates is either 25 mm or 50 mm with a measuring gap of 1 mm.

The dimensions of the setup depend on the general viscosity of the material. Larger diameters have a higher accuracy because more material is sheared and therefore stresses are higher. However, in the case of highly viscous materials, the shear stresses may exceed the stress limit of the rheometer. The filled silicone oils are tested with a diameter of 25 mm, while all others are tested using a diameter of 50 mm. This size variation is taken into account by the rheometer and the measured parameters are calculated accordingly.

After the sample has been loaded, the gap is almost closed to final gap distance, before the protruding sample material is cut off and the gap distance is decreased to the final position (Figure 2.2). This ensures optimal filling of the setup. To remove most of the residual stresses

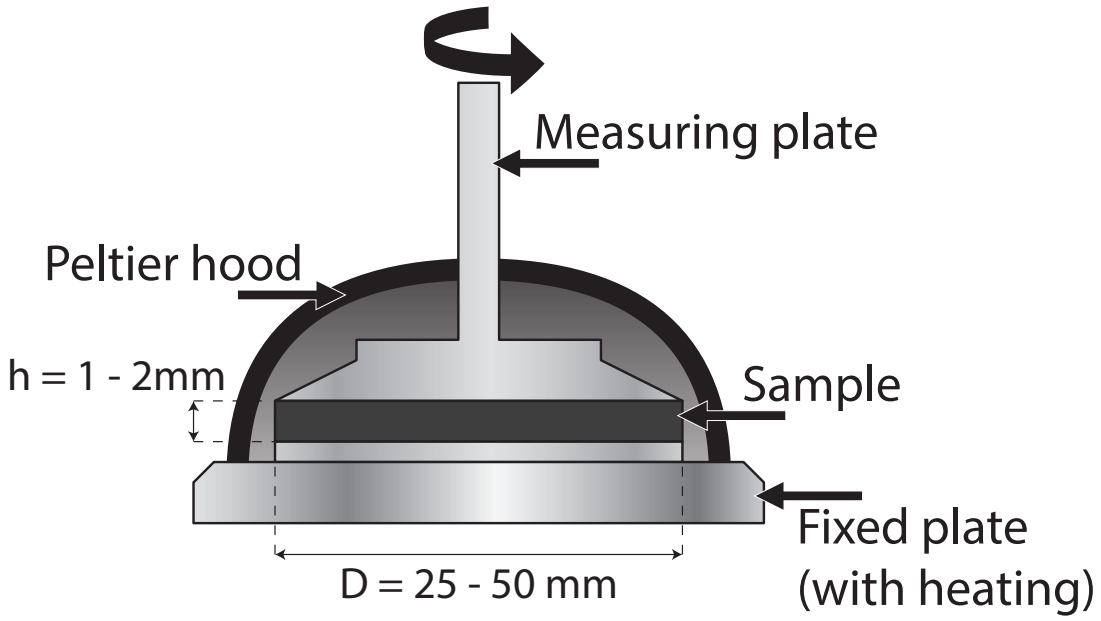

Figure 2.2: Schematic drawing of the rheometer setup. The sample material is squeezed between the two plane-parallel plates. The temperature is controlled by a water and air cooled Peltier element located inside the hood and within the lower plate.

and to reach a homogeneous temperature distribution, the sample is allowed to rest for 300 s. The relaxation in the measuring gap is dependent on the Maxwell relaxation time, which is poorly determined at this stage.However, from measurements done by Ten Grotenhuis et al. [2002] a relaxation time in the order of a few tens of seconds can be estimated for SGM36. Additionally, the rheometer is monitoring the normal stress acting on the sample. After 300 s the stresses have decayed below 0.01 N. Thus a nearly complete relaxation of the material within 300 s can be assumed.

Generally, the rheometer is set to automatically determine the optimum measuring time per point, resulting in a very high precision and effectiveness for an individual point measurement. Only for the temperature sweep tests a predefined time (300 s) was used to ensure equilibration with the temperature conditions at each point.

Each test is repeated three times with a new sample for each run. For each series the mean value and standard deviation is calculated. The standard deviations are generally smaller than the markers in the plots. So they have been omitted to make the plots easier to read.

2.6 Results

2.6.1 Shear rate dependency of viscosity

Almost all materials show a near-linear relationship between stress and shear rate for $10^{-5} < \dot{\gamma} < 10^{-2}\, s^{-1}$. Using equation 2.1 this results in a power-law coefficient of $n \approx 1$ (Table 2.3). The viscosity is constant and therefore exhibits a Newtonian behavior (Figure 2.3 - column a). Only the silly putties SIPk and SIPy show a lower power-law coefficient of $n = 0.973$ to 0.975 (Table 2.3). This leads to a slightly decreasing viscosity during the test (Figure 2.3 - 4a).

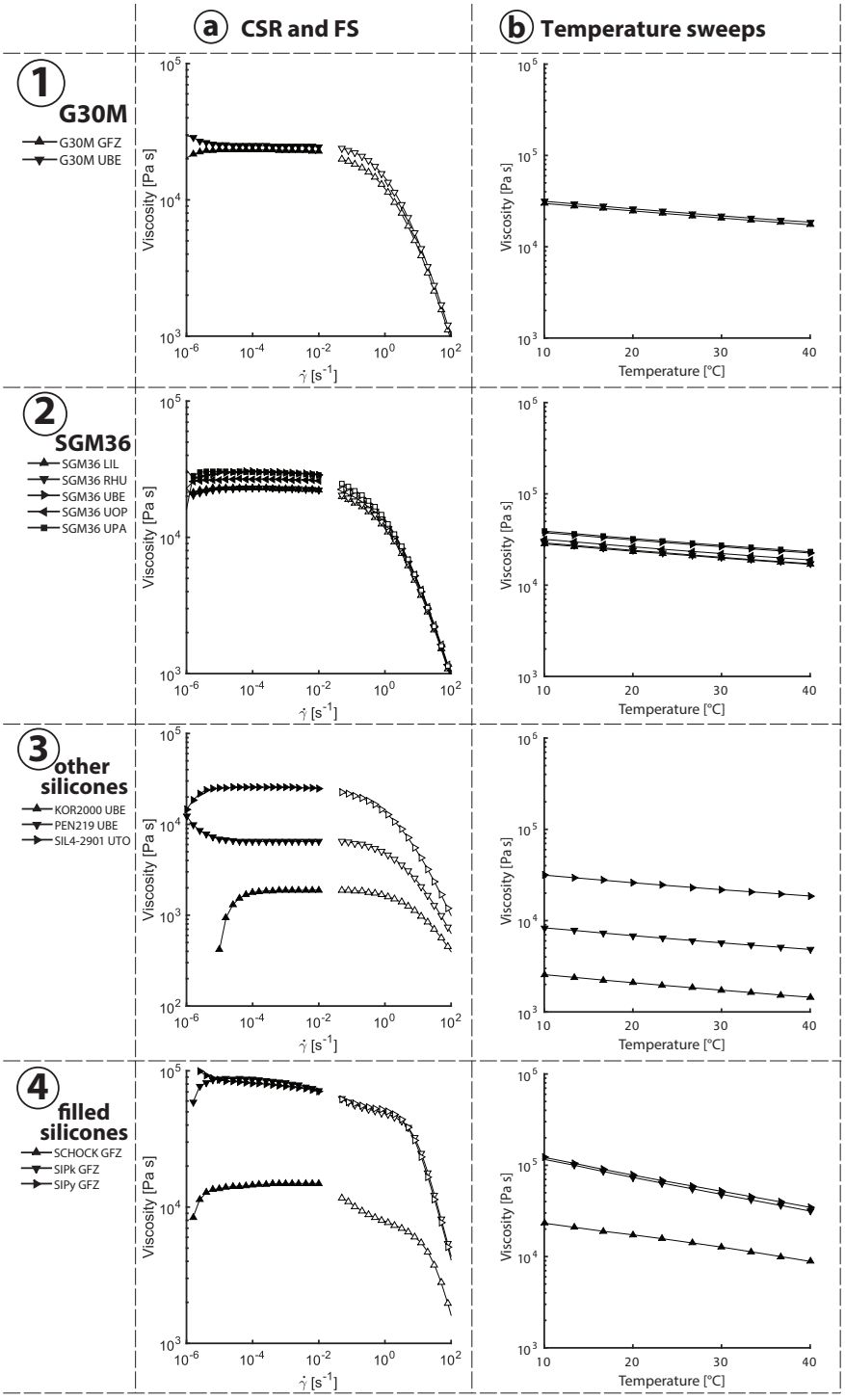

Figure 2.3: Column (a) shows the combined curves from CSR (filled symbols) and frequency sweep (hollow symbols) tests. All materials show a plateau value in the low shear rate regime. At very low shear rates the values presented are not significant due to the limitation of the rheometer but are included for completeness. Column (b) shows the effective viscosity depending on temperature. The pure silicones show a reduction of ≈1.5% per °C and the filled silicones of up to 4.5% per °C.

Table 2.3: Results of new and old controlled shear rate test (CSR) and temperature sweep data. All errors are given as 2σ derived from the 95% confidence bounds of the curve fits.

		CSR-Test		Data RC30 Rheometer	Temperature sweep	
Material	Institute	n	η_0 [Pa s]	η_0 [Pa s]	$\eta_{T\to\infty}$ [Pa s]	$E_A[kJ/mol]$
SGM36	UOP	0.997 ± 0.002	2.60 $\times 10^4$	(2.34 ± 0.11)$\times 10^4$	137.42 ± 6.58	12.81 ± 0.12
	LIL	0.995 ± 0.001	2.19 $\times 10^4$	(2.08 ± 0.09)$\times 10^4$	129.02 ± 4.25	12.69 ± 0.08
	UPA	0.992 ± 0.001	2.79 $\times 10^4$	(2.73 ± 0.19)$\times 10^4$	170.77 ± 6.73	12.79 ± 0.09
	RHU	0.997 ± 0.002	2.23 $\times 10^4$	(2.22 ± 0.13)$\times 10^4$	119.62 ± 4.95	12.93 ± 0.09
	UBE	0.994 ± 0.003	2.84 $\times 10^4$	(2.73 ± 0.23)$\times 10^4$	173.31 ± 7.54	12.67 ± 0.11
G30M	GFZ	0.996 ± 0.001	2.24 $\times 10^4$	-	109.80 ± 4.20	13.19 ± 0.09
	UBE	0.996 ± 0.001	2.42 $\times 10^4$	(2.49 ± 0.12)$\times 10^4$	122.30 ± 5.38	13.06 ± 0.11
PEN219	UBE	0.994 ± 0.003	6.20 $\times 10^3$	(6.13 ± 0.27)$\times 10^3$	27.75 ± 1.29	13.43 ± 0.11
SIL4-2901	UTO	0.999 ± 0.002	2.51 $\times 10^4$	(2.36 ± 0.12)$\times 10^4$	125.98 ± 6.13	12.99 ± 0.12
KOR2000	UBE	1.020 ± 0.076	2.10 $\times 10^3$	(1.76 ± 0.12)$\times 10^3$	6.66 ± 0.17	14.01 ± 0.06
SIPy	GFZ	0.975 ± 0.003	6.42 $\times 10^4$	-	0.26 ± 0.03	30.71 ± 0.26
SIPk	GFZ	0.973 ± 0.007	6.62 $\times 10^4$	-	0.17 ± 0.03	31.71 ± 0.39
SCHOCK	GFZ	1.010 ± 0.003	1.60 $\times 10^4$	-	1.64 ± 0.87	22.53 ± 1.29

At shear stresses below 0.1 Pa the accuracy of the measurement is low. This inaccuracy manifests itself with unrealistic changes in viscosity at very low shear rates $\dot{\gamma} < 10^{-5}$. Samples with a lower viscosity like KOR2000 suffer from this effect up to higher shear rates. As shear rates exceed $10^{-2}\, s^{-1}$ the effective viscosity of all samples decreases and shows a power-law behavior.

Zero shear viscosities obtained from the Cross equation are within the same range as the results from the CSR tests (Table 2.3). Only the filled silicones show larger differences. This is because the Cross equation does not fit well to the curves. The critical shear rate $\dot{\gamma}_c$ is similar for SGM36, G30M, SIL4-2901 and the filled silicones. It is higher for PEN219 and KOR2000. The power-law coefficients for high shear rates show that the pure silicones exhibit a slower decrease ($0.41 < p < 0.58$) in viscosity than the filled silicones ($0.29 < p < 0.34$). This is also reflected by the narrower viscous to elastic transition (Section 2.6.3). The power-law coefficient p from the Cross equation is the inverse of the power-law coefficient m in the flow law $\dot{\gamma} = const \cdot \tau^m$ commonly employed to describe the flow of rocks in rock deformation experiments [Bürgmann and Dresen, 2008]. As a result, m varies between 1.7 and 2.3 for the pure silicone oils, whereas m is 2.9 - 3.4 for the filled silicone oils.

2.6.2 Temperature dependency of viscosity

All samples show a temperature dependence which leads to a decrease in effective viscosity with increasing temperature (Figure 2.3 - column b). For the pure silicone oils the decrease in viscosity ranges between 1.4% and 1.9% per 1 °C (Figure 2.3 - 1b, 2b, 3b). The filled silicones are generally more sensitive to temperature with viscosity losses of 2.5% to 4.5% per 1 °C (Figure 2.3 - 4b).

The activation energies for the individual silicones are similar. Accordingly, they do not show a correlation with differences measured for other parameters. All pure silicones, except KOR2000, show an activation energy of around 13 $\frac{kJ}{mol}$. KOR2000 has a slightly increased activation energy of 14 $\frac{kJ}{mol}$. The filled silicones are between 23 and 32 $\frac{kJ}{mol}$.

2.6.3 Viscoelastic properties

The amplitude sweeps show that the pure silicone oils generally have a higher limit of linear viscoelasticity (LVE-limit) than the filled silicones (Figure 2.4 - column a). The limits for the pure silicone oils range from 0.60 for SGM36 UPA and G30M UBE, to 1 for KOR2000 UBE. The filled silicone oils show values of 0.1 and less (Table 2.4). Nearly all samples show steady values for G' and G" below the LVE limit. Only SHOCK GFZ shows an increase in both moduli with increasing strain (Figure 2.4 - 4a). The dynamic moduli are distinctly different below the LVE-limit but are similar at higher strains for the same material (Figure 2.4 - 1a, 2a).

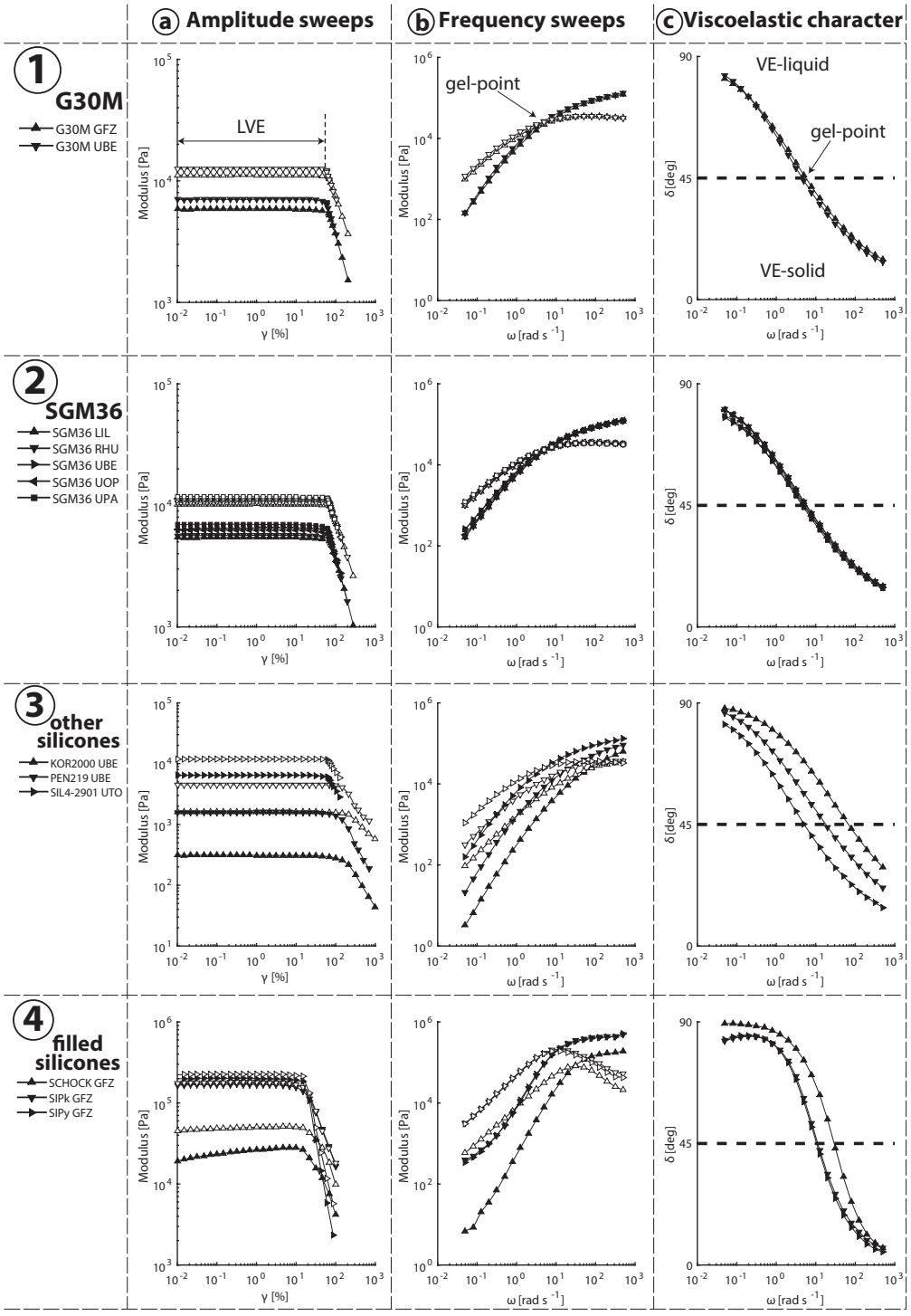

Figure 2.4: Results for the oscillatory tests where filled symbols represent the storage modulus G' and the hollow symbols represent the loss modulus G". The amplitude sweep curves display the linear viscoelasticity (plateau value) up to a certain yield stress which leads to non-linear deformation. The frequency sweeps show an intersection of G' with G" for each material representing the gel point. Viscoelastic character shows different slopes, onsets and transitional values for pure silicones and filled silicones. The dashed line represents $\delta = 45°$ which is true for G'=G".

Table 2.4: Results of the oscillatory tests. All errors are given as 2σ as in table 2.3.

		Oscillatory test			Cross fit			
Material	Institute	LVE	ω_{gel}[rad s^{-1}]	λ_M [s]	η_0 [Pa s]	λ_c [s]	$\dot{\gamma}_c$ [s^{-1}]	p
SGM36	UOP	0.65	5.3	0.189	(2.65 ± 0.03)×10^4	5.03 ± 1.26	2.0 ×10^{-1}	0.44 ± 0.04
	LIL	0.75	5.8	0.172	(2.28 ± 0.03)×10^4	4.28 ± 1.00	2.3 ×10^{-1}	0.44 ± 0.04
	UPA	0.6	4.6	0.217	(2.99 ± 0.03)×10^4	6.58 ± 1.59	1.5 ×10^{-1}	0.43 ± 0.04
	RHU	0.7	5.8	0.172	(2.27 ± 0.02)×10^4	3.13 ± 0.63	3.2 ×10^{-1}	0.47 ± 0.04
	UBE	0.65	5.0	0.200	(2.99 ± 0.04)×10^4	8.99 ± 2.30	1.1 ×10^{-1}	0.41 ± 0.04
G30M	GFZ	0.65	5.6	0.179	(2.31 ± 0.03)×10^4	3.87 ± 1.01	2.6 ×10^{-1}	0.45 ± 0.05
	UBE	0.6	4.6	0.217	(2.50 ± 0.01)×10^4	1.58 ± 0.19	6.3 ×10^{-1}	0.58 ± 0.03
PEN219	UBE	0.65	17.9	0.056	(6.52 ± 0.01)×10^3	0.69 ± 0.07	1.4 ×10^0	0.52 ± 0.03
SIL4-2901	UTO	0.6	5.1	0.196	(2.52 ± 0.03)×10^4	2.93 ± 0.64	3.4 ×10^{-1}	0.49 ± 0.05
KOR2000	UBE	1	67.1	0.015	(1.95 ± 0.01)×10^3	0.26 ± 0.04	3.8 ×10^0	0.47 ± 0.03
SIPy	GFZ	0.1	11.4	0.088	(7.98 ± 0.20)×10^4	6.89 ± 5.99	1.5 ×10^{-1}	0.34 ± 0.08
SIPk	GFZ	0.1	10.3	0.097	(8.34 ± 0.20)×10^4	7.91 ± 6.97	1.3 ×10^{-1}	0.34 ± 0.08
SCHOCK	GFZ	10^{-3}	25.1	0.040	(1.45 ± 0.03)×10^4	4.90 ± 2.89	2.0 ×10^{-1}	0.29 ± 0.05

The maximum strain amplitude during the test is dependent on the rheometer. Due to the maximum allowed shear force, a strain of $\gamma = 10^3 s^{-1}$ is not reached for all samples. Only materials with lower viscosities (KOR2000 and PEN219) reach the targeted maximum shear strain.

All materials show a change from VE-liquid to VE-solid (at the gel point) with increasing shear rate during the frequency tests (Figure 2.4 - column b). SGM36, G30M and SIL4-2901 exhibit a gel point of 4.6 to 5.8 rad s^{-1} (Table 2.4). SIPk and SIPy have higher gel points of 10 to 11 rad s^{-1}. PEN219 and SHOCK show gel points of 18 and 25 rad s^{-1} respectively. KOR2000 has the highest gel point with 67 rad s^{-1}. The resulting Maxwell relaxation times of SGM36, G30M, and SIL4-2901 range between 0.17 and 0.22 s (Table 2.4). The silicone oils with lower viscosity (PEN219 and KOR2000) have faster Maxwell relaxation times of 0.056 s and 0.015 s, as well as the SHOCK material with 0.040 s. The relaxation times of SIPk and SIPy are 0.088 s to 0.097 s.

The curves for viscoelastic character (Figure 2.4 - column c) have different shapes and slopes. Although the width of the transitional zone is similar for the pure silicone oils (Figure 2.4 - 1c, 2c, 3c), but with noticeable differences for the onsets of transitional behavior and peak slopes. The filled silicone oils show a very narrow transitional zone and generally higher peak slopes (Figure 2.4 - 4c). Additionally, SIPk and SIPy show a viscous peak between 10^0 and $10^{-1} s^{-1}$ indicating that they are more viscous in that regime than at lower shear rates.

2.6.4 Aging effect

The results obtained in 2015 for the effective viscosity are quantitatively close or quasi identical within error to results obtained in 2008 with the same samples (Table 2.3) but with a different rheometer (a stress controlled RC30 by RheoTec Meßtechnik GmbH (Germany)).

In addition, G30M GFZ is tested for differences in individual batches of material. Two batches from two different years (2009 and 2011) were measured multiple times with a time difference of 126 days ($\approx$ 4 months). The material was split and one fraction was stored in a closed barrel while the other fraction was stored in an open plastic cup under laboratory conditions. Frequency sweeps are used to determine the parameters that possibly change during storage. To illustrate differences the results are normalized to the youngest and freshest sample which is 2011a (Figure 2.5). Prior to sampling the 2011 barrel was still unopened and sealed in its original packaging.

Measurements on the 2011 batch material show a reduction in viscosity 126 days after opening (Figure 2.5). The sample that was left open in the lab shows a higher reduction of nearly 5 % over the complete shear rate range whereas the material in the barrel only lost around 2% of its viscosity. Compared to the 2011 batch the 2009 batch shows a strong decrease in viscosity especially for low shear rates. Separate samples of the 2009 batch exhibit only minor differences. The same changes apply to storage and loss moduli of the material. However the viscoelastic characteristics and the Maxwell relaxation times are not affected by these changes in viscosity. Each batch shows its own characteristic Maxwell relaxation time. The 2009 batch shows a λ_M of 0.18 s whereas for the 2011 batch it is 0.21 s.

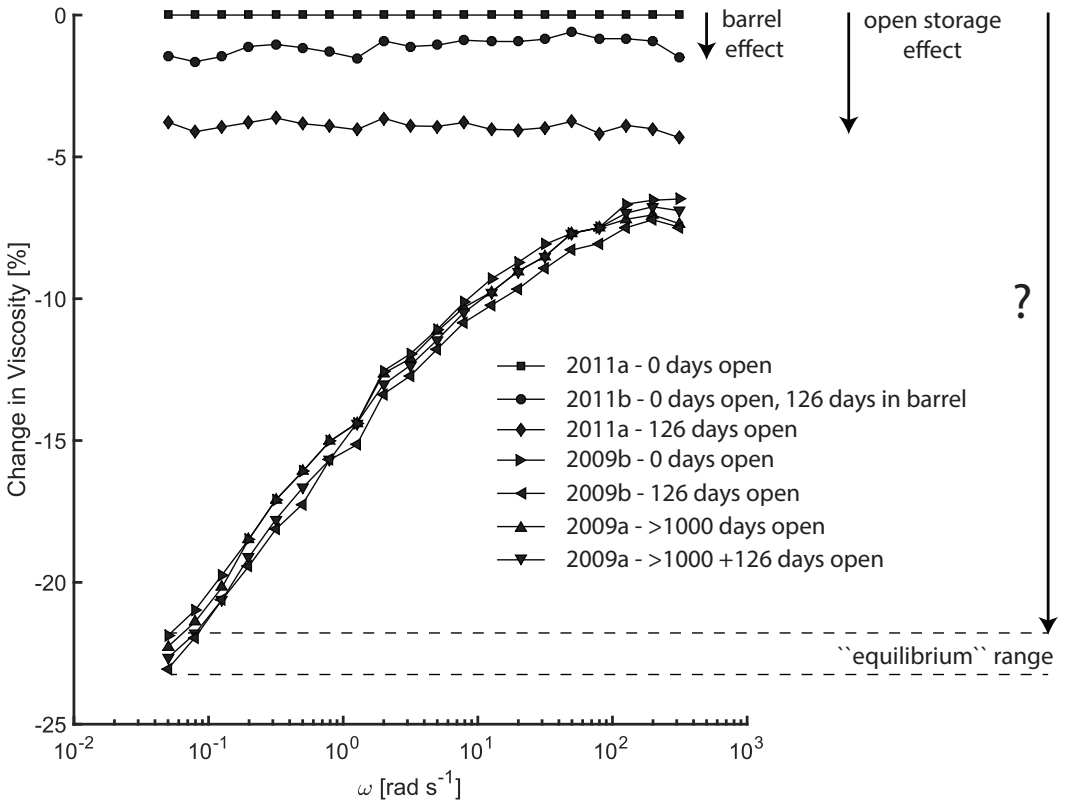

Figure 2.5: Comparison of different batches (2009 and 2011) of G30M. This plot shows the viscosity loss during a frequency sweep. The youngest and freshest sample (2011a, 0 days open) was used to normalize the plot. The samples were taken either from the barrel immediately before measuring and/or were left open for several months in the lab. The aging effect is strongest when the sample is exposed to fresh air. The silicones seem to equilibrate to a certain range after long exposure.

2.7 Discussion

2.7.1 Comparison of results with existing data

It has been repeatedly shown that SGM36 behaves as a linear viscous (Newtonian) fluid below strain rates of 10^{-2} to $10^{-1}s^{-1}$ and adheres to a power-law with an exponent of $m = 1-2$ above $10^{-1}s^{-1}$ [Weijermars, 1986a, Ten Grotenhuis et al., 2002]. This behavior has been re-confirmed by our analysis. The viscosities at 20°C for our SGM36 samples range between $2.4 - 3.2 \times 10^4$ Pa s and are therefore quasi identical to those obtained by Ten Grotenhuis et al. [2002] at the same temperature. At 23°C, our samples of SGM36 have a viscosity of $2.2-2.8\times10^4$ Pa s which is about half of what Weijermars [1986a] suggested at 24°C (5×10^4 Pa s). This difference could be either due to an aging effect in our samples, real changes in manufacturing or simply due to the very different measuring techniques.

In the viscoelastic regime, the gel point reported by Ten Grotenhuis et al. [2002] occurs at a frequency of 13 s^{-1} which is about twice of what we obtained (5 s^{-1}). In terms of the Maxwell relaxation time, which is the inverse of the gel point, the difference is 0.07 s vs. 0.18 s. The reason for this difference is unclear. It is unlikely that the cause is the 3°C difference in measurement temperatures because an increase in temperature causes a decrease in Maxwell relaxation time [Ten Grotenhuis et al., 2002, Mezger, 2006]. Weijermars [1986a] reported a Maxwell relaxation time of 1-10 s which is well beyond the more recent estimates and might again be related to real differences in the materials due to aging, manufacturing, or due to different measurement techniques.

The parameters obtained by our study for silly putty are similar to the results from Cross [2012] although he used a different technique for estimating the viscosity (dropping a load onto the sample). The silly putties measured by Weijermars [1986a] show a very different character but this might be due differences in the materials. In general, silly putties are difficult to compare because of lack of knowledge of the exact chemical composition of the samples used in previous studies.

2.7.2 Variability between samples and implications for scaling and model comparison

Variabilities in material properties are a primary control of differences in analog model results. Our evaluation of the differences between chemically similar PDMS samples (SGM36, G30M, SIL4-2901) shows that differences are small and range in terms of viscosity from $2.2-2.8\times10^4$ Pa s. Given the uncertainty in viscosity estimates in nature for the lower crust and mantle (which are of several order of magnitudes), we consider the variability found in our study negligible by comparison. However, for a correct scaling of analog model results as well as interpretation and cross-validation (i.e. comparison between analogue laboratories or between analogue and numerical simulations), a good control on the actual viscosities should be the ultimate goal. The Maxwell relaxation times for these materials range from 0.17 - 0.22 s. This variability is also considered a minor issue when comparing with a prototype, but may be problematic for cross-validation.

One major component in the system that is easily controlled is temperature. Some laboratories have the ability to run their experiments under constant temperature and humidity conditions. It is necessary to know the temperature of the silicone oil during the experiment as

temperature can alter the viscosity by several percent.

2.7.3 Implications of aging effects for proper storage

The comparison of two batches of G30M shows that there is a gradual decrease in viscosity and dynamic moduli with time. This strongly depends on the storage conditions, which determine to what extent typical reactions such as exchange of volatile substances or oxidation can occur. The loss of viscosity suggests that a weakening mechanism is acting during aging. We suspect that two mechanisms are active simultaneously. The dominant mechanism is the incorporation of water from ambient humidity into the polymer structure [Maxwell et al., 2003]. Water molecules weaken the intermolecular bonds and allow easier movement. Secondly, a temperature dependent depolymerization is weakening the material [Eddington et al., 2006, Xiang et al., 2012]. This leads to a shortening of the polymer chains resulting in lower viscosity. This effect will also take place in a closed system.

The combined influence of humidity and temperature is larger than the effect of depolymerization, assuming average temperatures of 23°C. Very high temperatures beyond the usual experimental range (>85°C) accelerate the depolymerization [Maxwell et al., 2003, Xiang et al., 2012]. In this case we can only infer the effect of equilibration with the ambient laboratory humidity. The change of the material in the barrel over the testing period is probably partially attributable to the "contamination" with humidity after the opening. Our observations suggest that PDMS equilibrates with laboratory conditions within months and stays rather constant for periods well beyond the official shelf life time. Storing PDMS for several years in closed containers under laboratory conditions, therefore, seems feasible.

2.7.4 Perspective for analog models using viscoelasticity

All tested materials show a change in their deformation behavior from Newtonian to power-law. This is similar to the behavior of rocks below the brittle-viscous transition. This is in accordance with the conclusions of Weijermars and Schmeling [1986]. The power-law coefficients m for the studied silicone oils are in the same range as experimentally derived values for natural rocks. Therefore, the tested silicone oils are dynamically similar at typical experimental shear rates not only in the Newtonian regime, but also in the viscoelastic regime. In contrast to Weijermars [1986b] conclusion that his filled silicone oil is not suitable for analog modeling, we found significantly lower power-law coefficients and a completely different behavior in the low-shear rate regime for the filled silicone, meaning that this material is indeed a suitable analog.

To scale viscoelasticity, the Maxwell relaxation times of the prototype and analog material can be linked using the Deborah number. Assuming that relaxation times of the lower crust and mantle are in the order of tens to hundreds of years [e.g. Bürgmann and Dresen, 2008] and an observational timescale, e.g. for geodesy, is in the order of one to ten years, the resulting Deborah number of the system is 1 - 100. This means that the observational timescale in experiments using silicone oils with relaxation times of 0.1 - 0.2 s, needs to be shorter than 1 - 200 ms in order to be correctly scaled and at the same time provide observations comparable to nature.

2.8 Conclusion

We performed rotational and oscillatory tests on a set of silicone oils commonly used in the analog tectonic modeling community. Our results confirm the viscoelastic behavior of silicones shown by previous studies and their suitability to model a variety of short- to longterm tectonic processes under laboratory conditions. The transition from Newtonian behavior at low strain rates ($< 10^{-2}s^{-1}$) to power-law behavior and a pronounced viscoelasticity at higher strain rates opens the perspective to use silicone oils not only for modelling longterm processes like ductile flow of the lower crust or mantle but also for short-term processes like seismic cycles [e.g. Caniven et al., 2015]. A Maxwell relaxation time in the order of 0.1 s for silicones should dictate the temporal scaling of such models which requires a high rate of monitoring.

We could verify aging effects of the silicones at different time scales (months to years) and interpreted these effects as being due to storage conditions (sealed, closed, open storage). We conclude that storage beyond the shelf life time of the materials is feasible, since the properties of the material change in the order of just a few percent provided they are stored in closed or sealed containers under laboratory conditions.

The variability between the chemically similar materials used by different laboratories as well as the aging and temperature effect on viscosity are small compared to uncertainties in natural properties. However, for the comparison of analog models and especially for cross-validation, the differences obtained might be critical. Therefore, we suggest reporting age, storage, and lab conditions (temperature and humidity) during the experiment, and if possible measuring the actual properties of the materials used.

Acknowledgments

M. Ritter is greatly appreciated for his help with the rheometer. Y. van Dinther, Y. Caniven and an anonymous reviewer are acknowledged for their helpful remarks and suggestions for revision. We thank K. Leever and J. Bedford for their corrections and help with the manuscript. The editor K. Wang is thanked for handling the editorial process of this manuscript. Funding was provided by the Deutsche Forschungsgemeinschaft (DFG) through CRC-1114-'Scaling Cascades in Complex Systems'.

List of Variables

δ	=	phase shift angle
$\dot{\epsilon}$	=	strain rate
$\dot{\gamma}$	=	shear strain rate
$\dot{\gamma}_c$	=	transitional shear rate from Newtonian to power-law behavior
ϵ	=	strain
η	=	viscosity
$\eta_{T\to\infty}$	=	viscosity at infinitely high temperatures
η_0	=	viscosity at zero shear
γ	=	shear strain
γ_A	=	shear strain amplitude during oscillation
γ_{LVE}	=	shear strain limit for linear viscoelasticity
λ_M	=	Maxwell relaxation time
ω	=	angular frequency
ω_{gel}	=	angular frequency at the gel point
σ	=	stress
τ	=	shear stress
De	=	Deborah number
E_A	=	activation energy
G'	=	storage modulus
G''	=	loss modulus
G^*	=	complex shear modulus
n	=	power-law exponent for flow laws
m	=	power-law exponent for rock flow laws
p	=	power-law exponent for Cross equation
R	=	universal gas constant
T	=	temperature
t	=	time
t_p	=	observation time

Chapter 3

Interseismic deformation transients and precursory phenomena: Insights from stick-slip experiments with a granular fault zone

M. Rudolf[1], M. Rosenau[1], O. Oncken[1]

[1] *Lithosphere Dynamics, Helmholtz Centre Potsdam, German Research Centre for Geosciences (GFZ), Telegraphenberg, D-14473 Potsdam, Germany*

This chapter has been submitted for publication to ***AGU Journal of Geophysical Research - Solid Earth*** as:

Rudolf, M.; Rosenau, M.; Oncken, O. (submitted): Interseismic deformation transients and precursory phenomena: Insights from stick-slip experiments with a granular fault zone.

An undedited preprint is available in the EarthArXiv at `https://dx.doi.org/10.17605/OSF.IO/6MWRX`.

Individual Contributions:

M. Rudolf planned and performed the research, measured and analysed the data, and wrote the research paper. M. Rosenau was involved in planning the research, analysing the results and writing. O. Oncken was involved in supervising the research and writing.

Keypoints

- External and internal forcing alter the characteristics of slip events in granular fault analogs
- Precursory slip and transient creep influence predictability of slip events
- A characteristic scale gap between fast and slow slip events is observed

3.1 Abstract

The release of stress in the lithosphere along active faults shows a wide range of behaviors spanning several spatial and temporal scales. It ranges from short-term localized slip via aseismic slip transients to long-term distributed slip along large fault zones. A single fault can show several of these behaviors in a complementary manner often synchronized in time or space. To study the multiscale fault slip behavior with a focus on interseismic deformation transients we apply a simplified analog model experiment using a rate-and-state-dependent frictional granular material (glass beads) deformed in a ring shear tester. The analog model is able to show, in a reproducible manner, the full spectrum of natural fault slip behavior including transient creep and slow slip events superimposed on regular stick-slip cycles (analog seismic cycles). Analog fault slip behavior is systematically controlled by extrinsic parameters such as the system stiffness, normal load on the fault, and loading rate. Accordingly, interseismic creep and slow slip events increase quantitatively with decreasing normal load, increasing stiffness and loading rate. We observe two peculiar features in our analog fault model: (1) Absence of transients in the final stage of the stick-slip cycle ("preseismic gap") and (2) "scale gaps" separating small interseismic slow (aseismic) events from large (seismic) fast events. Concurrent micromechanical processes, such as dilation, breakdown of force chains and granular packaging affect the frictional properties of the experimental fault zone and control interseismic strengthening and coseismic weakening. Additionally, interseismic creep and slip transients have a strong effect on the predictability of stress drops and recurrence times. Based on the strong kinematic similiarity between our fault analog and natural faults, our observations may set important constraints for time-dependent seismic hazard models along single faults.

3.2 Introduction

Active faults are characterized by a wide range of slip behaviors ranging from aseismic creep to seismic stick-slip that may change spatially along the fault and temporally over the seismic cycle [e.g. Harris, 2017, Ide et al., 2007]. The types of slip are defined by their characteristic timescale which ranges from milliseconds to a few years [Obara and Kato, 2016]. Depending on their characteristics in time and seismic wave forms, the slip events are characterized as seismic (very low frequency earthquakes, tremors, normal earthquake) or geodetic (short-term and long-term slow slip events) events. They can occur simultaneously, i.e. within one seismic cycle, at the same locality or in different depth ranges of the same main fault. The physical origin of this range of slip modes is still not entirely clear, although several valid explanations for certain phenomena have been found. In this study we purely focus on the frictional characteristics of a fault zone which is described within the rate-and-state framework [Dieterich, 1979a, 2007]. Other processes that influence the slip modes along a fault zone are variations in pore-fluid pressure, changes in material because of comminution, or mineral reactions. Not all slip modes are observed for all

active zones which strongly suggests that there is a complex interaction between the processes acting on different scales in space and time. Knowledge of the complex interactions between the different slip modes is relevant for estimating the seismicity rates along plate boundaries and therefore for seismic hazard assessment.

The rate-and-state framework describes the evolution of sliding resistance, that is friction μ, along an interface between two bodies [Dieterich, 1979a]. Although the friction within geological materials roughly corresponds to the Coulomb friction ($\tau = \mu \cdot \sigma + C$), experiments have shown that friction is not constant and shows a non-linear evolution with sliding velocity, stress evolution and slip history [see Dieterich, 2007, and references therein]. This complex evolution of friction generates episodic slip behavior because sliding resistance can decrease once a certain criteria, e.g. sliding velocity, is reached. In very general terms, this can be described by two different friction coefficients. Static friction μ_s that describes the strength of the material at rest and dynamic friction μ_d that describes the sliding resistance in motion. Both terms are used to describe the phenomenological behavior of the system, but both originate from the same heuristic description and continuously evolve during sticking and sliding [Dieterich, 1979a, Ruina, 1983, Rice, 1983].

The seismic behavior of faults is primarily dependent on its frictional stability which is influenced by several parameters of the fault system [Scholz, 1998]. The term stability refers to whether slip can nucleate spontaneously (unstable), only propagate along the interface (conditionally stable), or can not nucleate at all (stable). Stick-slip experiments using rock and rock analogs suggest that besides intrinsic material properties (e.g. friction coefficient, slip/velocity weakening), extrinsic parameters like stiffness, normalized loading rate and effective normal stress are key controls of frictional (in)stability [e.g. Leeman et al., 2016, Heslot et al., 1994, Marone, 1998, Mair et al., 2002]. Two types of interfaces are controlling the frictional slip along two crustal blocks. Bare rock surfaces control the slip behavior of young faults, whereas in mature fault zones, the frictional component is mainly defined by fault gouge that forms because of abrasive processes. Both frictional interfaces can exhibit stick-slip type behavior and may evolve over the duration of multiple seismic cycles.

In this study we focus on the effect of a granular material on seismogenesis. We here report characteristics of slip events in an analog fault gouge consisting of spherical glass beads. In contrast, to similar experiments [Marone et al., 2002, Anthony and Marone, 2005, Ferdowsi et al., 2013, Jiang et al., 2016, Cui et al., 2017] we explore the low pressure (kPa instead of MPa) and low stiffness regime which is rich in slip behaviors and generates regular stick-slip with more complete stress drops similar to seismic cycles along major faults in a highly reproducible way. Assuming that rate-and-state dependent friction is a scale independent process, we use lower pressures and lower stiffnesses which has several technical advantages over high-pressure testing procedures. Moreover, the use of a ring-shear tester instead of commonly used direct shear apparatuses allows us to apply an in principle infinite amount of displacement and therefore a large number of events, which is a solid database for statistical analysis.

For the same material we vary the extrinsic parameters normal stress σ_N, loading velocity v_L, and stiffness k_L. In this parameter space, we monitor the occurrence of slip events and creep, as well as the transitions from one slip mode to another. The main purpose of this study is to demonstrate the influence of interseismic transient slip phenomena on the overall seismic cycle behavior. We compare the findings to first order observations from earthquake catalogs and to rock friction experiments.

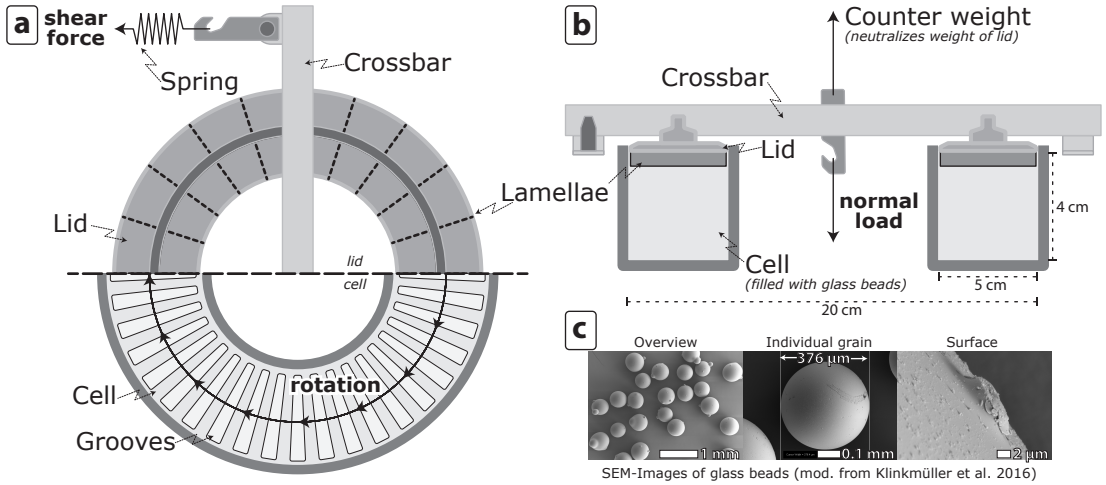

Figure 3.1: Schematic drawing of the modified ring shear tester. The system is loaded at loading velocities of $5{\cdot}10^{-2}$ to $8{\cdot}10^{-4}$ $\frac{mm}{s}$ by rotating the cell. The cell has grooves for a high friction interface which is mirrored by lamellae attached to the lid. A moveable weight pulls the lid from below by a motor driven lever for applying normal load. Force transducers behind the springs measure shear force. a) Top view the above part showing the lid and the bottom part showing the cell and its internal structure. b) Crosssection through the whole setup. c) Scanning electron microscopy images of the glassbeads showing the average particle size and the surface structures [modified from Klinkmüller et al., 2016].

3.3 Methods

3.3.1 Setup

For the experiments we use the ring shear tester of type 'RST-01.pc' [Schulze, 1994] with slight modifications (additional spring to reduce the stiffness). As a fault gouge analog material we use 300-400 μm sized fused quartz microbeads (Figure 3.1c). They are characterized by a relatively low friction coefficient (ca. 0.5) and cohesion (10-40 Pa) as well as a strain hardening-weakening behavior associated with dilation-compaction [Lohrmann et al., 2003, Klinkmüller et al., 2016, Ritter et al., 2016a]. They are frequently used as a rock and gouge analogue material and generate stick-slip under laboratory conditions [e.g. Mair et al., 2002]. In our setup, the glass beads are confined in a ring shaped shear cell and sheared against a lamellae-casted lid which also imposes the normal load (Figure 3.1a+b). Two bars attached to force transducers hold the lid in place. A granular shear zone of a few millimeters thickness localizes at the base of the lamellae. The applied and resulting forces (normal and shear), driving velocity (v_L, measured along a diameter dividing the cell area into two equally sized compartments) and vertical lid displacement (dilation d) are measured at a frequency of 12.5 kHz each.

All measured values are averaged over 20 samples for noise reduction resulting in a final output frequency of 625 Hz, high enough to study the stick-slip events at high resolution. Based on the setup geometry, we convert shear and normal forces into shear and normal stresses and lid displacement into volumetric change (dilation/compaction). Instead of displaying shear stress, we use the dimensionless actual friction (coefficient) μ which is defined as the shear force divided by the normal force throughout the manuscript.

Before an experiment is started, the sieved samples are presheared by 10 mm which ensures a fully developed shear zone without major post failure weakening [derived from Ritter

et al., 2016a,b]. The experiments are conducted as velocity stepping tests with logarithmically decreasing loading velocity V_L from $5{\cdot}10^{-2}$ $\frac{mm}{s}$ to $8{\cdot}10^{-4}$ $\frac{mm}{s}$. Normal stress σ_N is fixed for each individual time series. We use 4 different normal stresses of 5, 10, 15, and 20 kPa. For each velocity step the amount of displacement is constant, which leads to an approximately equal number of events per velocity step.

Previous studies examined granular media under natural pressure conditions, whereas we are using conditions realized by analog models, being 3 - 4 orders of magnitude lower [Rosenau et al., 2017]. This prevents comminution of the glass beads and ensures constant frictional properties over the experimental duration, which gives well reproducible results. Furthermore, the rate-and-state framework as a heuristic concept, reproduces the measured frictional properties of natural rock materials. If the whole stick-slip system acts as a self-organizing critical system (SOC) [Sornette and Sornette, 1989], a statistically similar system can be used as an analogue for it [Marković and Gros, 2014]. It is still under debate whether the earthquake system obeys such a scaling relationship, but it has been shown that it has major similarities with slip avalanches in granular piles, e.g. with the Olami-Feder-Christensen model [Caruso et al., 2007, Rundle et al., 2003].

3.3.2 Stiffness of the system

Three different types of stiffness are relevant for our setup. The loading stiffness k_L that is defined by the combined stiffness of the testing apparatus, force transducers, and attached spring without sample material. Loading stiffness changes from 1335 $\frac{N}{mm}$ (without spring) to 20 $\frac{N}{mm}$ (with spring). The unloading stiffness k_u which relates the stress drop to lid displacement during an event. It is measured for both setups (with and without spring) at all experimental normal stresses. Without spring the unloading stiffness is 624 $\frac{N}{mm}$, whereas with the spring it is 18 $\frac{N}{mm}$. The third stiffness acting in the system is the effective cyclic reloading stiffness k_c which includes the machine, spring and the material. It is derived from the linear fit of stress increase during the first 40% of the interseismic phase. This reloading stiffness is also used to calculate creep during the interseismic phase. For creep estimation, the linear trend is extrapolated to the point of failure and related to the measured stress at failure. For experiments without a spring k_c is 503 to 578 $\frac{N}{mm}$ and increases with normal stress. In contrast, k_c with a spring is very similar for normal stresses of 10 kPa and above, namely 33 to 34 $\frac{N}{mm}$, whereas for 5 kPa the stiffness doubles and is 67 $\frac{N}{mm}$.

3.3.3 Loading velocities

For a better comparison with other studies we normalize the loading velocity by cyclic reloading stiffness k_c and by normal stress σ_N to obtain a normalized loading rate $\dot{\mu}$. It describes the increase in non-dimensional frictional stress in the glass beads per second:

$$\dot{\mu} = \frac{V_L k_c}{\sigma_N} \tag{3.1}$$

In the presented experiments, normalized loading rates cover five orders of magnitude, with some overlap between experiments with and without spring. They range from 10^{-5} to 10^{0} s^{-1} which is comparable to experiments that have been conducted with rock samples in a geometrically similar apparatus at Brown University but with stress levels in the MPa-range [Tullis and Weeks, 1986, Beeler et al., 2014]. Other experiments at very low normal stresses of

less than 100 Pa that have been performed by Nasuno et al. [1997, 1998] and are in the range of 10^{-3} to 1 s^{-1} but with a geometrically different setup (pure spring-slider).

3.3.4 Data Analysis and Processing

The acquired measurements are analyzed with a suite of MATLAB scripts. Each slip event is automatically picked using two methods. The first method picks each event with a very simple peak-detection algorithm that compares each point with its neighbours. If a critical height or low is reached, the point is detected as either start or end of a slip event. For each experiment this threshold is adjusted to minimize the amount of wrong detections and varies between 10 and 45 Pa. Some experiments show slip events which have a strongly differing stress drop rate $\dot{\tau}$. A fast slip event is detected when a critical stress drop rate, a proxy for slip velocity, is reached. This may differ from experiment to experiment, and also depends on loading velocity, and is therefore manually picked for each time series. It varies between -620 $\frac{Pa}{s}$ and -7273 $\frac{Pa}{s}$. The experimental data, parameters, and scripts for reproducing the figures in this study can be found in Rudolf et al. [unpublished].

3.3.5 Assessing Predictability

As the regular stick-slip serves as an analogue for seismic cycles along major faults in nature we test for time and slip predictability and assess how interseismic transients affect the predictions. Time predictability is assessed after Bufe et al. [1977] which relates previous stress drop with stressing rate to predict the time until the next event:

$$t_r = \frac{\Delta\tau_{t-1}}{V_L k_c} \tag{3.2}$$

Slip predictability is assessed following Shimazaki and Nakata [1980] which calculates the expected stress drop $\Delta\tau_{t+1}$ by relating time passed since the previous event t_r and stressing rate:

$$\Delta\tau_{t+1} = t_r V_L k_c \tag{3.3}$$

To quantify the accuracy of both predictions the mean forecast error e_n is calculated and normalized by the measured mean $\bar{x}$. It is defined as the average difference of the predictions to the observations, divided by the mean of the measurements:

$$e_n = \frac{\frac{1}{n}\sum_{i=1}^{n}(x_{measured} - x_{predicted})}{\bar{x}} \tag{3.4}$$

The resulting values for e_n indicate how predictions differ from the measured values. If $e_n < 0$ the model tends to over forecast the observations and if $e_n > 0$ the model under forecasts the observations. For $e_n = 0$ model and observation are equal. The absolute value shows by how much the model is inaccurate normalized to the observation mean.

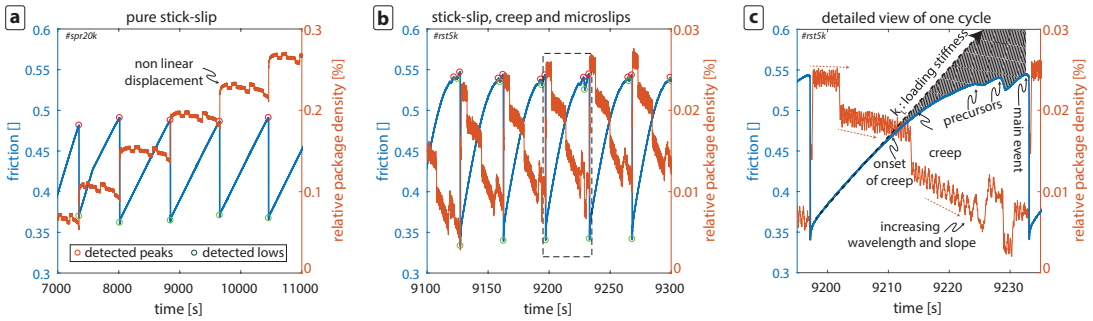

Figure 3.2: Typical stick-slip curves generated by the setup. Shear stress is normalized by normal load and shown in blue. Lid displacement (15 Hz low pass filtered), here relative to the lowest y-axis point for comparison, is shown in orange. Results of the peak detection is shown as red and green colored circles. (a) Experiment with low stiffness (spring) with few but relatively large events in a sawtooth shape. (b) High stiffness test (no spring) at the same velocity as in Figure 3.2a. The event rate is higher, with precursors and creep. (c) Detailed view of one cycle from Figure 3.2. After the previous slip event (t_{i-1}) with a slight overshoot, the system is reloaded linearly. In the second half of the cycle the fault zone starts to creep and finally shows several slow precursory events. Finally a new main event (t_i) occurs and stress drops to a similar level as for t_{-1}.

3.4 Observations

3.4.1 Stick-slip cycles

The glass beads show cyclic increases in shear stress followed by sudden stress drops characteristic for stick-slip. Because stick-slip is an analogue for seismic cycles we here use co- and interseismic as synonyms for the slip and stick (or locking) phase. For experiments with low loading stiffness (with spring, #spr..k) the stress-time evolution closely follows a sawtooth shaped curve with linear increases indicative of full sticking during the loading phase (Figure 3.2a). For higher loading stiffness (without spring, #rst..k) and at low normal stress, the loading curves become increasingly non-linear at higher stresses indicating accelerating interseismic creep (Figure 3.2b). In addition, smaller and slower slip events emerge close to failure stress and in the last third of a cycle of stiff systems.

Stick-slip cycles are associated with systematic volume changes: Interseismic dilation and coseismic compaction in the order of of 0.025 to 0.050 %. Interseismic dilation is non-linear and accelerates towards failure, in particular for the stiff system. Additionally, the lid displacement shows several distinct upward and downward steps of 1-2 μm which are not necessarily mirrored in the stress curve but very repetitive and similar for each interseismic phase. Another, second order, observation is that the low amplitude oscillations in the low pass filtered signal show an increase in their wavelength towards the end of the interseismic phase (Figure 3.2c). A secular trend over the experiment run indicates progressive material loss through the small gap between lid and shear cell.

The slip events show a characteristic size distribution which is unimodal for low stiffness and bimodal for high stiffness (Figure 3.3a+b). At low stiffness the distributions show a log-normal character with a positive skew. A comparison using Q-Q plots shows that all distributions are similar, except the distribution for the experiment at low normal stress of 5 kPa which has a slightly different shape and is shifted towards smaller sizes. The median is ≈0.036, while all other distributions show a significantly higher median of ≈0.066.

For a high stiffness the distributions are bimodal with one mode at very low stress drops <0.05 and one mode at higher stress drops. All events that belong to the lower mode are considered as precursors because of their lower stress drop rate compared to the catastrophic failures defining the higher stick-slip cycles (shaded area in Figure 3.3b). When the events are separated into precursors and main events each of the respective populations are similarly normal distributed. The median size of the precursors is ≈0.005 and ≈0.169 for the main events. Likewise, the experiment at a normal stress of 5 kPa is somewhat different from the other experiments. Although the median value does not show a significant difference, the distribution of the main events is broader and does in itself show a weak bimodal characteristic.

3.4.2 Precursory slip events

For the high stiffness setup small scale interseismic (precursory) small slip events can be detected. They are characterized by low stress drop and low stress drop rate. The relative amount of precursors decreases with increasing normal stress. For low normal stress more than 40% of the detected events are found to be precursors, whereas for higher normal stresses it is 5 - 10%. Additionally, there is a variation in occurrence with loading velocity. At high loading velocity only very few precursors are detected, while at low loading velocity multiple precursors of increasing size can occur before one main event.

In terms of frictional stress drop, most precursory slip events are at least one order of magnitude smaller than the main events. The average stress drop of a precursor is only 2.6% of the corresponding main event.

The occurrence of precursors shows a specific temporal pattern. They do not occur in the first half of the interseismic cycle. The probability of occurrence increases between 0.7 and $0.9t_r$ and peaks at $\approx 0.85t_r$ (Figure 3.3c). Then the probability drops abruptly to zero and for all experiments almost no precursor has been detected in the last 10% of the interseismic cycle. The stress level at which the precursors occur is generally very close to the stress level of the main event (Figure 3.3d). For higher normal stresses the precursors occur around $0.95\tau_f$, and for σ_N =5 kPa at higher stresses of $0.97\tau_f$. Few events happen at stresses equal to the stress level of the main events.

3.4.3 Event scaling

In the parameters space tested, we observe distinct systematics and gaps in the spectrum of observed slip rates. All events show an increase in stress drop rate with increasing loading rate (Figure 3.4a+b). This increase is independent of the amount of total stress drop, although a high stress drop coincides with a higher stress drop rate. For low stiffness experiments the events for 10 kPa and above fall into one category that show an increase in stress drop rate with loading rate of $\frac{\Delta\mu}{\Delta t} \propto \dot{\mu}^{0.36}$. For the low normal stress experiment the scaling is similar, but the whole cluster is shifted to higher normalized loading rates.

At high stiffness three clusters are observed that show different characteristics (Figure 3.4b). One cluster contains all precursor events that show low stress drop and low stress drop rates (shaded area in Figure 3.4b). They scale much stronger with loading rate and show an increase in stress drop rate by $\frac{\Delta\mu}{\Delta t} \propto \dot{\mu}^{0.87}$. A second cluster shows a scaling similar to the events at low stiffness with $\frac{\Delta\mu}{\Delta t} \propto \dot{\mu}^{0.46}$. But here the stress drop increases more strongly with decreasing loading rate than for low stiffness. A small cluster of very fast ($>2\mathrm{s}^{-1}$) and large ($\Delta\mu$ >0.2)

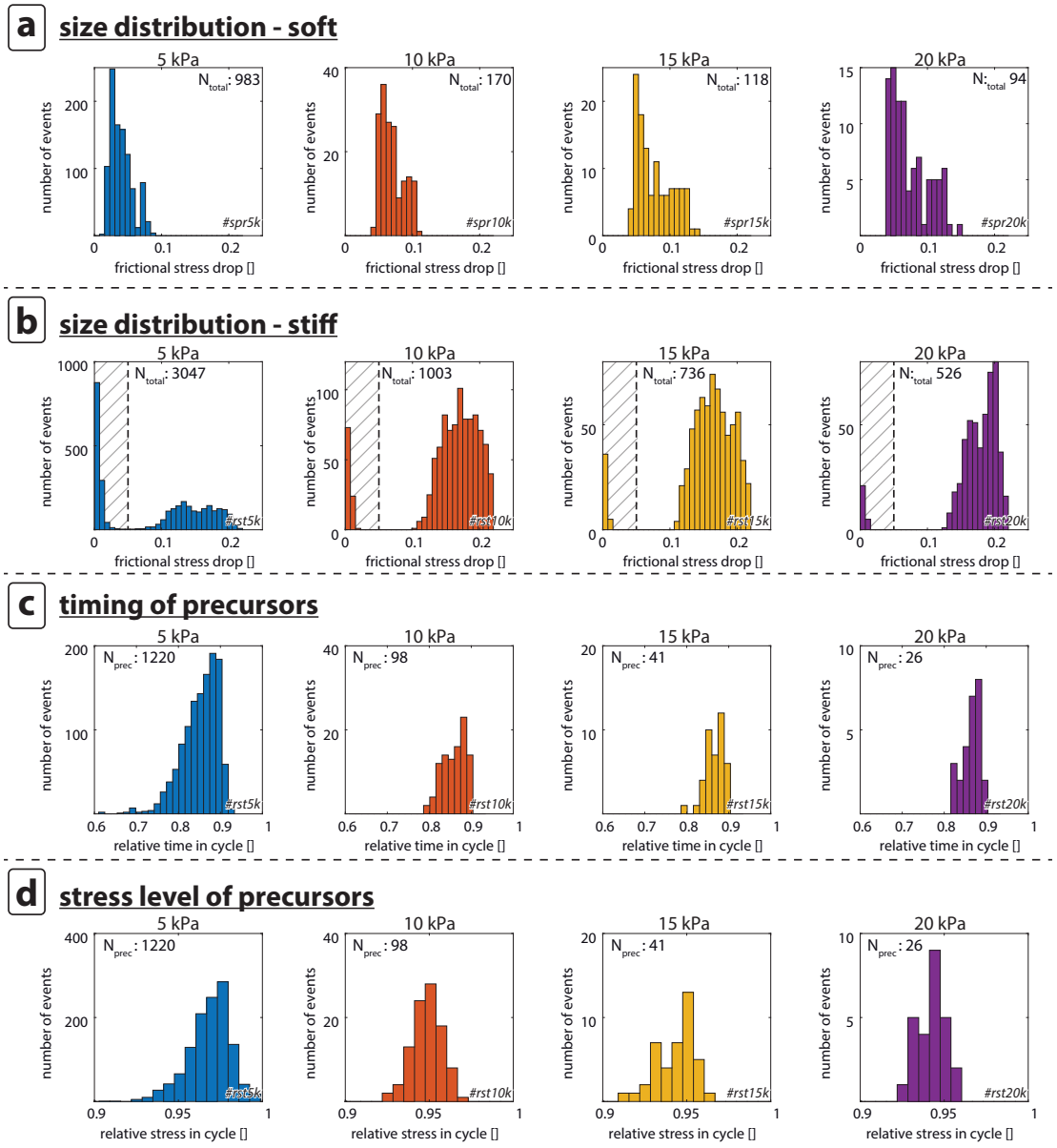

Figure 3.3: Distributions of event size and precusor occurrence. (a) Size distributions of slip events with spring (low stiffness). All distributions show a slight log-normal trend. (b) Size distribution for experiments without spring (high stiffness). The shaded area shows the location of the precursory events. (c) Timing of the precursor events within an event cycle. All precursors occur in the second half of the cycle and show an increased occurrence towards the end. (d) Stress level at which the precursors occur in the event cyle. They mainly happen at stresses close to failure ($>0.9\tau_f$) with a slightly decreasing median with increasing normal stress.

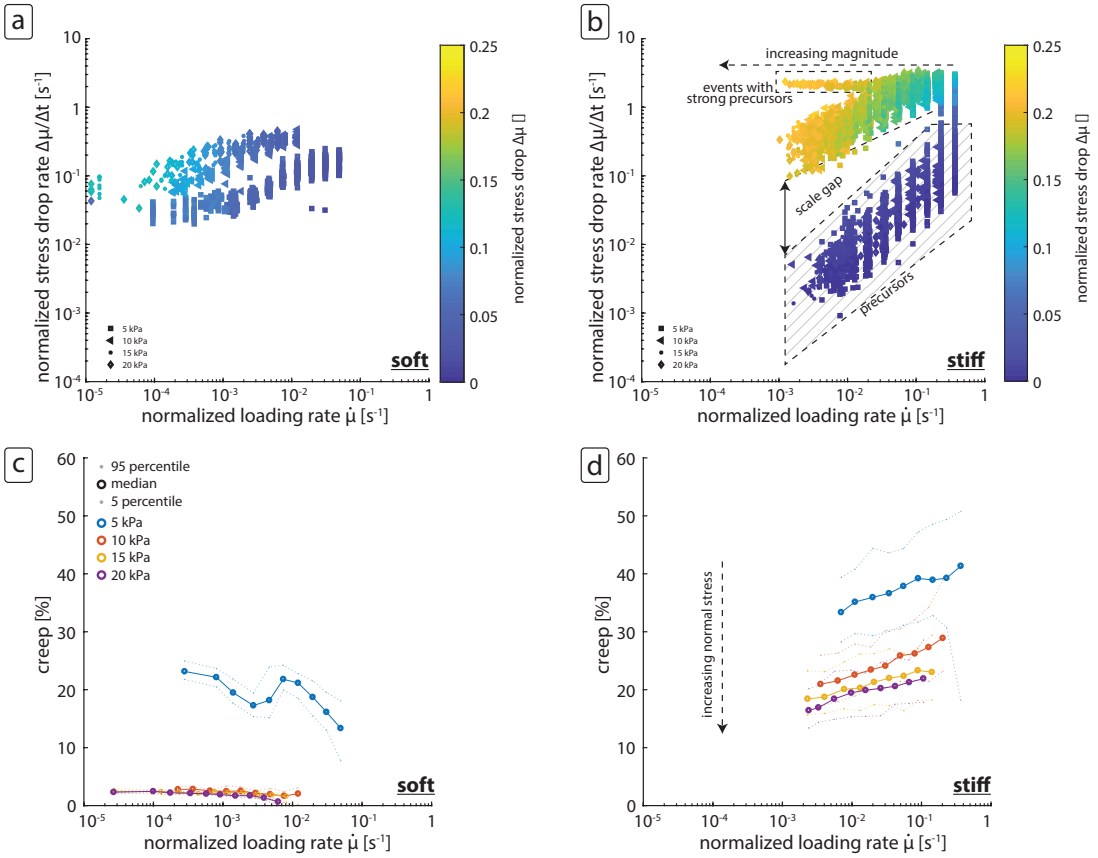

Figure 3.4: Scaling behavior and creep during the experiments. (a) Comparison of normalized stress drop rate and loading velocity for low stiffness. All detected events fall into a cluster of similar stress drop rate at each loading velocity. (b) Experiment with high stiffness where the precursors form a separate cluster (shaded area). They show significantly reduced stress drop rates and are much smaller. (c) Amount of creep as a function of normalized loading rate and normal stress for low experimental stiffness. Significant creep is only occurring at very low normal stress. (d) At high stiffness all experiments show creep, which decreases with increasing normal stress and decreasing normalized loading rate.

events is also observed (upper rectangle in Figure 3.4b). At the highest loading rates main events and precursors form a more continous distribution and are only separated by the difference in stress drop.

3.4.4 Creep

Each main slip event is followed by an initial phase of linear elastic loading indicating full postseismic locking. For experiments with high stiffness (#rst..k) and low load (#spr5k) this linear loading transitions into a non-linear loading phase. The amount of creep is derived by calculating the theoretical failure stress at the observed time of failure by linear extrapolation of the cyclic reloading stiffness, and estimating the stress deficit at the point of failure. This stress deficit is balanced by the total amount of interseismic deformation, including precursors, that has been released during each cycle. Accordingly, some precursory slip events can account for more than 30% of creep deformation but on average they only account for 10% of total interseismic creep.

The amount of creep is depending on the loading rate and on normal stress (Figure 3.4c+d).

An increase in normal stress leads to a strong reduction of creep and high stiffness experiments indicate that creep slowly approaches a non-zero limit (Figure 3.4d), rather than dropping to values near zero as is observed for the low stiffness experiments (Figure 3.4c). Furthermore, for high stiffness the total amount of creep increases with increasing loading rate but also the variability of creep per event increases.

3.5 Discussion and Interpretation

3.5.1 Micromechanical processes

Granular material gains shear strength due to force chains oriented in the direction of the maximum stress [Cates et al., 1998]. Depending on the number, length and orientation distribution of such chains shear deformation might be stable or unstable. Stick-slip is therefore interpreted as a cyclic setup and breakdown of force chains, the frequency and size of which should be a function of grain size distribution [Mair et al., 2002]. Furthermore, granular materials exhibit so called 'jammed states', where jamming is induced at high packaging density or by application of shear stress [Bi et al., 2011]. We corroborate this view as large slip events are associated with compaction while the interseismic is characterized by accelerating creep and dilation (Figure 3.2).

The normal stress is one of the critical factors that control the creep threshold of the system. For low normal stresses it is easier for the grains to rearrange during the creep phase. Firstly, this results in higher background slip of grains that exhibit a much lower normal stress along their contacts and can easily slide along each other. Secondly, the ratio of normal stress to dilational stress, that pushes the grains apart when sliding over the rough internal shear zone, is smaller. Therefore, force chains are less effective in strengthening the material.

The occurrence of small precursory slip events is in accordance with other studies that show transient effects during the transition of the stick phase to dynamic slip [Nasuno et al., 1998, Ferdowsi et al., 2013]. Because they are much smaller than the main events it is suggested that the events are the expression of internal reorganization in the granular material. During this internal deformation the grains are jammed and the force chains are rearranged into a more stable configuration. Although creep continues the newly formed granular package is stronger than the previous package and therefore a short period of quiescence without slip events occurs. This rearrangement can occur several times during the late interseismic phase. If the internal structure reaches a critical threshold, probably determined by the contact ratio and packing density, a runoff process starts and the system changes from creeping to dynamical slip.

Other studies have shown a similar system behavior that is attributed to intermittent criticality [Ben-Zion et al., 2003]. In contrast, to the self-organized critical system, intermittent criticality implies a cyclic evolution of the fault zone, wheras the SOC only gives a general statistic fluctuation around the critical state (i.e. failure criterion). If we apply the concept of intermittent criticality, the small precursors are the expression of small scale stress perturbations along the fault zone. Overall the stress field within the granular fault zone homogenizes by increasing rearrangement of force chains, that explains the increasing frequency of precursory events up to a certain point. Then the system is largely homogenized and is in a critical state, very close to failure, which is comparable with the state of stress in the lithosphere [Sornette et al., 1990]. This behavior has also been observed for the temporal and spatial clustering of smaller earthquakes [Hainzl, 2003].

The behavior of dilation during the interseismic cycle is even more complex and it is difficult to assign a direct relation to micromechanical processes. The observed increase in wavelength of the small amplitude oscillations could indicate a smoothing of the internal fault surface, leading to a smoother frictional response. The discrete upward and downward steps might be artificial, or the result of sensor noise. However, the strong reproducibility over multiple cycles indicates that mechanical explanations can be valid, too. For example, internal reorganization of the granular packaging leads to discrete conformations of packaging with different densities that are characteristic for each state of the system.

3.5.2 Effect of creep on rate and state relations

We test if interseismic transients have an effect on the rate and state relations that can be determined by looking at the velocity and time dependence of friction during each experimental series. In rate and state friction three key parameters are determined, the direct effect a, the healing effect b, and the state evolution variable ϕ [Dieterich, 1979a, Marone, 1998]. From our type of experiments we can not observe the evolution of friction directly because our system is inherently unstable. This is due to the system stiffness k_L which is below the critical stiffness k_c. Therefore we can only infer the amount of weakening depending on loading velocity $(a-b)$ and the relation of loading velocity and recurrence time $V_L = C\, t_r^n$ [equation (5) in Beeler et al., 2001].

The main events show typical scaling of peak strength μ_p with loading velocity V_L. From this the rate-and-state parameter $(a-b)$ is derived because peak strength is the onset of dynamical failure and at that point the slip velocity V equals the loading velocity V_L [Rosenau et al., 2017]. We fit the curve with a power law of the form $\mu_p \propto V_L^n$ with $n = (a-b)ln(10)$ (figure 3.5a+c). This shows that the glass beads are velocity weakening with $(a-b)$ ranging from -0.011 to -0.017 which leads to a reduction of peak strength by 1.1 to 1.7 % per e-fold increase in velocity.

There is no significant difference in the estimate of $(a-b)$ from soft and stiff systems, as expected for a material property. The scaling of strength at the onset of slip is consistent with the findings of Beeler et al. [2001] who show the same type of scaling. The scaling coefficient typically attributed to natural rocks or gouge in the seismogenic zone, is in the same range (-0.011 to -0.015 [Beeler et al., 2001]; ≈-0.01 [Scholz, 1998]; -0.001 to -0.01 [Dieterich, 2007]). Other analog model studies have used $(a-b)$ values in the same range to model seismotectonic processes with other materials (gel on sand paper: -0.028 [Corbi et al., 2013]; rice: -0.015 [Rosenau and Oncken, 2009]; cacao, ground coffee, and others: [Rosenau et al., 2017]). Therefore, we consider our models to be dynamically similar to the natural prototype, to rock deformation experiments in the MPa-range [e.g. Tullis and Weeks, 1986], and to numerical simulations of rate and state friction [e.g. Ferdowsi et al., 2013].

Usually, slide-hold-slide tests are used to determine the healing effect b which scales as $\Delta\tau_p \propto bln(t_h)$, showing that with increasing hold time t_h the strength of the material is increasing. As described in section 3.4.1, the interseismic creep and precursors strongly affect the recurrence behavior of main events, essentially making them not predictable by classical laws of predictability. Due to the interseismic deformation the fault zone is not at complete rest, which would be the case for a stress relaxed slide-hold-slide test.

According to Beeler et al. [2001] if time-dependent strengthening is present the scaling relation of loading velocity and recurrence time $t_r \propto V_l^n$ shows an exponent $n > -1$. For the stiff

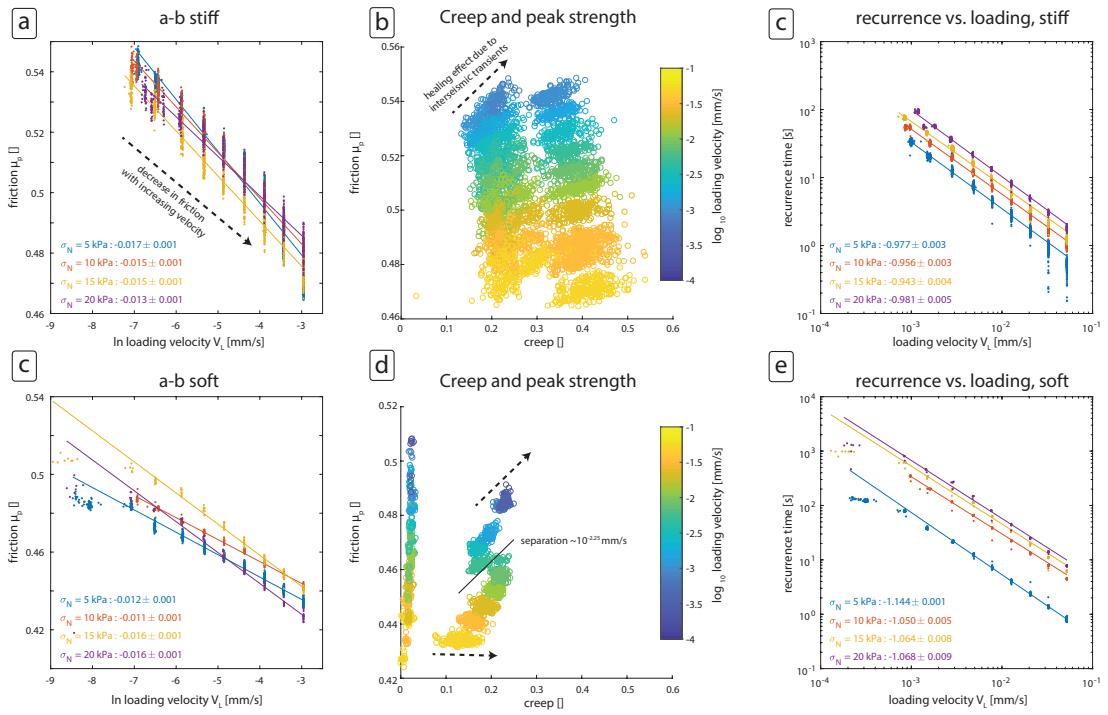

Figure 3.5: (a+c) Data and scaling of peak friction with loading velocity in the form of $\mu_p \propto (a-b)\,ln(V_L)$. The values given are the parameters (a-b) with the corresponding 2σ confidence interval. (b+d) Effect of creep on peak friction. Higher creep correlates to higher peak friction, for each individual velocity step (color-coded). (c+e) Scaling of recurrence time with loading velocity after Beeler et al. [2001].

experiments n is between -0.981 and -0.943 which shows that a time-dependent healing effect leads to a strengthening of the fault zone over the recurrence interval (Figure 3.5c). So what is a possible source of time-dependent strengthening in our system? To some extend interaction on the individual grain scale, such as electrostatic and van-der-Waals forces between the individual glass beads can lead to a certain healing effect. We then also would expect a visible healing effect in the soft system which is not the case. For the soft system we even observe a time-dependent weakening. As a result, the scaling of loading velocity and recurrence has an exponent of $n < -1$.

The major difference between the soft and the stiff system is the amount of creep and the occurrence of precursors. Therefore, we compare the correlation of creep, that includes precursors for the stiff system, and the peak friction at the onset of dynamic failure (Figure 3.5b+d). We observe an increase in peak friction in the stiff system for each individual loading velocity and normal load (Figure 3.5b). For the soft system we do not observe a correlation for most normal loads, because there is only a small amount of creep. The experiment with low normal load (#spr5k) does show 10 to 30% creep, but also has the lowest scaling exponent of $n = -1.144$. For high loading velocity ($> 10^{-2.25} \frac{mm}{s}$) the neutral to negative trend is visible (Figure 3.5d). Below that we suspect a separation (solid line in Figure 3.5d) because for lower velocities the overall amount of creep drops and we observe an increase in peak friction. Accordingly, we assume that slow creep during the interseismic phase only leads to a small strengthening effect, and that the fault healing is dependent on the loading velocity as was already mentioned by Marone [1998]. For the described experiments we think that the precursor slip events have a strong strengthening effect on the experimental fault zone. As a result the evolution of the frictional state ϕ during the interseismic phase is affected by micromechanical rearrangement.

While the scaling of peak friction μ_p with V_L is similar for both systems, we observe that the scaling for final friction μ_e, where the system comes to rest after dynamical failure, is very different for both systems. For the stiff system it is more or less constant for all loading velocities, whereas for the soft system it changes. Therefore, we think that the unloading stiffness of the system plays second order role because it influences the slip distance during an event which is higher for lower unloading stiffness. Consequently, this leads to a different evolution of localization phenomena inside the shear zone, which may weaken the material resulting in $n < -1$.

3.5.3 Comparison with natural systems

3.5.3.1 Magnitude size distributions

The magnitude size distribution of natural earthquakes follows the Gutenberg-Richter relation where the cumulative number of events decreases exponentially with increasing magnitude ($\sum N(M) \propto M^{-b}$). Therefore the b-value indicates the relative proportion of small events compared to big events. In the following, we use dynamic stress drop $\Delta\tau$ as a proxy for magnitude. It is linearly related to seismic moment M_0 in our system because σ_N and fault surface A is constant for one experiment:

$$M_0 = \Delta\tau\sigma_N A^{\frac{2}{3}} \tag{3.5}$$

Seismic moment is then logarithmically related to moment magnitude M_w:

$$M_w = \frac{3}{2}(log_{10}M_0 - 9.1) \tag{3.6}$$

Experiments with a high stiffness show power law type scaling for the precursory part of the probability distribution with a b-value being smaller than 0.2. In the size interval that is characteristic for the larger main events, the distributions do follow a more Gaussian like behavior and probably shows the stress drop that is characteristic for the fault zone in the ring shear tester. In contrast, for low stiffness the distributions are characterized by power law scaling with $b \approx 1.5$ for normal stresses greater than 5 kPa and $b \approx 2.2$ for experiment #spr5k. The low stiffness distributions more closely follow a G-R type shape with a sudden drop off at larger magnitudes. Where the power law distribution is present, we see that b-value decreases with increasing normal stress. This is in accordance with natural observations, that for highly stressed fault zones the b-value of the earthquake distribution becomes smaller [e.g. Schurr et al., 2014].

3.5.3.2 Moment - duration scaling

Another parameter that is frequently obtained for the scaling behavior of earthquakes is the relation of seismic moment and event duration [Ide et al., 2007, Gomberg et al., 2016]. In general, slip events that grow without bounds within a fault zone show a scaling of $M_0 \propto T^3$ (e.g. earthquakes). In contrast, slip events that span the complete spatial scale of the system and only grow along the fault zone, show a scaling of $M_0 \propto T$ (e.g. slow slip events).

In terms of moment magnitude M_0 - duration T scaling after Ide et al. [2007], the precursors cover a very broad range of durations at low magnitude. Therefore, it is not possible to assign a scaling law to them, due to a cross correlation coefficient of 0.02. The cross correlation of $log\, M_0$ and $log\, T$ for the main events is low but reasonable (0.55 - 0.76). The scaling of moment with duration is a power law but with a low goodness of fit for most experiments. Moment scales with duration by $M_0 \propto T^n$ with $n = 0.1$ to 0.3 for experiments without spring and $n = 0.4$ to 0.5 for experiments with spring. This is much smaller than what is observed for natural systems. A possible reason is that the actual duration of an event is much smaller than observed. During the measurement of the unloading stiffness k_u we observed shorter durations using a high-speed camera at 10 kHz. If the actual duration is not linearly related to the measured duration this would increase the power law exponent. Additionally, the definition of earthquake duration is different for natural systems (seismograms) and our model (stress drop duration) which makes it difficult to compare the absolute values.

Furthermore, we consider this a second order feature of our model which may not necessarily be correctly scaled to nature. In order for the analog model to be scaled geometrically it is mandatory to scale the critical slip distance L_c of glass beads to those of fault gouge. Therefore, the total slip during an event is not scaled properly but the model is dynamically similar because the non-dimensionalized dynamic parameter (a-b) is similar.

3.5.4 Effect of creep on predictability

Although the stick-slip oberserved is highly regular and characteristic, application of simple time and slip predictable recurrence models seem to fail: Comparing the predicted with observed recurrence and observed stress drop for the experiments without spring shows that the majority of points plot away from unity (solid line in Figure 3.6a+b). As a result, the models for predictability are not able to predict the observed parameters. For lower normal stresses the prediction error increases systematically. The observed recurrences and also stress drops, are up to twice as high as the predictions. For experiments with a spring only the σ_N=5 kPa experiment

shows a significant deviation from unity (Figure 3.6c+d). An increase in normal stress for the low stiffness experiments leads to highly predictable stick-slip events.

However, the recurrence models can be corrected for interseismic creep resulting in a significant improvement of predictions. We observe a direct correlation between forecast error and amount of creep: Events that show a high amount of creep plot close to the dashed lines in figure 3.6. For 50% creep the observed stress drop is approximately half the size than what is predicted by equation 3.3. When the predictions are normalized by the amount of creep in the observations, the highest forecast error of -0.60 drops to -0.08 for slip predictability and from 0.38 to 0.07 for time predictability. The normalized predictions still show an increased forecast error for high loading rates.

To summarize, creep at low shear stress retards loading and extends the interseismic phase. i.e. the time until the peak strength is reached. Simple recurrence models tend consequently to overforecast stress drop and underforecast the recurrence time. Because this effect is systematic it should be taken into account when applying simple recurrence models. We interpret the precursory events as being similar to repeating transient events, such as slow slip events, due to their frequent occurrence before a slip event. If the right conditions are met by tuning stiffness, normal stress and loading velocity, the precursors are very regular and can occur multiple times before a main event. When the system is close to the stability boundary in the rate and state framework very subtle perturbations of the system leads to dynamic failure. Furthermore, the regular pattern of the dilation seems to indicate that the granular fault zone does undergo recurring patterns of internal configuration of force chains.

3.6 Conclusion

We present an experimental setup which is able to generate regular stick slip events in an analog fault gouge to study their dependence on different extrinsic parameters. The slip events reproduce typical characteristics that have been observed in similar experiments in other experimental setups and materials allowing to generalize the observations to natural occurrences of earthquakes. Accordingly, transient phenomena considerably alter the predictability of the slip events and should be taken into account for time-dependent recurrence models of seismic hazard assessment. In the experiments, micromechanical rearrangement in the granular package is the major process leading to the observed precursory strengthening and the short period of quiescence before a slip event. The magnitude size distribution of larger events is strongly affected by precursory phenomena and a characteristic scale separation of precursors and larger events is present. We conclude that transients and precursors can strongly affect the statistical characteristics of a single fault zone system. The small scale events during the precursory phase are the expression of distributed fluctuations of the system in a critical state. Further examination of these fluctuations and their correlation with the generation of large events may give important constraints on the predictability of slip events [as suggested by Ben-Zion et al., 2003]. Furthermore, the addition of interacting faults could provide additional insights into the system behavior at conditions that are more close to a natural fault zone.

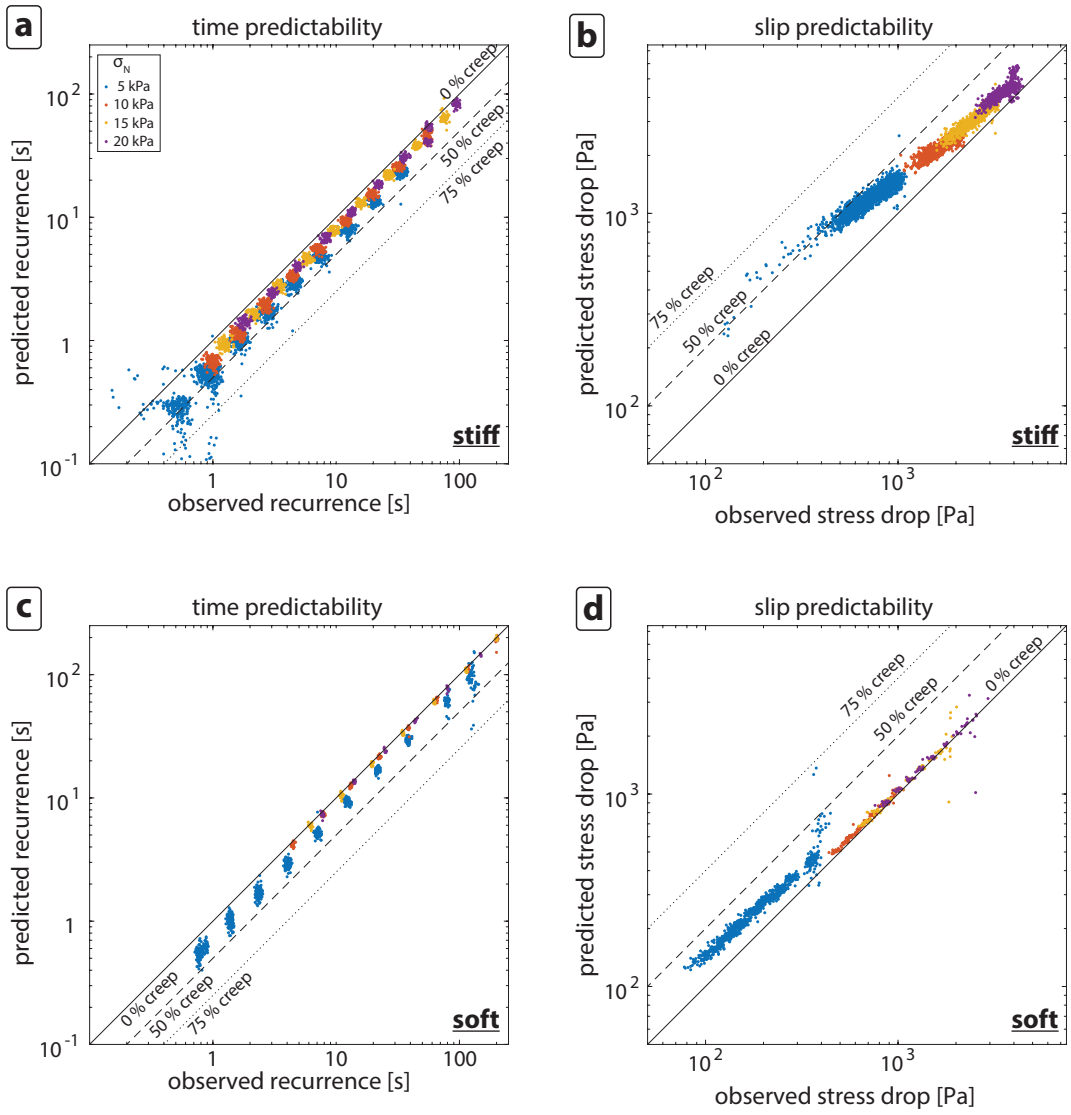

Figure 3.6: Comparison of predictions and observations from the recurrence and stress drop based models. The dashed lines indicate perfect predictability taking a specified amount of creep into account. (a) Time predictability for experiments with high stiffness. All points plot away from unity which results from the higher amount of creep. (b) Slip predictability at high stiffness shows that the predictions are higher than the observed stress drops with an increasing prediction error with decreasing normal stress. (c) Results for time prediction of the low stiffness experiments. Most slip events lie close to the unity and only the low normal stress experiment shows a stronger shift due to higher creep. (d) The slip predictability also shows that for higher normal stress the slip events are nearly perfectly time slip predictable.

Chapter 4

Smart speed imaging in Digital Image Correlation: Application to seismotectonic scale modelling

M. Rudolf[1], M. Rosenau[1], T. Ziegenhagen[1], J. Bedford[1], V. Ludwikowski[2], T. Schucht[2], H. Nagel[2], O. Oncken[1]

[1]*Lithosphere Dynamics, Helmholtz Centre Potsdam, German Research Centre for Geosciences (GFZ), Telegraphenberg, D-14473 Potsdam, Germany* [2]*LaVision, Göttingen, Germany*

This chapter is going to be submitted for publication to ***Frontiers in Earth Science, section Structural Geology and Tectonics*** as:

M. Rudolf, M. Rosenau, T. Ziegenhagen, V. Ludwikowski, T. Schucht, H. Nagel, O. Oncken: Smart speed imaging in Digital Image Correlation: Application to seismotectonic scale modelling.

Individual Contributions:

M. Rudolf planned and performed the experiments, analysed the data, and wrote the research paper. M. Rosenau was involved in planning the research, analysing the results and writing. T. Ziegenhagen, V. Ludwikowski, T. Schucht, and H. Nagel facilitated the technical realization of the study. O. Oncken was involved in supervising the research and writing.

Keypoints

- The amount of data generated during an experiment decreases significantly when a dynamic trigger system is used.
- Force measurements are a suitable input to dynamically trigger image acquisition.
- Even for less pronounced stress drops, the reduction of data is greater than 50%.

4.1 Abstract

Elastic stress in the lithosphere releases through slip along preexisting planes of weakness. Slip events may occur on many spatial and temporal scales. They range from short-term localized seismic slip (earthquakes) to long-term distributed slip (ductile shear zones). In the analogue model presented here, we examine the influence of multiple parameters on the slip dynamics and overall statistics of ruptures within a glass bead shear zone. We use a customized rotary shear apparatus (Schulze ring-shear tester) to monitor shear stress during shear. The apparatus allows a direct control of shear rate and normal stress. Digital image correlation is used to measure on-fault deformation.

Because of the rate-and-state frictional properties of glass beads, the used setup produces regular stick-slip events. The events feature statistics similar to natural slip systems, e.g. a magnitude distribution similar to single faults. Estimated moment magnitudes of the laboratory earthquakes range from M_W = -7 to -6. A Gutenberg-Richter like decay up to a certain corner magnitude followed by a characteristic peak is observable. With decreasing loading rate the recurrence time and size of events increases exponentially with exponents similar to natural events. Slip is usually initiated along the high strain rate boundary (outer perimeter), propagates spherically until it reaches the low strain rate boundary (inner perimeter), and continues propagating in a bidirectional manner, as is also true for earthquake slip.

Analogue earthquake and seismic cycle models are characterized by strong variations in strain rate: from slow interseismic loading to fast coseismic release of elastic energy. Deformation rates vary accordingly from micrometer per second (e.g. plate tectonic motion) to meter per second (e.g. rupture propagation). Additionally, deformation values are typically very small over one seismic cycle in the order of few tens of micrometer because of the scaled nature of such models.

Applying digital image correlation (DIC) methods requires image pairs which show deformation significant enough to be detected (usually >0.01-0.1 Px) and therefore the period covered by image pairs of images should scale inversely with the deformation rate. In the presented experiments high speed (>100 Hz) imaging is required to capture the rupture process while slow speed imaging <10 Hz is sufficient for interseismic loading given the accuracy of the DIC method in this application (ca. micrometer). In order to prevent over-sampling of the cyclic process to acknowledge transmission and storage capacity limits we developed a tool which allows on-the-fly scaling of imaging frequency with strain rate based on an external trigger signal and a ring buffer. The external trigger signal comes from a force sensor that independently detects stress drops associated with analogue earthquakes triggering storage of a short high frequency image sequence from the buffer. After the event passed, the system returns to a low speed mode in which image data is downsampled until the next event trigger. Using this tool, we are able to reduce the image data by a factor of at least 10 from 3 TB for a typical experiment to less than

300 GB. In future, we plan to implement an on-the-fly virtual strain meter in the DIC software in order to trigger high-speed imaging internally instead of externally.

4.2 Introduction

During earthquakes elastic stress and strain is suddenly released in the lithosphere, causing abrupt relative motion of two adjacent crustal blocks. The released energy is partially transformed into the generation of seismic waves and can cause major damage to structures in the vicinity of the epicentre [Hyndman and Hyndman, 2016]. Earthquakes are usually bound spatially to a discontinuity (e.g. fault, or fault zone) and often occur in a quasiperiodic manner over geological timescales (ka to Ma). According to the elastic rebound theory, each earthquake is preceeded by a period of seismic quiescence, followed by the earthquake and associated postseismic deformation [Reid, 1910]. This cyclic behaviour is termed 'seismic cycle' and is the basis for assessing the geologic evolution of a seismogenic fault and the seismic hazard associated with it [Scholz, 2010].

The seismic cycle is characterized by strongly contrasting strain rates in the interseismic and coseismic phase. During the interseismic period the system is frictionally locked, loaded at low rates (mm/a) and elastic strain gradually builds up [Tse et al., 1985, Schurr et al., 2014]. In some cases the fault is not completely locked and shows slow creep deformation, e.g. in the form of slow slip events [Ide et al., 2007, Bürgmann, 2018]. If the accumulated strain leads to stresses that exceed the frictional strength of the locked patch, a slip event nucleates and results in an earthquake with slip velocities in the range of m/s. After an earthquake the plate interface still shows some activity, usually due to hetereogenous distribution of stress and viscoelastic relaxation of deeper segments. This is called postseismic deformation and is expressed as seismic and aseismic afterslip on the fault [Omori, 1894, Utsu, 1961].

Although the recurrence behaviour of earthquakes on a single fault is quasiperiodic, under the assumption of constant loading rates and frictional parameters, it is not possible to predict the onset of seismic slip [Ben-Zion et al., 2003]. Therefore, numerical simulations and physical experiments have been designed to model fault slip and the seismic cycle [Rosenau et al., 2017]. Because of the multiscale nature of fault slip, many numerical simulations are limited to either short (e.g. rupture models) [Heinecke et al., 2014] or long timescales (e.g. geodynamic models) [Dinther et al., 2013]. Only few numerical techniques allow the combination of short term and long term processes, and frequently the parametrization and implementation of the non-linear, multiscale interactions between the long and short timescales remains difficult [Avouac, 2015]. Scaled physical experiments (analogue experiments), allow to address the multiscale nature of slip on a laboratory scale and may provide additional insight into the deformation over multiple seismic cycles. Even though the analogue experiments are strong simplifications of a seismogenic fault system, they inherently show stick-slip dynamics without the need of a complex integration scheme [Caruso et al., 2007, Marković and Gros, 2014].

The strong variation of slip rate during the interseismic and coseismic period is the main challenge for monitoring the physical experiment (Figure 4.1). The experiments are commonly monitored with cameras at a constant frame rate, that is adjusted to the high coseismic velocity. The images taken during the experiment are then processed using digital image correlation which yields the displacement field of slip on the fault. Ideally the experiments are run for a long time, to supply a large number of seismic cycles under constant experimental conditions,

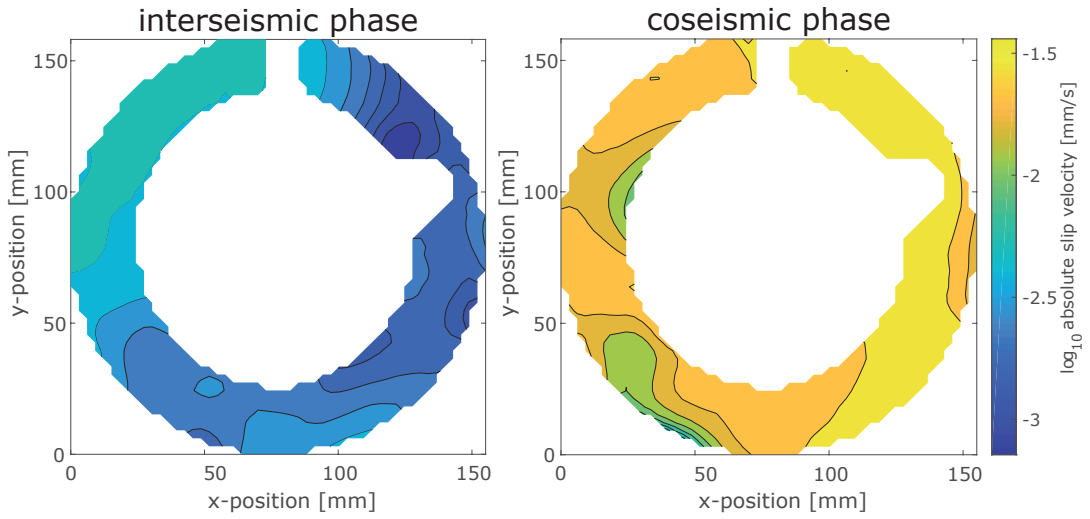

Figure 4.1: Comparison of the slip velocity in the experimental setup during the interseismic (left) and coseismic (right) phase. The slip velocity during an event is almost 2 orders of magnitude higher than during the interseismic phase. The colorbar is valid for both plots.

for a good statistical analysis. This usually requires large amounts of data to be stored during an experiment which either is limited by the total amount of storage available (e.g. on the harddrive) or by the maximum rate of data transfer (e.g. memory to harddrive). Furthermore, the processing of the interseismic deformation is difficult for constant framerates, because of the very low signal-to-noise ratio.

In this study we present a new technique which allows for constant monitoring of a physical experiment over multiple seismic cycle analogues. The setup provides in-situ monitoring of shear stress and dilation, under variable normal stresses and loading rates. The measurements coming from the setup are used to trigger a switch from low to high framerates, resulting in drastically reduced amounts of data generated by the monitoring system. Moreover, the trigger system is combined with a ring buffer of images, supplying a temporary storage, which is used to fetch a certain amount of older images previously taken. This allows to increase the total duration of an experiment, while maintaining the ability to monitor the onset of seismic slip and the coseismic deformation at high rates.

4.3 Experimental Setup and Methods

To produce regular stick-slip oscillations we utilize a rotary shear apparatus (ring-shear-tester), normally used for testing granular material properties [Schulze, 1994]. Two different sets of experiments are used to show the performance and suitability of the triggering mechanism. The first configuration uses the ring-shear-tester in standard configuration, filled with rice which produces strong stick-slip events that are very regular. The second configuration is a rotary version of typical block sliders, featuring an annular gelatine block that slides on glass beads.

4.3.1 Experimental Setup

A Schulze ring-shear-tester [Schulze, 1994] is used as a base for the experimental setups. This machine measures shear forces during rotary shear of a granular material [e.g. sand, glass beads;

see also Panien et al., 2006]. During the experiment, it is possible to vary normal load and shear velocity. The ring-shear-tester uses a cantilever in combination with a motorized weight to hold a constant normal load. The cantilever pulls the lid downwards onto the sample inducing normal stresses of 0.5 to 20 kPa. A digitally controlled motor rotates the shear cell at velocities V_L from 8.3x10.$^{-4}$ to 5x10^{-1} mm/s. For the experiments in this study, we use velocities from 8.3x10^{-4} to 1.6x10^{-2} mm/s and normal stresses between 5 and 20 kPa. A twin beam system coupled to inductive displacement transducers measures the shear forces during the experiment at a high frequency (12.5 kHz). Averaging over 20 samples leads to an effective frequency of 625 Hz with most of the noise removed. The stiffness of the complete experimental setup is 1354 Nm [Schulze, 1994].

4.3.1.1 Standard Configuration

We use the ring-shear-tester in standard configuration with an annular shear cell that has an inner sample diameter of 10 cm, an outer diameter of 20 cm, and a thickness of 4 cm, as described in Schulze [1994]. The aluminium shear cell has a high friction bottom, defined by evenly spaced grooves. As granular material we use a typical 'thai' rice (sample 'RI-1', Table 4.1), which has previously been found to show ideal stick-slip characteristics that are needed to test the triggering algorithm [Rosenau et al., 2009, 2017]. A rigid, aluminium lid, with lamellae providing a high friction interface, is placed on top of the rice. The upper surface of the lid is covered with a white-on-black random pattern of dots, which is ideal for the digital image correlation.

4.3.1.2 Block Slider Configuration

For the block slider model, we use a 10 mm thick annular shear cell (other dimensions equal to the standard configuration), which is completely filled with glass beads (samples 'GB-1' to 'GB-3', Table 4.1). On top of the glass beads an annular ring of gelatine provides elastic boundary conditions. The shear cell has a bottom that is covered with a pattern of 2x2x2 mm pyramids which provides a very high basal friction along the bottom of the glass beads. The glass beads are filled into the shear cell according to the procedure given by Panien et al. [2006]. The glass beads are spherical with an average diameter of 300 to 400 μm. For better detection with the image correlation algorithm 10 % of glass beads are coloured with diluted black acrylic paint. We use the same mixture of glass beads throughout all experiments. The rate-and-state frictional properties of glass beads are measured using the same apparatus but in standard configuration. Velocity stepping tests show the influence of shear rate onto the recurrence behaviour, peak strength and weakening of glass beads.

4.3.2 Monitoring System

Over the whole experimental duration the top surface of the lid (standard configuration), or glass bead layer (block slider configuration), is monitored with a variable bit-depth CCD camera (Imager MX4M, by LaVision). Depending on the speed of the observed process the frame rate is adaptable to values between 0.5 and 500 Hz. The observed surface is illuminated by a continuous LED light to prevent changing brightness because of the 50 Hz power grid frequency. The images are calibrated with a rectangular pattern of dots. This calculates the spatial scale per pixel and adjusts for lens distortion.

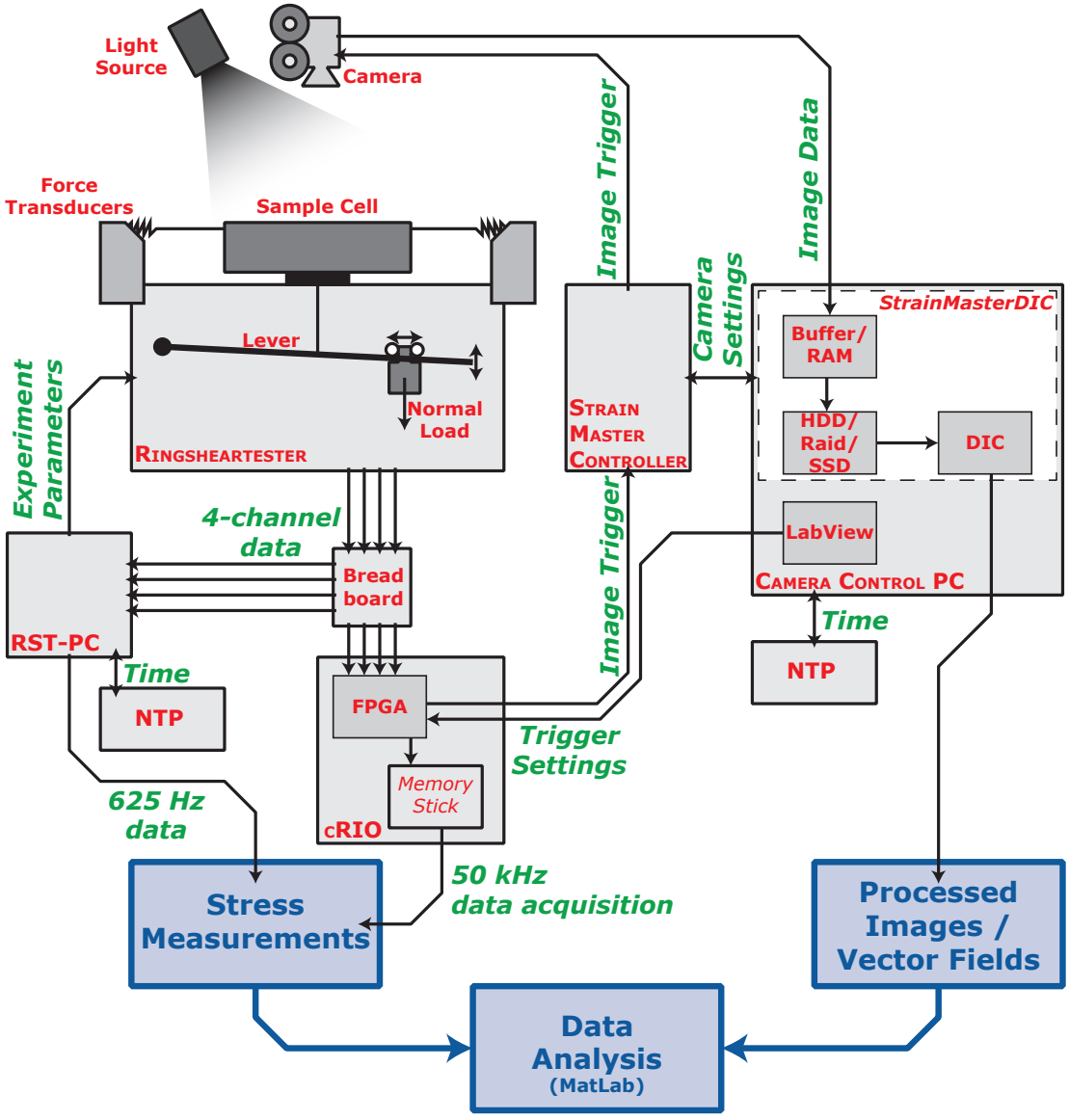

Figure 4.2: Schematic diagram showing the setup and the connections to the monitoring system. The ring-shear-tester is controlled by a computer (RST-PC), which also uses a built in analogue-digital-converter to record the four output channels ($F_{shear}, F_{normal}, \Delta H, V_L$). The CompactRIO (cRIO) is connected to the output channels and currently only provides the triggering at 1 kHz frequency. In a next step, the cRIO is going to bypass the RST-PC to directly control the ring-shear-tester and record the data at 50 kHz. A second computer (Camera Control PC) is connected to the camera system which consists of a controller (StrainMaster Controller) and a software (StrainMasterDIC by LaVision). It supplies the settings for the camera (recording rate, exposure time,...) and stores the incoming image data for digital image correlation (DIC).

Each acquired image has a bit depth of 8 bit which gives 265 grayscale values. In combination with a spatial resolution of 2048×2048px this results in a file size of ≈ 8 MB per image. To get an appropriate catalogue size, the experiments run over at least one hour. Usually, the camera takes a continuous time series of images at a fixed frequency, e.g. 10 Hz. Due to the nature of the modelled system, the deformation during the interseismic phase of a stick-slip cycle is very low. Previously, the acquisition rate was a tradeoff, between the amount of storage available, and the speed of the process. As an example, one hour of continuous measurement at 10 Hz covers 60 to 70 seismic cycles and uses approximately 288 GB of storage. For this study, we developed a triggering system that uses the shear stress measurements from the ring-shear tester to trigger a change in camera frequency from 0.5-1 Hz during the interseismic phase, to 10-25 Hz in the coseismic phase.

4.3.3 Trigger Algorithm

The trigger system consists of an embedded controller (National Instruments, CompactRIO) that is connected to the four channel analogue output of the ring-shear tester and the trigger input of the camera system. The controller does a 50 kHz data acquisition, that is sampled down to 1000 Hz. The FPGA of the microcontroller then uses the input to determine the trigger level by comparing two differences in the signal x (Equation 4.1). The first difference is defined by a moving window of adjustable size over the last t_w samples. A smaller window size is faster but more susceptible to noise. The second difference is the current signal value x_{t0} compared to the last value x_{t-1}. The latter difference must be twice as high as the first difference. This provides a fast response to negative and positive slopes with only a small influence of noise. This factor of two could also be adjustable, but to keep the algorithm simple and the behaviour more predictable we keep it constant.

$$|x_{t0-t_w} - x_{t-1}| > 2|x_{t-1} - x_{t0}| \tag{4.1}$$

This equation is satisfied for positive and negative changes in the observable x. Therefore, the sign of the first difference $x_{t0-t_w} - x_{t0}$ is used to determine whether to trigger on a positive or a negative slope. Furthermore, the moving window size t_w is used as a delay timer t_d to keep the fast response of the trigger but being not too susceptible to noise. This delay timer requires that the above condition (Equation 4.1) is met for a duration of at least t_d before a trigger signal is given to the camera system. To cover the postseismic phase, the signal is hold for an additional duration of t_h once the equation 4.1 is not fulfilled anymore. Due to hardware reasons the trigger signal is inverted at the output, so technically the frequency is low when the trigger signal is active and the frequency is high when the trigger signal is inactive. This is a restriction of the camera system, but our setup is adaptable for other trigger inputs (±5 or ±10 V, various rise behaviours).

Inherently, the trigger system is only activated when a slip event is already happening (Figure 4.3). Therefore, it is combined with a ring buffer of images which is constantly filled with images. The amount of images in the buffer can be set in the software. In this study the number of images in the buffer is set to be the number of high-speed images between two subsequent low-speed images. The camera control software (StrainMasterDIC 1.1.0 by LaVision) runs the camera at high speed and only fetches images when needed. Two different acquisition frequencies are realized by giving the high speed frequency and a division factor which slows down the acquisition

when no slip event is happening. As soon as a trigger is detected, all images in the buffer are fetched and stored. The delay between trigger signal and reaction of the camera system is in the order of a few μs. Then it continues recording at high speed until the FPGA switches back to slow mode. If the two window sizes are well adjusted, the complete onset of the slip event and the postseismic effects are recorded at high speed, whereas the interseismic phase is covered at reduced rate.

For this study we used the shear force signal as an input of the trigger algorithm. The system is designed to use all available channels if needed, either independently or simultaneously on multiple channels.

4.4 Results

4.4.1 Slip Events in the Different Configurations

Both configurations show quasiperiodic stick-slip oscillations of varying amplitude and recurrence (Figure 4.4A). The test experiment in standard configuration was carried out at a loading rate of $V_L = 8.2 \times 10^{-4}$ mm/s and a normal stress of 5 kPa. The strength of the rice grains is relatively high and reaches values above the normal stress several times, which means that the frictional strength μ is greater than 1. The resulting stress drops $\Delta\tau = 3650 \pm 150$ Pa, are also two orders of magnitude higher that for the block slider configuration (Figure 4.4C). The recurrence time t_{rec} is very regular and is 18.3 ± 2.3s. The duration of a slip event in rice is around 0.1 s. The ratio between recurrence and duration is very high ($\frac{t_{rec}}{t_{dur}} \approx 360$), and as a result the potential for saving image data is very high.

In the block slider configuration three different shear rates are realized, which are in the range of the targeted values for the application of the trigger setup. Shear rates range from 8.2×10^{-4} to 1.7×10^{-2} at normal stresses of 5 kPa. The slip events in the block slider configuration are of much lower magnitude than in standard configuration with median stress drop ranging from 27±8 to 41±14 Pa (Figure 4.4). Furthermore, they are less regular and have a less homogenous magnitude-size distribution, log-normal instead of normal, especially at the highest shear rate the events cover a broad range of stress drops. The recurrence time decreases with increasing shear rate, which is an expected behaviour for this rate-and-state-dependent material. At the

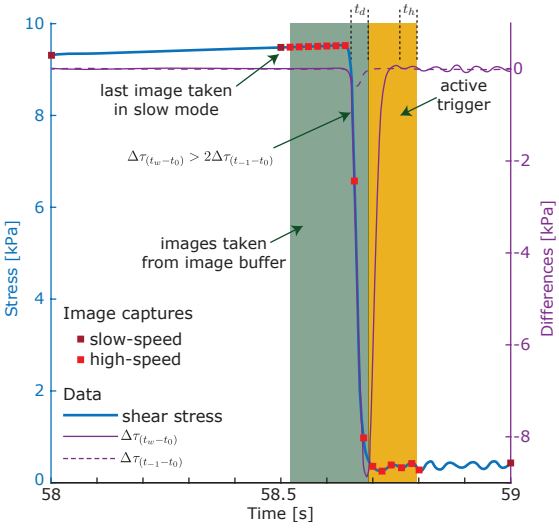

Figure 4.3: Behaviour of the trigger algorithm during an experiment, denoted by the two purple curves. Red squares show the time when images are taken, dark red is the slow-speed acquisition at 2 Hz and bright red is high-speed at 50 Hz When the shear stress (blue) starts to drop, the equation 4.1 is satisfied very early. Then the delay timer t_d defines how long equation 4.1 has to be satisfied before the trigger becomes active (yellow area). As soon as the trigger is active, the camera fetches all images that are stored in the image buffer. When equation 4.1 is not satisfied anymore, the trigger signal is held active for the hold time t_h to capture possible afterslip or post-event effects.

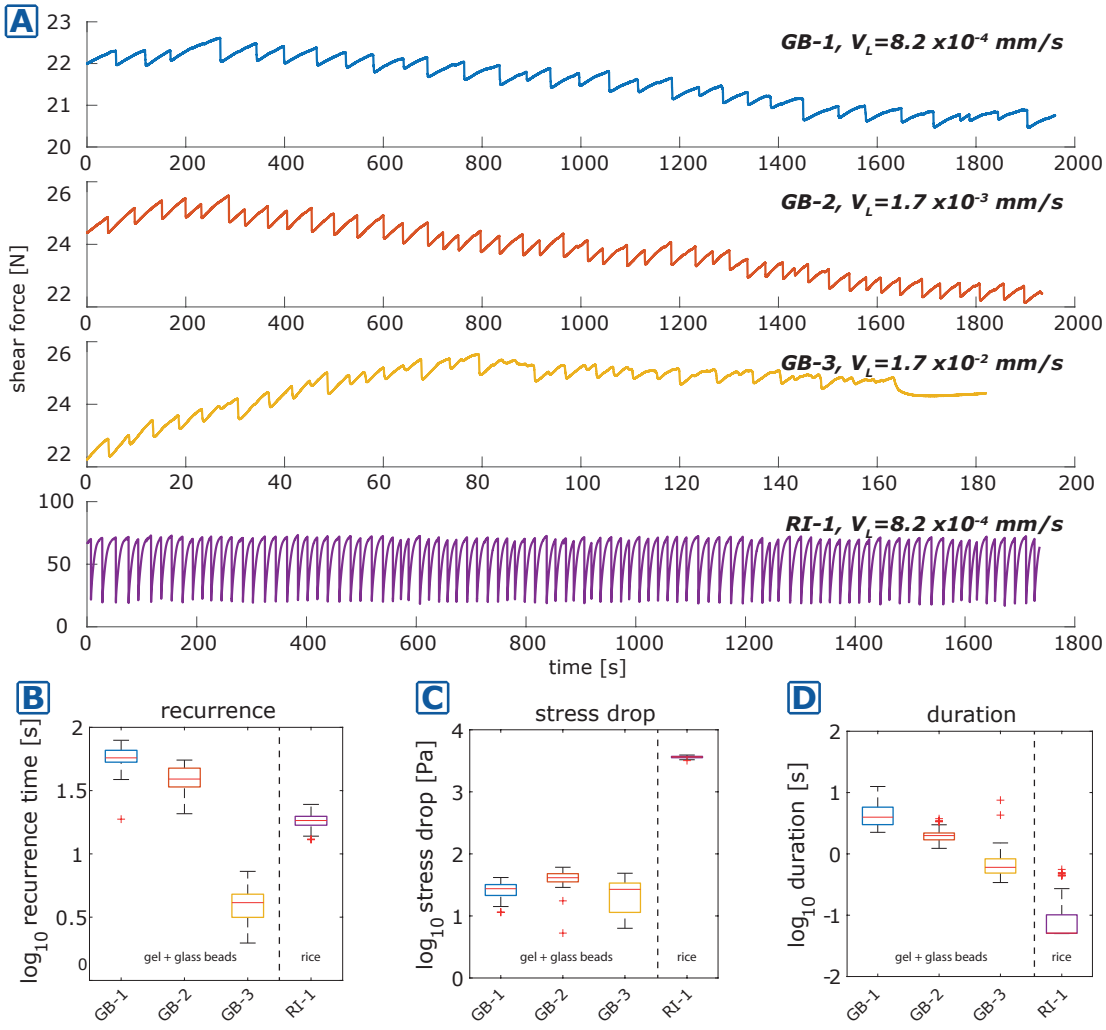

Figure 4.4: Shear force curves and characteristic parameters derived from the stress measurements. (A): Shear force measurements during the experiments with a characteristic saw-tooth shape. The y-axis is shear force in Newton and the x-axis is time in seconds for all experiments. (B): The realized recurrence times cover two orders of magnitude and are similar for both setups. For higher shear rates the recurrence time is significantly reduced, which is in accordance with the rate-and-state-dependent friction. (C): Stress drops cover the same range for the block slider configuration and is much higher for the standard configuration. This results mostly from the stiffness of the setup, which is several orders of magnitude higher in the standard configuration. (D): The duration of the events decreases with increasing shear rate. The detected durations of the rice stick-slips are very low and truncated at 0.1s.

highest realized shear rate the recurrence time is reduced by one order of magnitude from around 60s down to 4s. This is due to the occurrence of some smaller precursory events, also reflected in the lower tail of the stress drop distribution. The duration of slip in the block slider is also decreasing with increasing shear rate and ranges between 0.6±0.6 and 4±2 s. The resulting ratio between duration and recurrence is in the range of 14 to 20 for the two lower shear rates and 7 for the higher shear rate.

4.4.2 Trigger Algorithm

The amount of data saved during the image acquisition ranges between ≈50 and 95% (Table 4.1). Experiments which show a very regular and ideal stick-slip behaviour show the highest amount of data saved (GB-1, GB-2, and RI-1). If the slip events are less regular, or are dissected by transient slip events that are much slower than the actual event, the algorithm triggers more often, and therefore more data is produced (GB-3). Nevertheless, the trigger system is able to save more than 50 % of data. Slight refinements to the detection thresholds or frame rates can help to push this limitation a bit further. Correctly adjusting the window size to the faster events lowers the amount of false detections and a higher 'slow' framerate helps to cover the slower events with more accuracy.

Table 4.1: Recording rates and data savings per experiment.

No.	V_L	Framerate		Images		Data		Savings
	mm/s	low	high	taken	full	used	full	
GB-1	8.2×10^{-4}	0.5 Hz	10 Hz	1930	18635	8.6 GB	82.9 GB	89.6%
GB-2	1.7×10^{-3}	1 Hz	25 Hz	4335	47767	19.1 GB	210.6 GB	90.9%
GB-3	1.7×10^{-2}	1 Hz	25 Hz	1403	2852	6.2 GB	12.5 GB	50.8%
RI-1	8.2×10^{-4}	1 Hz	500 Hz	45260	862913	17.6 GB	335.8 GB	94.8%

The trigger algorithm also decreases the average framerate over the duration of the whole experiment, e.g. ≈26Hz for RI-1. This limits the average amount of images per second from 200MB/s to 10MB/s which enables the use of inexpensive single hard-drive systems instead of a raid configuration. In extreme cases (full resolution and framerate) the camera used in this study produces around 1GB/s which can be lowered to around 100 MB/s, assuming a typical reduction by 90%. Usually this system requires a multi-disk raid that can store up to 1.8GB/s in combination with a large RAM (>128GB) to record images over the duration of 1 hour. This is not needed anymore, when using the provided trigger system.

4.5 Discussion and Conclusion

4.5.1 Time synchronization

Combining experimental results from different monitoring systems requires a reliable time stamp on the images and on the signal data. To synchronize the time between multiple computers in our setup we use the network time protocol (NTP). A specialized software continuously synchronizes each computer with the two network time servers of the local area network at the institute. The network time servers synchronize with GPS signals and the software automatically calculates the delay and offset within the network. This is a standard facility that is necessary for many LAN networks and should be generally available at most universities or research institutions.

If only the internal time synchronization with internet servers is made, e.g. Windows time service, the time difference between two individual computers can be up to several seconds. For seismotectonic analogue models with slip events that occur on the millisecond time scale, this is not feasible. Therefore, it is advised to either use a single computer for everything, or to synchronize the time between the individual devices by using an external clock generator.

4.5.2 Digital image correlation

The reduction of produced images yields much faster processing times for the digital image correlation. This speeds up the typical workflow of an analogue experiment. Additionally, the signal to noise ratio is improved during the interseismic time. Because the framerate is adjusted to the coseismic velocities, the interseismic deformation often is below the detection threshold of the digital image correlation algorithm, which is usually in the subpixel range. Lower framerates during the interseismic time increase the total amount of deformation recorded per image providing a much more accurate estimation of interseismic deformation, that is needed for example to calculate the interseismic locking.

4.5.3 Other Possible Triggering Systems

Our trigger system serves as an a priori reduction of data. A comparable technique is the adaptive time stepping which is often used for numerical algorithms. It is therefore most efficient when the observations are preceded by some sort of precursor, or if additional observations, such as the force measurements, are available. Furthermore, it relies on the temporal storage of images with dynamic access to the ring buffer which is not available for most systems. Some camera systems allow for post-triggering, which means that they have a static ring buffer which is emptied after an event has been triggered. These only support one frame rate, and the triggering process has to be fast enough, that an overflow of the ring buffer is prevented. The triggering can be automated with the presented setup, or manual by visual inspection of the experiment. This technique can be feasible when a reliable signal is not available and should be accompanied by a continuous monitoring at lower frequency with a second camera.

In some cases a reliable secondary signal, such as the force measurements, is not available because the setup is technically not feasible. This is the case for many analogue experiments, like wedges and sandboxes. For these experiments a reliable stress measurement is geometrically hindered or the stress transmission to a sensor is limited. Such experiments can be monitored using a simultaneous strain measurement by digital image correlation. Especially when the observed deformations are too small to be visible by the naked eye, which makes the manual post-triggering impossible. The real-time strain gouge also requires a ring buffer and a performant computer system which is able to compute a quick strain estimation from the images. If these requirements are met, the system is similar to our trigger system and can either use a velocity or acceleration threshold to trigger the high-speed acquisition of images.

If a ring buffer on the computer ram or camera ram is not available, e.g. for consumer grade digital cameras, the above algorithm can be used to do quick a posteriori sorting of images. The images have to be transmitted during the experimental run which is also possible for many standard digital cameras where the manufacturer supplies a specialized software to remote control the camera via USB. Using a script, or the PC component of the embedded microcontroller ('RealTime' for the CompactRIO), the trigger is used to delete the unnecessary

images during the interseismic phase.

In cases where no ring buffer but a signal is available, and the camera system can be manually triggered using a computer or microcontroller, a machine learning based approach may be suitable. For this the camera is always triggered remotely at low frequency. The machine learning algorithm is trained on previous experimental data under the same conditions. It predicts the remaining time until an event happens, which is then used as a threshold to switch to high speed acquisition in time.

4.5.4 Conclusions

Our experiments show that the trigger algorithm is able to greatly reduce the needed amount of storage. The use of a double time-frame approach is easy to adjust, while maintaining a rapid and robust response to changes in the triggering signal. The fully modular specification of the algorithm and hardware system, allows to add further input signals (e.g. acoustic emissions) without major changes. Furthermore, the lower amount of images provides a faster processing speed because less images have to be processed during digital image correlation.

Additional Information

Material Characteristics

With increasing shear rate the friction coefficient μ of glass beads decreases with $(a - b) = -0.014 \pm 0.001$. Fractional stress drop increases with increasing recurrence time which indicates frictional healing during a 'stick'-phase. For rate-and-state friction this is assumed to be exponential with $b = 0.0205 \pm 0.0004$. A second parameter that describes frictional healing is the B-value that describes the effect of shear rate on recurrence time [Beeler et al., 2001]. Shear rate scales exponentially with recurrence time at an exponent of $B = -0.786 \pm 0.004$.

Because the experiments are carried out at room temperature and the required material elasticity is high, we use a highly concentrated gelatine (by ITALGELATIN). Gelatine concentrations range from 20 to 25 wt% which produces a very stiff gelatine with a Young's-Modulus of around 150 kPa. Other seismotectonic analogue models also use gelatine as an analogue for elastic and viscoelastic behaviour, but at much lower concentrations [Corbi et al., 2016]. As a consequence, the preparation technique differs from the one proposed by Di Giuseppe et al. [2009]. For our experiments, the gelatine is mixed with the appropriate amount of cold, deionized water and left to soak for 1 hour. Afterwards, it is molten using a water bath at 60°C and poured into the molds. To reach equilibrium conditions the gelatine is aged for 24 hours at 4°C. Before the experiment it is warmed to room temperature in a drying furnace at 25°C. This also produces a slightly dried surface which is needed to prevent water migration from the gelatine to the glass beads, during the experiment.

Chapter 5

Single Fault Experiments

The previous chapters provide the experimental basis for the development of the analogue model. In the following sections these findings are applied to multiple experimental setups. The first section covers results from the block model with constant near field normal load and variable loading rate (see also Chapter 4). The on-fault displacement is monitored during the experiment, which allows a detailed description of the rupture behaviour. The second section covers the extension of the simplified rotary shear experiments to a more realistic strike-slip configuration including a rheological stratification (elastic + viscoelastic). It has a depth-dependent normal load with constant far field loading rate. For this setup the surface deformation is monitored to gain insights into the deformation of the elastic blocks.

5.1 Fault Block Model

5.1.1 Setup

Results and conclusions shown in this section feature the experimental setup that has been utilized in chapter 4. This setup has two different configurations, one 'half'-elastic and one 'double'-elastic (Figure 5.1). In the following, some exemplary slip events from the double elastic configuration are shown in detail and a preliminary analysis of several experiments is provided.

High dynamic range and high-resolution CCD-cameras are used to acquire images at a frequency of 1 - 50 Hz and with 4 - 11 MPx during an experimental run. The frame rate in the early experiments (up to 56-060) is continous, whereas later experiments employ the newly developed trigger system (Chapter 4). The images are processed with the least squares matching algorithm using DaVis 8 by LaVision [Fleet and Weiss, 2006]. The resulting displacement fields are post-processed using the PIVMat and readimx toolbox in MatLab (Appendix A).

Due to the circular shape of the setup, the displacements during the experiment are circular as well. To better compare the displacement fields with examples using rectangular fault surfaces, the displacement fields are projected onto a rectangular grid (Appendix A.3). Both displacement fields are evaluated using several approaches. From the unprojected displacement field the slip area and slip propagation velocity is determined. The projected vector field allows the analysis of slip direction with respect to the long-term loading conditions. Furthermore, the slip distribution along the fault is analysed using circular profiles.

To make the results comparable, all results presented in this section are derived from one

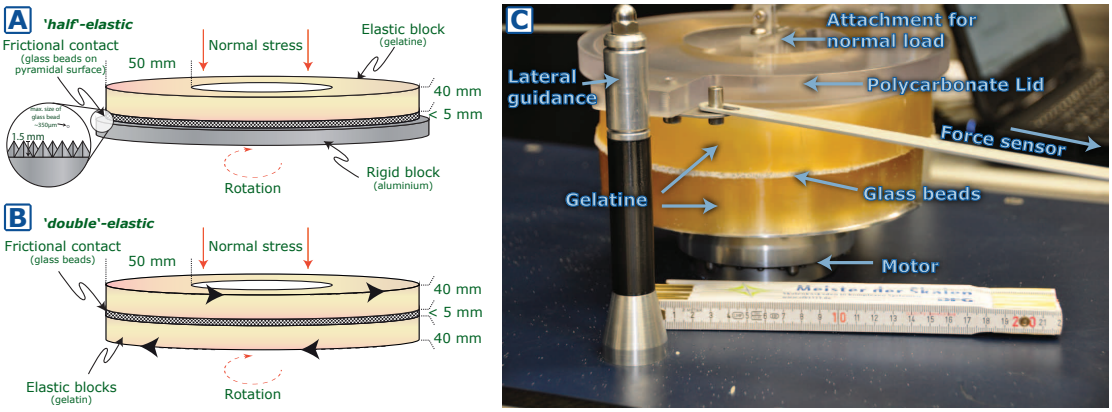

Figure 5.1: Schematic representation of the rotary shear experiments and in situ laboratory setup. In both cases the upper block is held stationary, while the bottom block rotates. Normal stress is applied by pulling on the lid of the setup. (A) 'Half'-elastic configuration where an elastic gelatine ring lies on a layer of glass beads which is on top of a relatively rigid aluminium plate. At the bottom of the glass beads layer a very high surface roughness is achieved through small pyramids engraved into the aluminium (small inset). (B) 'Double'-elastic configuration with two layers of gelatine and a granular shear zone in between. (C) Experimental setup within the modified ring shear tester. The polycarbonate lid is pulled from below with a dead-load weight that is moved along a lever (see also Figure 4.2). The weight of the upper block and lid is counterbalanced by a weight attached to the top of the lid.

experiment (56-039). This experiment shows several slip events of varying size and with differing slip modes.

5.1.2 Observables

5.1.2.1 Slip Evolution during an Event

In this setup, the displacement within the fault is monitored by looking through the upper elastic gelatine block. For each slip event, the nucleation within a small patch (usually a few cm^2) is observable (Figure 5.2A). The slip event shown in Figure 5.2 is a relatively small slip event, which does not rupture the complete extend of the fault zone. In general, slip events almost exclusively start along the outer edge of the gelatine ring. Then slip area continually increases leading to an initial crack like growth in the first phase. When the outer boundary of the gelatine ring is reached the slip event propagates laterally along the surface.

To define the characteristics of slip, horizontal profiles are taken along the fault zone. The red box in Figure 5.2A indicates the area from where the values have been extracted. The profiles are the median values of all vectors along strike within the profile region. Positive values indicate slip in positive x-direction, which is the same as the loading direction (syn-directional).

The incremental displacement along the fault illustrates the rupture propagation and the propagation direction (Figure 5.2B). For this event the rupture starts to propagate leftward after the first two increments. The peak of displacement migrates by approximately 50 mm towards the left. The rupture propagation is therefore anti-directional, which means it is in opposite direction to the loading rate. The rupture velocity is in the range of 10 - 25 mm/s which is about two orders of magnitude higher than the slip velocity.

The total cumulative displacement shows a maximum in the source region and decreases towards the edges of the slip patch (Figure 5.2C). At the edges, the slip direction apparently is

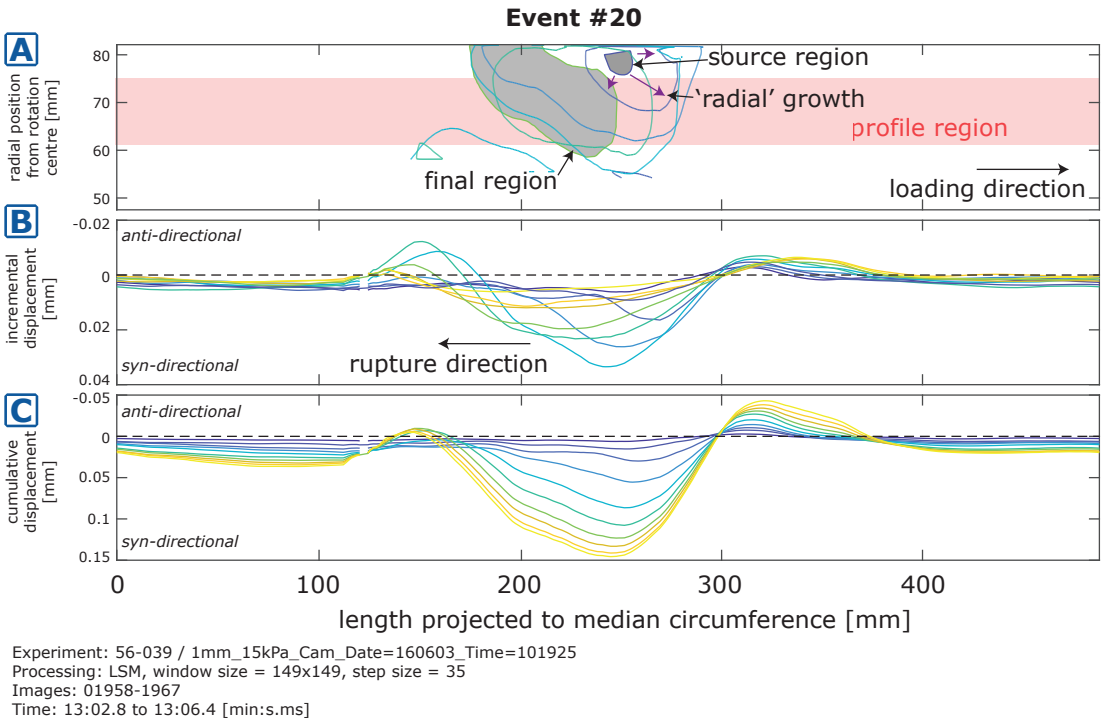

Figure 5.2: Development of a slip event over time which is indicated as colour of the lines (blue = start, yellow = end). The slip event is taken from the same experimental catalogue as Figure 5.4 and 5.5 and has been projected to a rectangular reference system. (A) Contour map showing the contour where slip rate is greater than the loading rate. The source region expands radially and then slip propagates along the rupture area. (B) Incremental displacement extracted from the 'profile region' in (A). The migration of slip is indicated by a shift in the peak slip. (C) Cumulative displacement showing a steady growth over time with a slightly shifted peak in the direction of rupture propagation.

reversed. According to the elastic rebound theory [Reid, 1910] the lower block should move in the same direction as the loading direction of the motor, whereas the upper block should show an opposing movement. As the monitoring system observes the uppermost glass bead layer that is in contact with the upper block the observed slip direction should be anti-directional. The rupture propagation can occur in all directions as it locally releases stress and generates an elastic wave that increases stress in the direction of slip and decreases stress in the other direction. Figure 5.2C shows that slip is syn-directional whereas the rupture propagation is anti-directional. Syn-directional slip may indicate a loss of adhesion of the glass beads to the gelatine ring and therefore movement in the direction of the lower ring.

5.1.2.2 Hypocentre Locations

The source region (hypocentre) of the slip events show a spatial and temporal clustering. In this experiment two main regions can be identified (Figure 5.3). The locations are characterised by differing magnitude and slip direction. They only partially rupture the fault zone and their rupture areas do not overlap. The clustering is most prominent during the initial phase of the experiment. Later slip events are bigger, rupture the complete area and do not show a preference for one of the regions.

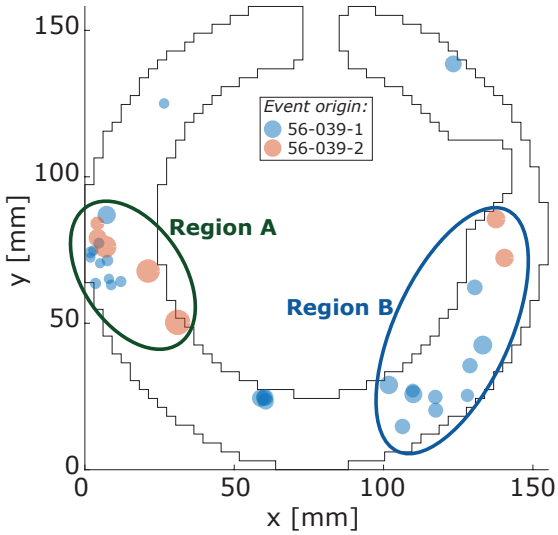

Figure 5.3: Hypocentres of all events that have been detected in two subsequent recordings of the same experiment. The colour indicates the origin and the size is relative to the maximum seismic moment. Two main regions are identified where most events nucleate. A small cluster of events lies in between the two.

The events that initiate in region A are relatively small and show syn-directional slip (Figure 5.4). Most of the small events happen at the beginning of the experiment which later transitions into less frequent but similar larger events (see also Figure 5.9). The majority of very small events themselves cluster within region A as a smaller sub-cluster. This indicates a very stable 'asperity' in that region. In the later stage, especially during the second recording (56-039-2), the events also nucleate in this region.

Slip events that initiate in region B are very often larger than the events in region A (Figure 5.4). Furthermore, they show anti-directional slip and a longer duration. In many cases a larger slip event nucleating in region B is preceded by a smaller slip event in region A, which is also visible as double peaks in Figure 5.9. The small cluster that is visible in the area between the two clusters is only active in the early stage of the experiment (latest event is #10 of 28).

5.1.2.3 Comparison of Two Successive Slip Events

As already mentioned before, the slip events cluster in two different locations. In the following, two successive slip events are shown which illustrate this clustering behaviour and the separation of the shear zone into two regions. They are both taken from the inital phase of the experiment, where the clustering is still pronounced.

The first slip event nucleates in region A and propagates clockwise around the ring. From t_0 to $t_0 + 0.4$, the rupture propagates in all directions (Figure 5.4A). Afterwards it reaches the inner boundary and continues to propagate along the fault zone. The apparent slip direction is syn-directional with the maximum slip along the outer edge of the ring. The propagation of the rupture front is most pronounced during the first 1.2 s of the event. This is expressed by rapidly shifting peaks in the top plot of Figure 5.4B (blueish colors). The propagation speed of the velocity peak is around 40 mm/s. Later on, the incremental slip shows slowly decaying activity over the complete extend of the patch (green to yellow colors). The cumulative seismic moment is around $1.2 \cdot 10^{-2}$Nm which classifies the event as a relatively small event in the experiment (Figure 5.4C and 5.10).

The slip event that follows the above event is larger and lasts about twice as long. It nucleates along the south-eastern outer edge of the ring and rapidly grows in extend (Figure 5.5A). The rupture area only grows within the first few images and then stagnates. It is concentrated in the area which was not ruptured during the last event. The main growth mechanism is not by rupture propagation, but by crack-like increase in displacement over the complete rupture area (Figure 5.5B). The main slip direction is counter-clockwise and therefore anti-directional. Peak displacement and the rupture front gradually move in counter-clockwise direction and the rupture does not propagate in the region between 150 and 300 mm, where the previous event was located. The source time function shows a strong linear increase in the growth phase which is followed by a slower non-linear decay towards the end (Figure 5.5C). The cumulative seismic moment released by this event is approximately one order of magnitude bigger.

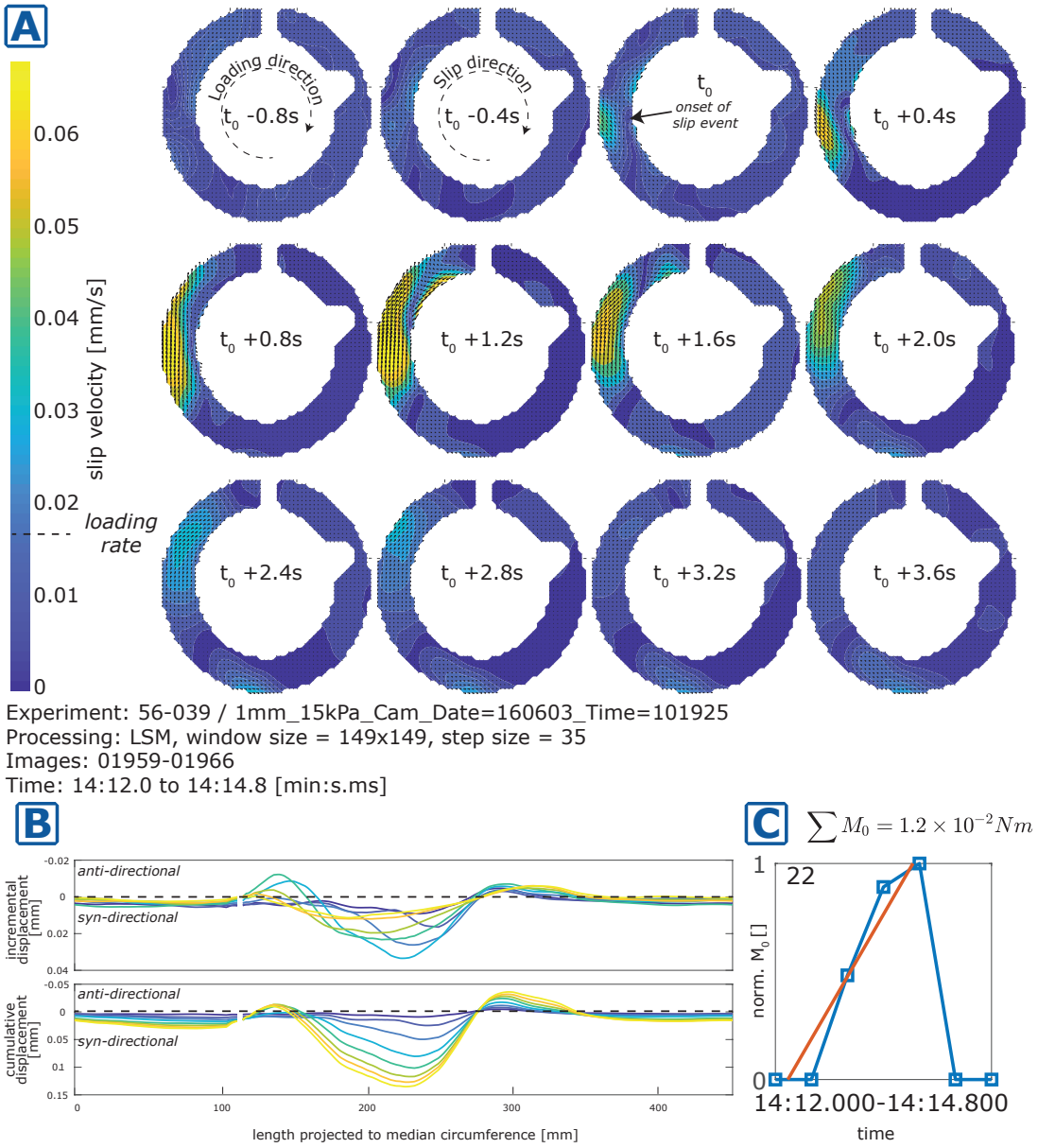

Figure 5.4: Compiled results from a small slip event that has the same orientation of slip as the loading direction (Num. 22 in Figure 5.11). (A) Slip distribution during the slip event. An event is detected when the local slip velocity is above the loading rate. The direction of slip is clockwise, which is equal to the loading direction. (B) Profiles of along-fault slip (incremental and cumulative) for each vector field. The colour indicates the time (blue = start, yellow = end). Co-directional slip is in the same direction as the loading, where as anti-directional slip is in the opposing direction. (C) Source time function showing the increase of seismic moment over the duration of the slip event. The y-axis shows the seismic moment normalized to the maximum seismic moment. The red line shows a linear fit of the rising segment.

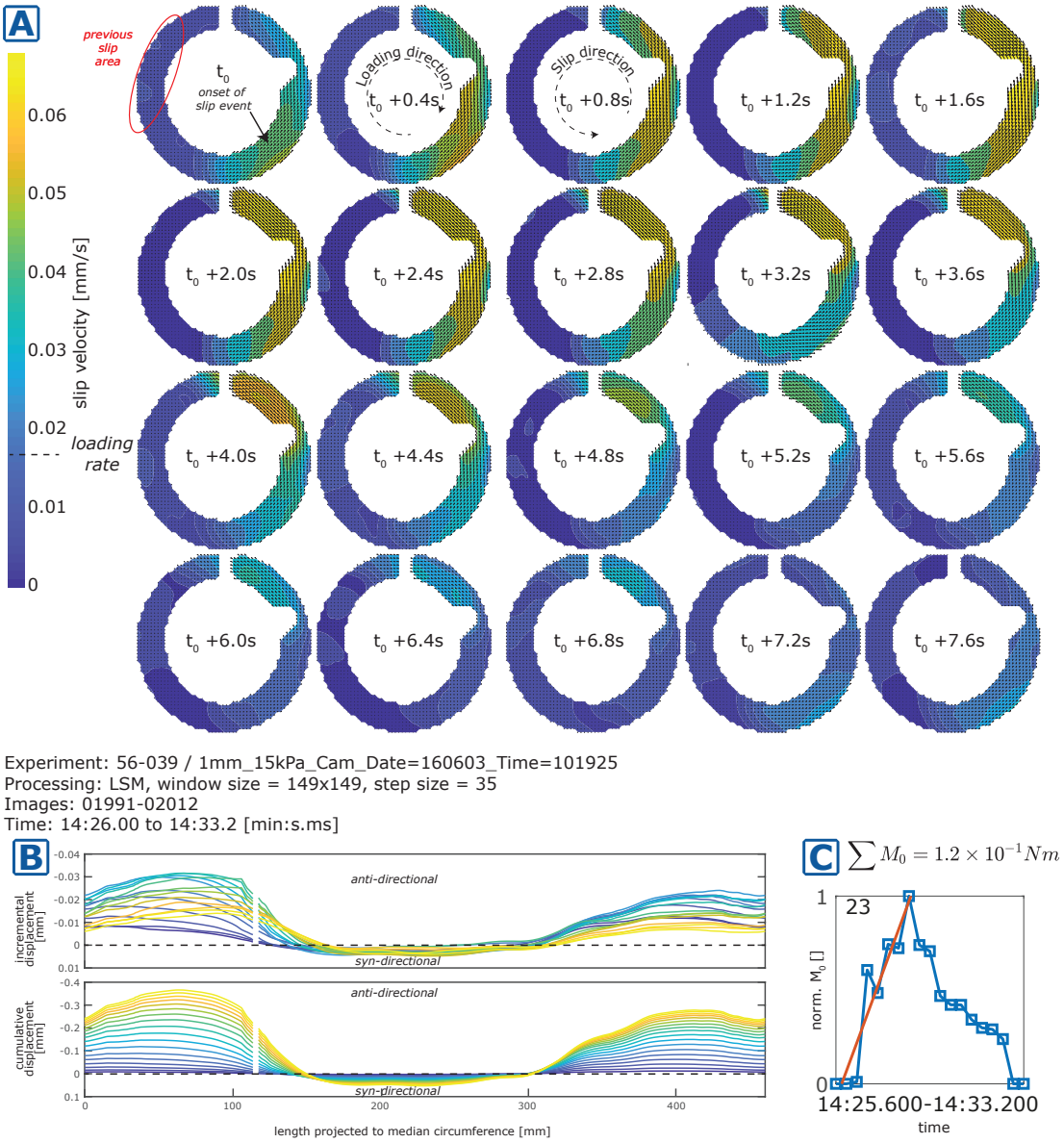

Figure 5.5: Compiled results from a bigger slip event that occurs after the event shown in Figure 5.4 (Num. 23 in Figure 5.11). (A) Slip distribution during the slip event. The direction of slip is counter clockwise. (B) Profiles of along-fault slip (incremental and cumulative) for each vector field. The colour indicates the time (blue = start, yellow = end). (C) Source time function showing the increase of seismic moment over the duration of the slip event. The y-axis shows the seismic moment normalized to the maximum seismic moment. The red line shows a linear fit of the rising segment.

5.1.3 Discussion

5.1.3.1 Analytical Solution of Slip in Cracks

The slip distribution along a selected profile is compared to the elastic model [Eshelby, 1957] and the critical fault tip taper (CFTT) Model [also termed 'small-scale yielding model', Kanninen and Popelar, 1985, Wang, 1995, Scholz and Lawler, 2004]. Displacement and profile length are normalized by the length of the profile (Figure 5.6). A third model that is important for the 'BOX'-Setup is the Dugdale-Barenblatt model, is also shown here for completeness.

Fault slip area during the early phase has a circular to elliptical shape [Scholz, 2002]. According to the elastic model, slip distribution Δu on a circular crack with radius r is approximated by:

$$\Delta u(x,y) = \frac{24}{7\pi}\, k\, \sqrt{r^2 - (x^2+y^2)} \tag{5.1}$$

where:

$k = \frac{\Delta\sigma}{G}$ is a scaling constant (ratio of stress drop $\Delta\sigma$ and shear modulus G)

x, y are the spatial coordinates.

For 1D slip along a profile line of length x normalized by the radius $r = \frac{x}{2}$ Equation 5.1 simplifies to:

$$\Delta u(x) = \frac{24}{7\pi}\, k\, \sqrt{1 - x^2)} \tag{5.2}$$

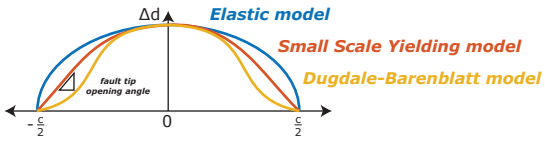

Figure 5.6: Comparison of the analytical solutions for crack growth in 1D [modified after Scholz, 2002]. On the y-axis the displacement Δd is shown and the x-axis shows the length of the profile c centred on the maximum displacement.

The elastic model has a stress singularity at the crack tip, because the results are complex for $r^2 < \sqrt{x^2+y^2}$. Furthermore, experimental studies show that close to the crack tip a tapering of the displacement can be observed [Scholz, 2002]. The CFTT model approximates the taper linearly and assumes a constant fault tip taper. The displacement magnitude still scales with the ratio of stress drop to shear modulus. An analytical expression does not exist for the CFTT model, therefore I use a linear fit to each side of the displacement profiles to compare the opening angle.

The fault slip does not follow the elastic model, although a faint similarity of the circular curve with the overall slip could be inferred (higher slip in central part, fast decay towards the edges). This is immediately visible by comparing the curve and the original data (Figure 5.7). But it is also reflected in the goodness of fit statistics which almost exclusively show $R^2 < 0.5$ and a very unstable solution of the curve fitting, which has a strong dependency on the starting point. For a few slip events I also tried to approximate the 2D slip distribution. In general, the shape of the slip event is reasonably close to an ellipse but can not be approximated with Equation 5.1 because the decay of slip towards the edges is too high.

In contrast to that, the CFTT model shows a good fit to the initial part of the slip profile, with $R^2 > 0.9$ in the majority of cases. From the slope m of the curve the opening angle is

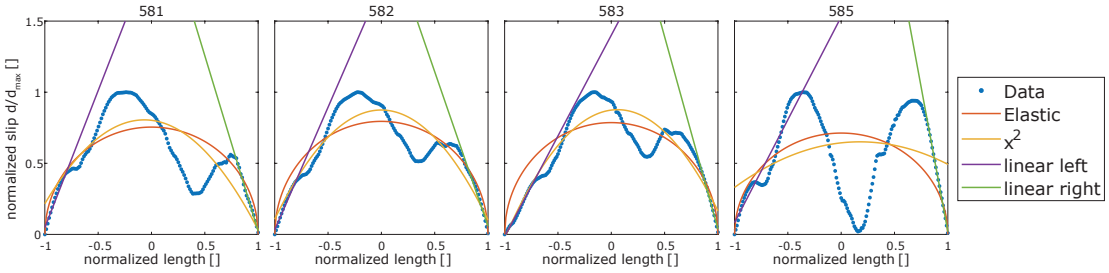

Figure 5.7: Incremental fault slip (1D) within the profile region for slip event #6 in 56-039-1, taken in the initial growth phase up to maximum moment release. Slip has been normalized to the maximum slip and the length by the total length of the slipping area. The lines show the fits of several models to the data set.

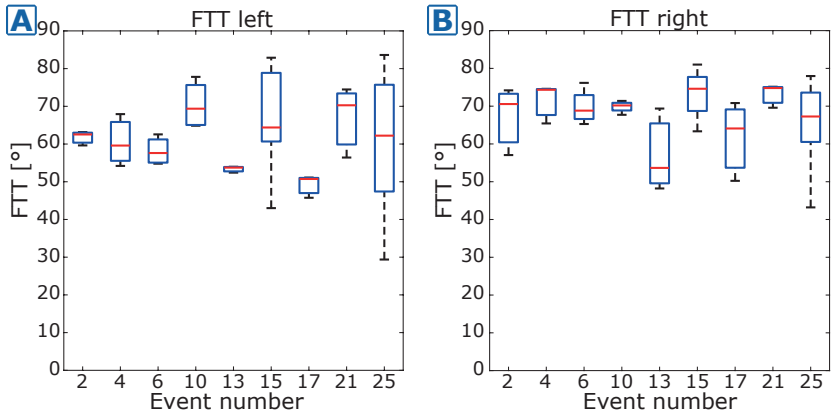

Figure 5.8: Comparison of different fault tip tapers from several slip events. Here only events are shown where the number of fits with $R^2 > 0.9$ is 3 and greater. This leaves out many small events with only a few points. (A) The left sided tapers show a much stronger variability and range from 30 to 85 degrees. (B) The right sided tapers are less heterogeneously distributed in between the events as well as for individual events.

calculated as:

$$\alpha = tan^{-1}m \tag{5.3}$$

The fault tip taper scales with the yield strength of the material directly in front of the tip. As a result, the opening angle should stay rather constant over one slip event. It also should be constant over several slip event if they rupture similar areas. The fault tip tapers for several experiments do not show significant difference (Figure 5.8), although some events have a large internal variability. The absolute angle is very high due to the normalization by the peak slip of the event.

The yield strength of glass beads is mainly determined by the recurrence time (see also Figure 3.5). If the time since the last rupture is high, the material has had a longer time to heal and therefore the strength is higher. This means, that the variability within one event can be explained by a rupture that is propagating into a region that has been ruptured previously with a shorter recurrence time than the rest of the patch. Late stage events (e.g. #25) rupture the complete fault area and are therefore good candidates for such behaviour. However, a significant trend in the variability of FTT within one event or between two events could not be verified with the amount of data available.

5.1.3.2 Seismic Moment and Source Time Functions

One parameter that allows a good comparison with seismic catalogues that are obtained from seismological studies, is the seismic moment. The seismic moment M_0 is the product of mean slip $\bar{d}$, slip area A, and shear modulus G in each image:

$$M_0 = \bar{d}AG \tag{5.4}$$

As an alternative, the seismic moment can also be calculated from the stress drop $\Delta\tau$ in relation to the slip area:

$$M_0 = \Delta\tau A^{\frac{3}{2}} \tag{5.5}$$

The needed parameters are taken from the stress measurements (RST) and the digital image correlation (PIV) (Table 5.1.3.2). All parameters can be directly determined for experiments where direct monitoring of slip area is possible. The slip area is defined as the area of active slip where the absolute slip velocity $|v|$ is higher than the loading rate v_L. The peaks in slip area are then correlated with stress drops measured by the ring shear tester (Figure 5.9).

Table 5.1: Parameters needed to calculate the seismic moment and their origin (digital image correlation: 'PIV', stress measurements: 'RST').

Parameter		Origin	Definition
active slip area	A	PIV, (RST)	Area of active slip where $\|v\| >= v_L$
mean slip	$\bar{d}$	PIV	Mean absolute displacement during a slip event in the active area
shear modulus	G	known	Shear modulus of the elastic block, in this case for gelatine equal to the Young's modulus $G = E \approx 150kPa$.
stress drop	$\Delta\tau$	RST	Stress drop of the event

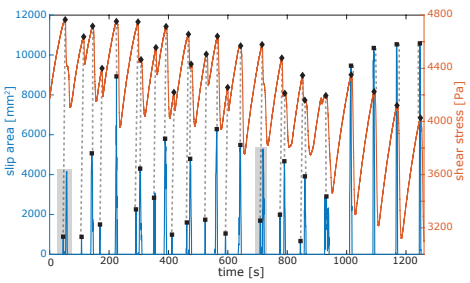

Figure 5.9: Correlation of slip area (blue) with shear stress (orange). Slip events (black markers) are detected in both curves and correlated with each other. In some cases a double peak is observable in the slip area which is not strongly expressed in the stress measurements (grey areas). In this case, the bigger slip area is used.

Figure 5.10 shows a comparison of the different ways to estimate the seismic moment for experiment 56-039. The estimates that use the area measured with PIV are very similar ('PIV+RST' and 'only PIV'). 'PIV+RST' incorporates stress drop and area with Equation 5.5, whereas 'only PIV' uses the slip area, mean slip and shear modulus to calculate the moment. The estimates using only the stress drop ('RST only') show a significantly higher moment rate. This is because the slip area is assumed to be the complete fault area, which is not necessarily correct. Even when the area is rescaled by the maximum stress drop, which means that a smaller stress drop has a smaller area, as $A^{\frac{3}{2}} \propto \Delta\tau$ they are much larger.

For a first order comparison the evolution of moment release during a slip event, called 'source time function', is evaluated. For the experiments shown in Figure 5.11, the estimation of the

complete moment release is done with Equation 5.5 which has proven to be reliable for estimating the moment release (Figure 5.10). The acquisition of images and stress measurements was not synchronized by an external clock for this experiment. As a result the estimated temporal difference between the two measurements is in the order of a few seconds. This makes it impossible to provide a combined calculation of the seismic moment with both measurements.

Most events show a linear increase in seismic moment in the initial phase up to the maximum moment. Afterwards, it decays non-linearly for very large events (e.g. 27 and 28) and almost linear for intermediate events (e.g. 15 and 20). This is in accordance with the findings of Meier et al. [2017] who also found a linear increase in seismic moment for earthquakes greater than M_w= 7.0. The non-linear decay for the setups presented here is differing from the natural observations, mostly because during the later stage the two ruptures link due to the annular shape of the setup and produce a much higher seismic moment.

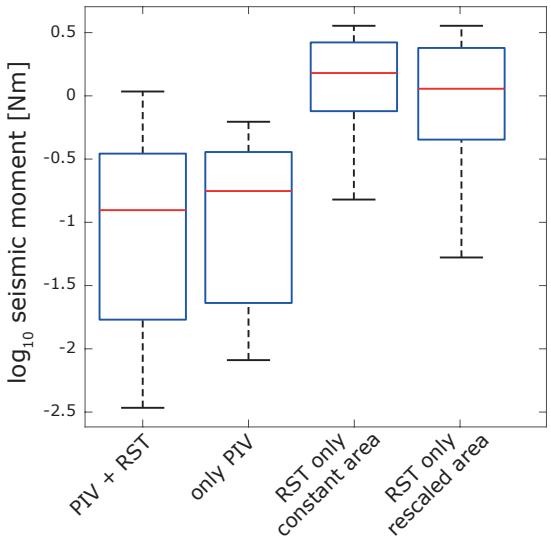

Figure 5.10: Comparison of different estimates of seismic moment. 'PIV+RST' combines both monitoring systems using Equation 5.5, whereas 'only PIV' uses the classical estimation (Equation 5.4) that is used for natural earthquakes, because stress drop is not measureable. The two estimates 'RST only', exclusively use the stress drop and the total area of the fault (Equation 5.5), and are significantly higher than the other estimates.

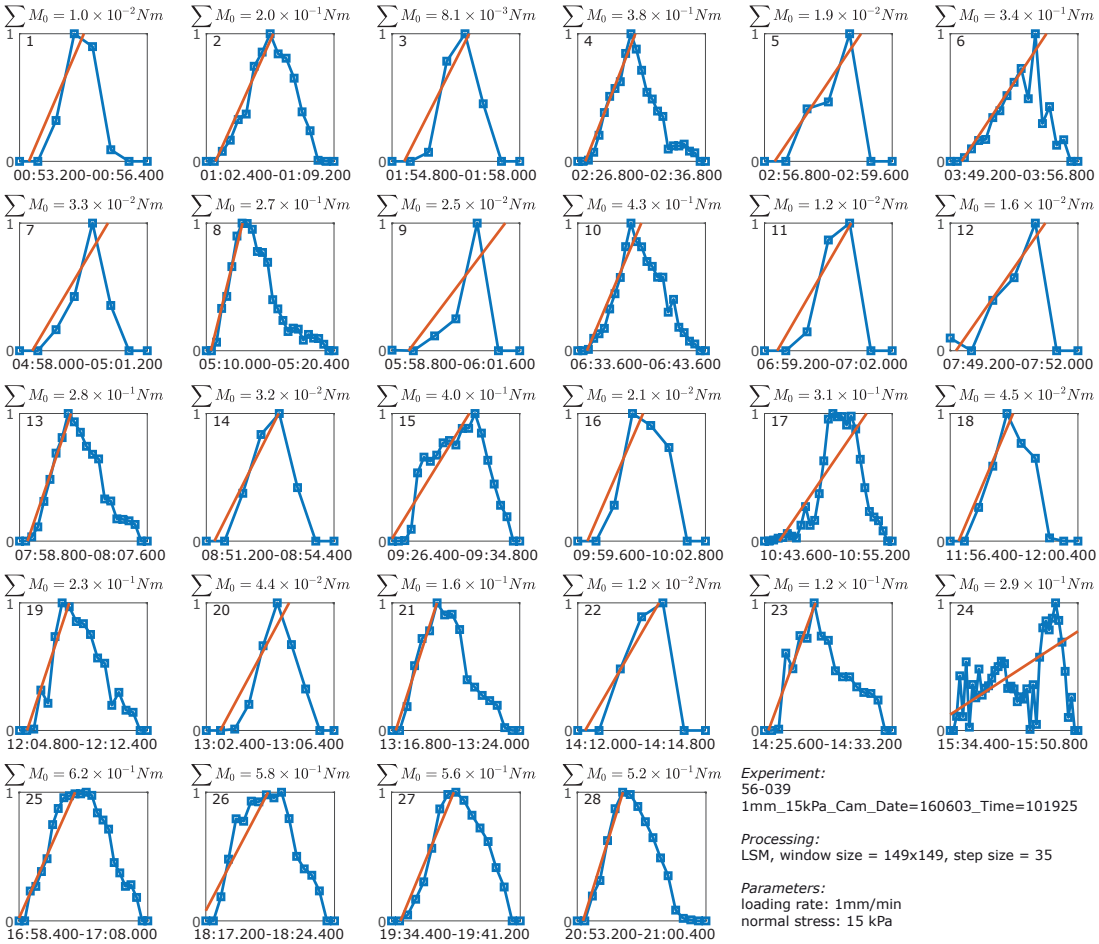

Figure 5.11: Evolution of seismic moment over the duration of one slip event for all detected events in experiment 56-039-1. Slip events with less than 5 data points have been ignored for this representation. Above each subfigure the cumulative moment release is given. For better comparison the y-axis is normalized to the maximum moment release rate in the individual event, and the x-axis is normalized by the event duration. The start and end time is given as 'min:s.ms' below each plot. The red line shows the result of a linear fit to the rising edge.

5.2 Strike-slip Configuration

In strike-slip configuration the surface displacement of the elastic blocks adjacent to the fault is observed, as opposed to the previous experiments where the fault surface has been monitored. The experimental setup is described in section 1.5.2 and features controlled velocity boundaries combined with force measurements. The first experiments have a single layer (only gelatine with glass beads). Later on a silicone layer is introduced to simulate the viscoelasticity of the lower crust.

5.2.1 Setup

The stress distribution in the block is mainly governed by the indenter and the angle of the fault zone. This mimics far-field loading conditions with the maximum horizontal stress S_{hmax} in the direction of the indenter. The minimum horizontal stress S_{hmin} is limited to the increasing 'lithostatic' pressure of the gelatine with increasing depth. The angle of the fault zone has to be in the range of the glass bead's angle of friction. The orientation of the fault therefore ranges between 15 and 28°, which corresponds to a friction coefficient of 0.3 to 0.55. If the angle of the zone is too small, the increase of normal stress on the fault is much larger than the shear stress and no slip failure can be initiated. A larger angle leads to stable sliding, because the system is not in the critical slip regime.

A major technical problem is the infiltration of sugar solution into the fault zone which prevents stick-slip. The lower boundary is sealed by the silicone oil that acts as a good sealant. The lateral edges of the blocks are the major pathways for water percolation. Therefore, only the inner 24 cm of the fault zone are moulded as a 0.5 cm wide fault. The cut and coated segments act as a sealant towards the outer edges and thus have to be very smooth. The blocks with the embedded fault zone are prepared on a metal sheet outside the tank and then plastic wrapped before being transferred into the box. The fault zone is prestressed to 5 - 10 N which stabilizes the plates and makes the removal of the plastic wrap easier.

The analogue fault is separated into aseismic (creeping) and seismic (stick-slipping) segments. The creeping patches lie at the outer edge of the fault and serve two purposes. Firstly, they isolate the granular material from the sugar solution that alters the characteristics of the glass beads. And secondly, the creeping segments help to produce continuous stressing of the central fault segment, without having major boundary effects, e.g. due to glass beads leaking out, or thickness changes.

5.2.2 Observables

5.2.2.1 Surface Displacement

The slip events nucleate around the transition of aseismic to seismic segments, because they pose a heterogeneity along the fault (Figure 5.12). The onset of slip can be traced to a very small region with elevated velocity which evolves into an elongated patch. The peak slip velocity itself is in the order of a few hundreds of micrometer per second ($\approx 600\mu$m/s), whereas the rupture travels the complete extend ($\approx$ 120mm) within 160ms. Therefore, the rupture velocity is several orders of magnitude bigger than the slip velocity ($\approx$1m/s vs. 10^{-4}m/s).

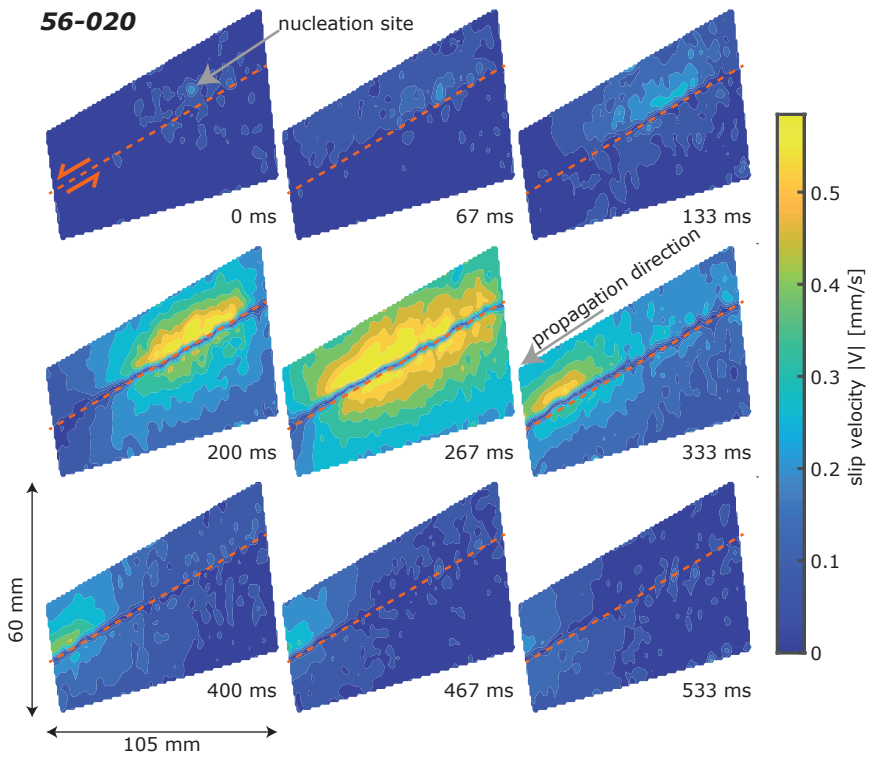

Figure 5.12: Displacement fields showing the evolution of absolute slip velocities over one slip event in the BOX-Setup. The red dashed line indicates the position of the fault. The overall shape of the vector field is non-rectangular because for this experiment, a smaller area of interest was chosen for digital image correlation. This was due to additional sensors embedded in the gelatine.

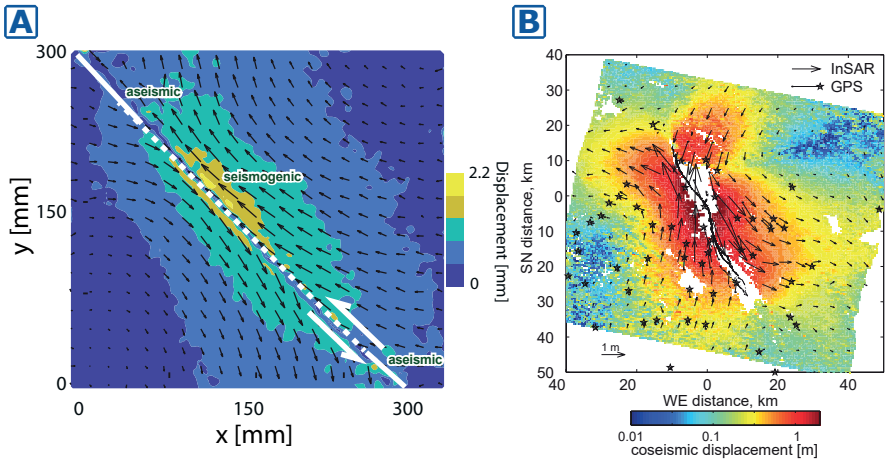

Figure 5.13: Coseismic displacement fields of (A) experimental slip event and (B) the 1991 Hector Mine earthquake [redrawn from Fialko et al., 2001].

5.2.3 Discussion

5.2.3.1 Comparison to Nature

As this model is fully scaled, the experimentally produced earthquakes can be scaled up to natural earthquakes using the scaling given in Section 1.4.1.

Surface Displacement The displacement field is qualitatively similar to typical coseismic displacements that have been found for earthquakes (5.13). Major similarities are the orientation of the displacement vectors which are parallel to the fault close to the fault and point towards or away from it at the edges. The absolute displacement shows an elliptical shape in the centre close to the fault and a 'butterfly' in the outer region which is not so well reproduced in Figure 5.13A but roughly visible at 200ms in Figure 5.12 and 5.17A. This observation is also in accordance with findings from similar analogue models [Caniven et al., 2015].

Statistical Parameters The model can be compared with the natural system by comparing the main statistical parameters that are available for earthquakes (Table 5.2.3.1). Because single fault statistics are rarely available, I use a regionally constrained model for the recurrence behaviour and more general statistics for all other parameters.

The recurrence time of slip events is 9.7 s with only minor variation. Scaling this using the static time scale yields a possible recurrence interval of a few hours to almost 2 years. This spread is due to the high uncertainty associated with the lower crustal viscosity, which influences the static time scale. To compare it with the natural value, one has to calculate the scaled moment magnitude of the analogue earthquakes, because the recurrence is strongly magnitude dependent. The seismic moment M_0 released during an event is around 0.15 Nm which gives an analogue moment magnitude of M_w =-6.6. This scales to $M_0 = 6.08 \cdot 10^{20}$to $6.29 \cdot 10^{21}$Nm and a resulting scaled moment magnitude of M_w =7.8 to 8.5. Using the Gutenberg-Richter law published in Schwartz and Coppersmith [1984] the recurrence interval for events of such magnitude is in the range of several thousands of years. As a result, the recurrence time of the analogue earthquakes is much lower than what is expected from events with such a high magnitude.

The average duration of a slip event is 2 s which scales to an earthquake duration of 13.8

to 20 minutes, which is one order of magnitude larger than the 0.01 to 2 minutes what are expected for the rupture duration of regular earthquakes [Ide et al., 2007]. Taken into account the large uncertainty associated with the scaling behaviour found by Ide et al. [2007] the analogue earthquakes plot within the upper range for regular earthquakes in the moment-duration plot (Figure 5.14). Therefore, the analogue earthquakes have similar moment release rates as regular earthquakes.

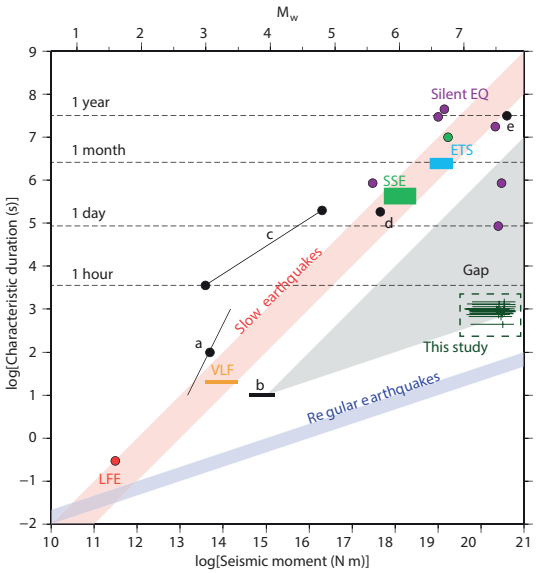

Figure 5.14: Scaled moment release and scaled duration with error bars (dark green), plotted into the moment-duration scaling plot by Ide et al. [2007]. The analogue earthquakes lie close to the upper limit of the scaling relation for regular earthquakes.

The total surface displacement over the duration of a slip event is in the order of 0.26 mm which scales to 57 to 95 m of surface displacement during a natural earthquake. This is one order of magnitude larger than usual estimates for coseismic surface displacement. The scaled stress drop is in the range of a few MPa, which corresponds to typical earthquake values of 0.1 to 10 MPa. In addition, the scaled slip velocity is in good accordance and lies within one order of magnitude from the natural observations.

5.2.3.2 Analytical Description of Surface Displacement

The surface displacement close to the fault is analysed for similarity with analytical solutions for fault slip. These solutions are frequently used to calculate the average slip on a fault from the surface displacement and have been successfully applied to analogue models [Caniven et al., 2015, and references therein]. Before the analysis, the background displacement is calculated from the surface displacement in the initial phase of the experiment, where no slip events have been detected (Figure 5.15). Because the angle of the fault is not optimally oriented for the coefficient of friction, primarily due to technical reasons, a large component of displacement is accommodated by elastic strain within the gelatine. This distorts the surface displacements by the slip events and increases the normal load on the fault surface. In addition, for some experiments the orientation of the fault with respect to the loading direction changes by several degrees due to the elastic deformation of gelatine.

Interseismic Phase The interseismic phase is characterised by none to very slow displacement along the locked segment of the fault. The creeping segments (left in Figure 5.16A) shows creep at the rate of the background far field loading velocity v_L. In a locked segment, the amount of

Table 5.2: Comparison of the scaled key parameters for analogue earthquakes obtained from experiment 56-012 and natural earthquakes. For the scaling factors see Table 1.2. The scaling factor for the seismic moment is calculated as $M_0^* = \sigma^* \cdot (L^*)^3$.

Parameter	Experimental value	Scaled value	Natural range	Source
recurrence time	9.70 ± 1.0 s	0.2 - 617 days	3800 - 15000 years	Gutenberg-Richter relation in Schwartz and Coppersmith [1984] for the southern segment of the San-Andreas Fault.
duration	2.00 ± 0.5 s	13.83 - 20.08 min	0.01 - 2 min	Moment-Duration scaling of regular earthquakes in Ide et al. [2007]
total surface displacement	0.26 ± 0.028 mm	56.93 - 94.60 m	5.5 - 6 m	Maximum surface displacement of the Hector-Mine M_w 7.1 earthquake [Fialko et al., 2001]
slip velocity	0.11 ± 0.015 mm/s	0.01 - 0.65 m/s	1 m/s	Value given in Rosenau and Oncken [2009]
stress drop	5.80 ± 0.8 Pa	2.32 - 5.23 MPa	0.1 - 10 MPa	General range of stress drops [Ruff, 1999]
seismic moment	0.150 ± 0.002 Nm	$6.08 \cdot 10^{20}$ - $6.29 \cdot 10^{21}$ Nm	10^{17} - 10^{28} Nm	General range of earthquakes
moment magnitude	-6.6	7.8 - 8.5	0.6 - 8.0	

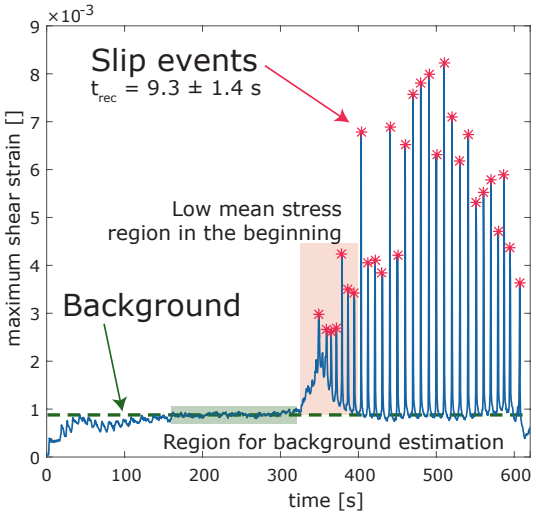

Figure 5.15: Maximum shear strain ϵ_{xy} over time in experiment 56-012. Slip events start to occur when the fault is under critical loading conditions. The green area shows the region where the background of elastic deformation (green dashed line) has been measured. The first slip events have a high interseimic creep, shown by the orange area.

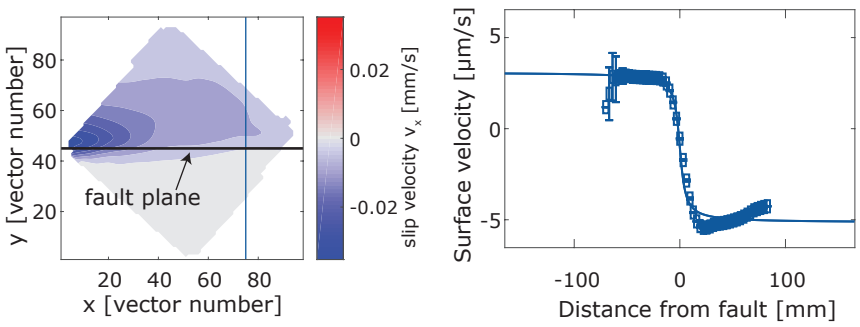

Figure 5.16: (A) Surface velocity in x-direction during one interseismic phase in experiment 56-012. The strong negative motion along the top segment indicates creep close to the far field loading conditions (v_L =0.05 mm/s). (B) Surface velocity along a profile across the fault. The fault is not completely locked and shows slow creep that is approximately one order of magnitude lower than v_L.

slip v_i decays with increasing fault perpendicular distance y according to the model proposed by Savage and Burford [1973]:

$$v_i(y) = \frac{v_L}{\pi} arctan(\frac{y}{D_L}) \tag{5.6}$$

From this model the locking depth D_L can be estimated from the surface displacement pattern. For the profile shown in Figure 5.16 the estimated locking depth is very shallow 3.9 ± 2.8mm and the estimated loading rate $v_L = -0.008 \pm 0.001$ mm/s. This very low estimate for the loading rate is probably due to the subtraction of the elastic far field loading pattern. The recurrence time of slip events is only a few seconds in this setup and therefore the interseismic period contains a strong postseismic component for most of the events. The slip event in shown in Figure 5.16 is one of the first interseismic phases in the experiment where the mean stress is still small. Later events are bigger and cause strong postseismic relaxation of the underlying viscoelastic silicone oil. As a result, Equation 5.6 does only fit very few events and no statistical analysis of the locking depth is possible.

Coseismic phase During the coseismic phase the slip velocity is one order of magnitude larger than during the interseimic period. Fault slip is left lateral for the shown experiment (Figure 5.17A) and the majority of slip is concentrated in two elliptical regions on each side of the fault. In the initial phase of the experiment the centroids of slip show an offset of several centimetres. In later events, at higher mean stresses, the centres lie on one line perpendicular to the fault.

The transition from negative to positive slip in the surface displacement is relatively smooth, compared to the analytical solution or other experiments. Firstly, this is due to the width of the brittle material embedded in the gelatine which is 5 mm. Other experiments and also natural fault zones have a much narrower width in comparison with the lateral extend of the fault. The effect is further amplified by the digital image correlation algorithm which uses a certain circular subset around the interrogation point (149 pixel in this case) and fills up the vectors that do not have a sufficiently high accuracy by cubic-spline interpolation.

For analysis of the perpendicular profiles the transition region has been left out, because the width of the experimental fault is much larger than what is assumed for most analytical models. The profiles are taken in x and y direction over the complete vector field at the centroid location for each slip peak (Figure 5.17A). The analytical solution for coseismic displacement

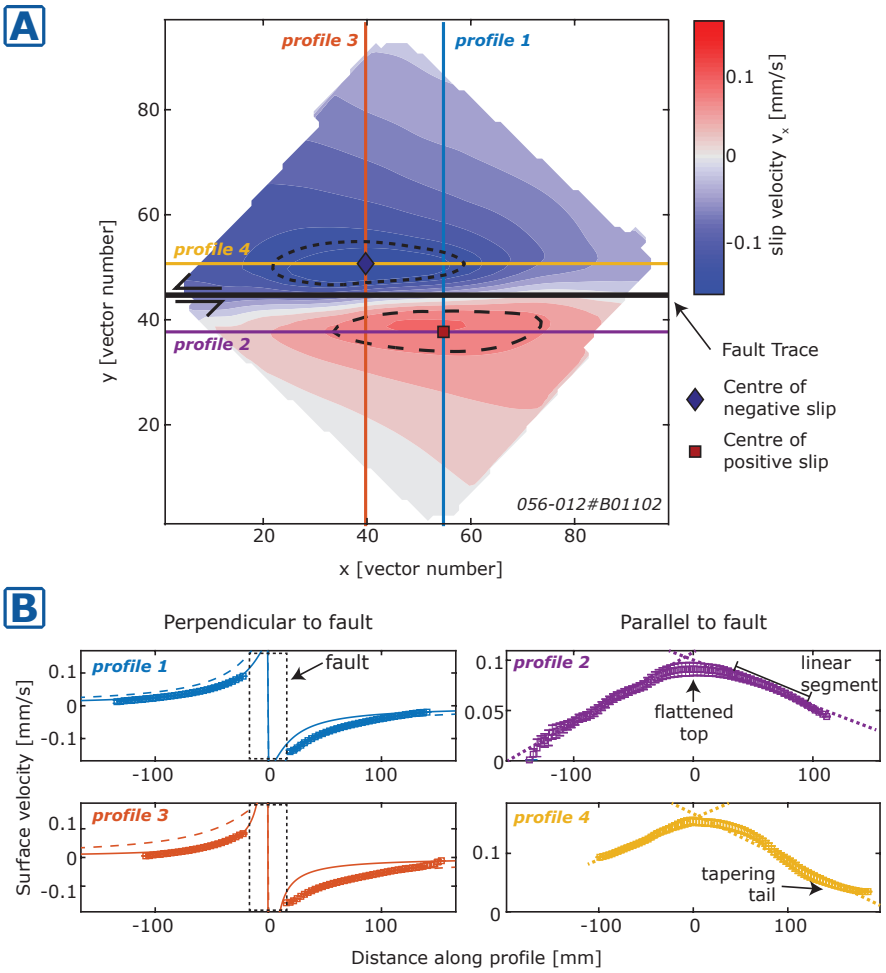

Figure 5.17: Coseismic surface displacement of one event in experiment 56-012 and several slip profiles taken at specific points. (A) Displacement field of the v_x-component and location of profiles. Negative slip (blue) indicates movement in negative x-direction (leftward) and positive slip indicates movement in positive x-direction. The slip centres (diamond and square) are slightly offset in the direction of movement. The dashed areas indicate the 95 percentile region of v_x. (B) v_x displacement along the profiles and fits of analytical solutions (Equation 5.7 and CFTT-Model).

after Okada [1985] is similar to the equation proposed by Savage and Burford [1973] (Equation 5.6) and approximates the coseismic slip v_c along a fault perpendicular profile y by:

$$v_c(y) = \frac{v_F}{\pi} arctan(\frac{D_d}{y}) \tag{5.7}$$

From this equation the on fault slip v_F and the depth of the elastic dislocation D_d can be estimated. Due to the asymmetry of the displacement fields on each side of the fault, each side is fit separately. The median dislocation depth is 29.9 mm with a relatively large scatter over the complete extend of the fault (Figure 5.18A). In general, most results are in accordance with the thickness of the elastic blocks which was 50 mm in this experiment. Only one fit indicates a higher dislocation depth, which can be neglected as statistical scatter. The fits indicate a coseismic displacement v_0 along the fault that is higher than -1 mm/s with a median of -0.497 mm/s. The negative polarity is due to the sinistral kinematics of the fault. This is higher than what is found as peak slip velocity for the surface displacement field (v_{max} = 0.2 mm/s) but still in the same order of magnitude. This may be due to the broad fault zone which leads to an 'extrapolation' of fault slip towards the fault core. Another possible explanation is that the slip at depth may be bigger than the measured surface displacement. The amount of outliers with $v_0 < -1$mm/s is higher than for the dislocation depth.

Profiles taken parallel to the strike of the fault are analysed with the analytical descriptions of crack growth (section 5.1.3.1, Equations 5.1 and 5.2). The profiles show that the maximum of fault slip occurs in the centre which is slightly flattened compared to the flanks of the profile (Figure 5.17B). The amount of slip decreases linearly towards the edges of the slip area. At the edges slip shows a concave, non-linear decay to the background level. This is in accordance with the Dugdale-Barenblatt model which is similar to the Elastic model (Equation 5.2) but does not have a stress singularity at the tip [Scholz, 2002] (Figure 5.6). Only few displacement profiles illustrate this behaviour because slip is truncated at the edges of the plates.

The elastic model does not fit the fault parallel displacement profiles because of the strong linear decay towards the edges. As a consequence the profiles are only fit by a linear function and the opening angle is determined. Figure 5.18C shows a comparison of all fault opening angles where $R^2 > 0.95$. The slopes show a larger scatter with a log-log distribution, although most opening angles lie within one order of magnitude. The large scatter is probably due to the non-linear taper towards the edge of some profiles which decreases the measured opening angle.

Postseismic phase The experiments that include an additional layer of silicone oil at the bottom of the gelatine show hints of post-event, viscoelastic relaxation (Figure 5.19). If the system would show only elastic and rate-and-state-behaviour, the force drop after an event would be followed by an immediate linear increase during the interseismic period. Furthermore, the fault would immediately lock again and no slip rates should be measureable. In contrast to that, the experiments with a viscoelastic bottom layer show a non linear decrease in force after a slip event, as well as elevated slip.

Two models can be used to describe the non-linear decay. From earthquake statistics, the number of aftershocks after an earthquake decays according to a power-law [Omori, 1894]. If one assumes that the aftershocks represent the seismic afterslip on a fault, the total afterslip (including seismic and aseismic afterslip) should scale according to the same power-law. Here I use the Omori-Utsu model where the aftershock frequency, or slip rate in this case, scales with

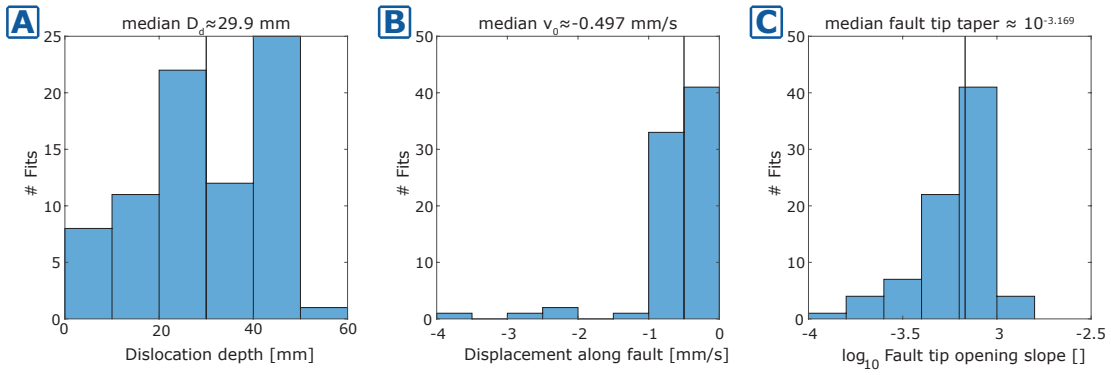

Figure 5.18: Fit parameters for the analytical solution of the slip profiles for all events in experiment 56-012. Only fits with $R^2 > 0.95$ are shown. (A) Dislocation depth during coseismic slip. The maximum depth of the fault is 50 mm, which is also reflected by the fits. (B) On fault displacement in the direction parallel to the fault. The results are higher than what would be expected from the peak surface displacement. (C) Fault tip taper (opening angle) given here as the slope of the linear fit. The values show a scatter over 2 orders of magnitude with a median of $10^{-3.169}$.

the reciprocal of time after the main shock, or peak slip rate [Utsu, 1961]:

$$n(t) = \frac{k}{(c+t)^p} \tag{5.8}$$

Where k, c, and p are constants. For typical earthquakes the constant p lies between 0.7 and 1.5. This law is purely descriptive and does not have any physical mechanism. Applying Equation 5.8 to the slip rate, contains the assumption that the slip rate is proportional to the moment release rate in the postseismic phase.

Several other statistical laws describing the aftershocks are available. One is Båth's law, that indicates the difference between the mainshock magnitude and the largest aftershock. Furthermore, aftershock sequences often follow a Gutenberg-Richter law, which indicates that there is a higher amount of small aftershocks compared to large aftershocks. The combination of the three above observations, together with the detection threshold for smaller events, leads to a moment release rate which scales in a similar way to the Omori-Law [Kagan and Houston, 2005]. Additionally, I assume that the proportion of seismic to aseismic slip stays constant over the afterslip phase because the available laws only use seismic events and neglect potential aseismic slip on the fault. Therefore, it is reasonable to assume that the afterslip in the experiment should show the characterisics indicated by the Omori-Law.

In contrast, the viscoelastic relaxation of a Maxwell material, e.g. the silicone oil below the gelatine layer, shows an exponential decay of stress with a characteristic timescale $\lambda_M = \frac{\eta}{E}$ where η is the viscous component and E is the elastic component [Mezger, 2006]. This description is based on physical parameters of the material. In terms of strain rate $\dot{\epsilon}$ this decay is given as:

$$\dot{\epsilon}(t) = \dot{\epsilon}_0 \exp^{(-\frac{E}{\eta}t)} \tag{5.9}$$

where $\dot{\epsilon}_0$ is the initial strain rate at the peak of slip.

A comparison between the two laws shows that the Omori-Utsu aftershock model shows a better quantitative fit to the experimental data ($R^2 = 0.99$) in comparison with the Maxwell model ($R^2 = 0.96$). But both models give reasonable results for the fit. The power-law exponent

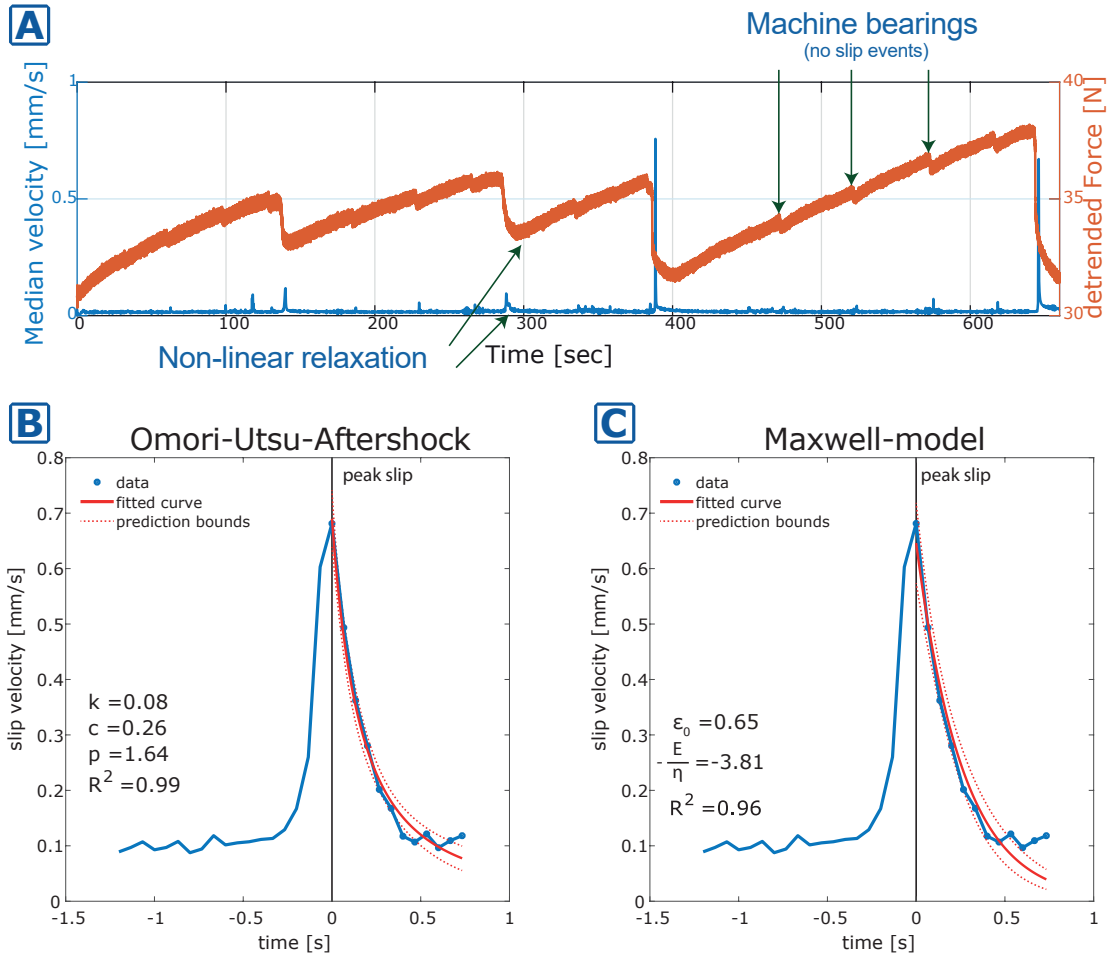

Figure 5.19: (A): Mean slip velocity and force during experiment 56-020. The force is detrended by subtracting a long term moving average. This subtracts the continuous increase of force over the experimental duration because the fault was not optimally oriented. (B) Fit of the Omori-Utsu aftershock model to the experimentally determined slip velocity (Equation 5.8) [Omori, 1894, Utsu, 1961]. (C) Fit of a simple Maxwell relaxation model to the decay of slip velocity (Equation 5.9).

of the Omori-Utsu fit is $p = 1.64$ which is slightly above the upper limit of what is observed for natural earthquakes. Furthermore, the Maxwell relaxation time resulting from the fit is $\lambda_M = 0.26 \pm 0.11s$ which is similar within errors to the observed Maxwell relaxation time of the silicone oil of 0.18 s (Table 2.4). It is very likely that the non-linear decay of the slip rate is granular afterslip within the fault zone mainly driven by the viscoelastic relaxation of the silicone layer.

5.3 Boundary Effects and Problems with the Current Setup

Both setups show a behaviour that is similar to the natural prototype although some individual parameters, such as coseismic displacement, are not scalable to the prototype. This may be the result of geometrical constraints of the setup. The presented experiments use blocks with an edge length of around 30 cm which scales to 65-110 km in nature and are therefore much smaller than what is needed for a large-scale lithospheric fault of several 100 km length. Furthermore, boundary effects perturb the stress field on the seismogenic patch due to the small distance between the aseismic patch and edge of the blocks. Further experiments with bigger blocks and with adjustable differential stress (biaxial) will decrease the boundary effects from the setup geometry.

The width to length ratio of the fault zone is currently not true to scale because a minimum amount of glass beads is required to build up force chains and a granular fault zone [Daniels and Hayman, 2008, Cates et al., 1998]. Increasing the setup size is going to reduce this effect. A decrease of the glass bead size leads to the loss of the stick-slip characteristics in the granular fault zone, probably because the adhesive, electrostatic forces between the grains are higher with respect to the repulsive forces.

Reproducibility of the system behaviour is an important factor for this experimental study. Subtle changes in stiffness, or frictional behaviour of the glass beads, due to humidity and cross-contamination with dust particles, can alter the stick-slip properties of the system. To counteract this, several steps are used. The glass-beads have to be sieved to a narrow grain size range of 300-355 μm and stored within a drying furnace prior to shearing which reduces the humidity related adhesion between individual glass beads. The gelatine shows a highly temperature dependent rheology and is therefore also equilibrated with the laboratory temperature for several hours. This ensures very similar surface conditions and gelatine stiffness. This sensitivity of the system to external factors may also be indicative of being close to the instability criterion for the creep to stick-slip transition. In many cases the stick-slip process can be initiated by changing the velocity several times which approaches the bifurcation from a different direction and leads to unstable behaviour [Heslot et al., 1994]. To improve the reproducibility even further, the switch from gelatine to silicone rubber as elastic analogue material can get rid of the strong temperature dependency of gelatine.

Chapter 6

Conclusions

This study shows the feasibility of the presented analogue setups to be used as models for earthquake recurrence along large lithospheric fault zones. The materials that are used in the setups are suitable analogues for their prototypical equivalents. The quantitative and qualitative results of the experimental runs show that the characteristics of the models well represent the natural prototype.

A detailed assessment of the rheological properties of silicone oils that are currently used in analogue modelling revealed that although chemically equivalent silicone oils show a difference in their viscosity, they are not significant enough to justify major differences in model outcomes (Chapter 2). In addition, the variability of the silicone oils from different laboratories is several orders of magnitude less than the uncertainty of viscosity estimates of the natural prototype (lower crust and mantle). Major differences in the experiments may only arise when the temperature is changed from experiment to experiment. Furthermore, silicone oils are very stable over long periods of time and, once equilibrated with laboratory conditions, relatively insensitive to short term changes in the laboratory.

The (Multi-)Maxwell rheology of the tested silicone oils is similar to the behaviour of rocks around the brittle-ductile transition. This makes them suitable for use in seismotectonic analogue models that aim at modelling all the relevant stages of the seismic cycle. At low deformation rates the system shows Newtonian rheology which changes to a power-law rheology ($n = 2 - -3$) at higher deformation rates, similar to the decrease in effective viscosity during postseismic relaxation. This result is incorporated into the experimental setup presented in Section 1.5.2.

The stick-slip dynamics of glass beads showed that analogue fault gouge reproduce typical characteristics that have been observed in rock mechanical tests (Chapter 3). The rate-and-state parameters for glass beads are similar to natural fault zones that show velocity weakening behaviour. The slip events are quasiperiodic and show some precursory activity for experiments with a high stiffness of the apparatus. The precursors only occur in a small timeframe that lies between 50 and 90% of the overall seismic cycle. Although the stiffness of the analogue setup designed in the second part of this thesis 5 is too low to show the precursory activity, they still represent a characteristic behaviour of the granular material that is used in the setup. In a later stage the model could potentially have a higher stiffness, where the precursory activity is important.

A dynamic triggering algorithm has been developed to adaptively change the frame rate of the camera system (Chapter 4). When a slip event has been detected the camera switches to

high-speed acquisition and goes back to low-speed during the interseimic period. The time scale of the observed processes during one experimental run spans several orders of magnitude (μm/s to m/s). As a result the amount of data produced with a continuous camera system is too much to be handled efficiently. The triggering algorithm saves large amounts of data (>90%) in most cases. Although the system is rather simple, this is a major technical advance in the design of analogue models.

The results of the analogue models show good similarity with the natural prototype (Chapter 5). The rupture propagation within the fault zone starts at a small nucleation point, then continues radially, and finally propagates along the fault zone when the outer boundary is reached. The estimation of source parameters, such as seismic moment, proved to be reliable and comparable to previous results for the purely granular stick-slip experiments. Furthermore, the slip events cluster in certain regions of the model and sometimes only rupture a small area of the fault. This may make the RST setup suitable to model the long-term statistical behaviour of a single fault, which also may not always rupture to its complete extend. A comparison of the displacement field with analytical models of cracks remained ambiguous. From the generally accepted descriptions, only the critical fault tip taper model showed a good similarity with the displacement during a slip event.

The geometrically and rheologically most similar analogue model (BOX) shows a good qualitative similarity. The surface displacement is similar to natural earthquakes, and the rupture propagation is several orders of magnitude higher than the slip velocity. The slip events themselves are a bit slower (< 1mm/s) than what is expected from the scaling. The viscoelastic layering produces a non-linear post-seismic relaxation pattern which is detectable in shear force and slip velocity.

Chapter 7

Outlook

The conclusions illustrate that the developed setup reliably shows the characteristics of seismic cycle under the assumption that they are governed by rate-and-state-dependent friction in combination with elastic and viscoelastic components. The presented setup is going to serve as an experimental benchmark to a numerical code that is developed within the overarching framework of this project. Therefore, a detailed parameter study with both setups, in close interaction with the numerical simulation, has to be performed. This is going to provide a better insight into the predictability of slip over multiple seismic cycles, as well as help to validate the experimental methodology.

Another direction can be the incorporation of multiple faults to simulate the interaction between them. Because the single fault system already shows a strong complexity in time and space this should happen after the validity of the experimental approach has been verified by numerical simulations.

As a first step towards better control on the boundary conditions and the material properties several changes to the experimental setup could be made. For long term experiments and continuous material properties the gelatine has to be exchanged for another more stable material. A prime candidate is silicone rubber which is as stable as silicone oil and shows nice elastic properties (Section 1.4.2.1). Additionally, the open side walls can be exchanged with force controlled sidewalls, to have a much better control on the differential stress within the sample. Currently, this is only roughly given by the orientation of the fault to the compression direction. Adding a second set of movable back walls, could enable larger samples and a better comparison with numerical simulations and rock mechanical tests.

Bibliography

B Aagaard, C Williams, and M Knepley. Pylith: A finite-element code for modeling quasi-static and dynamic crustal deformation. *Eos Trans. AGU*, 88:52, 2007.

H Ahlenius. tectonicplates - world tectonic plates and boundaries. *Online:https://github.com/fraxen/tectonicplates*, 2014. URL `https://github.com/fraxen/tectonicplates`.

Keiiti Aki. Maximum likelihood estimate of b in the formula log n= a-bm and its confidence limits. *Bull. Earthq. Res. Inst., Tokyo Univ.*, 43:237–239, 1965.

Keiiti Aki. Scaling law of seismic spectrum. *Journal of Geophysical Research*, 72(4):1217–1231, 1967.

R.M. Allen. *Earthquake Hazard Mitigation: New Directions and Opportunities*, volume 4, pages 607–647. 12 2007.

Jennifer L Anthony and Chris Marone. Influence of particle characteristics on granular friction. *Journal of Geophysical Research: Solid Earth*, 110(B8), 2005. doi: 10.1029/2004jb003399.

Jean-Philippe Avouac. From geodetic imaging of seismic and aseismic fault slip to dynamic modeling of the seismic cycle. *Annual Review of Earth and Planetary Sciences*, 43(1):233–271, 2015. doi: 10.1146/annurev-earth-060614-105302. URL `https://doi.org/10.1146/annurev-earth-060614-105302`.

Raik Bachmann, Onno Oncken, Johannes Glodny, Wolfgang Seifert, Viktoria Georgieva, and Masafumi Sudo. Exposed plate interface in the european alps reveals fabric styles and gradients related to an ancient seismogenic coupling zone. *Journal of Geophysical Research: Solid Earth*, 114(B5), 2009.

NM Beeler, SH Hickman, and T-f Wong. Earthquake stress drop and laboratory-inferred interseismic strength recovery. *Journal of Geophysical Research: Solid Earth*, 106(B12):30701–30713, 2001. doi: 10.1029/2000jb900242.

NM Beeler, T-F Wong, and SH Hickman. On the expected relationships among apparent stress, static stress drop, effective shear fracture energy, and efficiency. *Bulletin of the Seismological Society of America*, 93(3):1381–1389, 2003.

NM Beeler, Terry Tullis, Jenni Junger, Brian Kilgore, and David Goldsby. Laboratory constraints on models of earthquake recurrence. *Journal of Geophysical Research: Solid Earth*, 2014. doi: 10.1002/2014jb011184.

Yehuda Ben-Zion. Collective behavior of earthquakes and faults: Continuum-discrete transitions, progressive evolutionary changes, and different dynamic regimes. *Reviews of Geophysics*, 46 (4), 2008. doi: 10.1029/2008rg000260.

Yehuda Ben-Zion, Mariana Eneva, and Yunfeng Liu. Large earthquake cycles and intermittent criticality on heterogeneous faults due to evolving stress and seismicity. *Journal of Geophysical Research: Solid Earth*, 108(B6), 2003. doi: 10.1029/2002jb002121.

Dapeng Bi, Jie Zhang, Bulbul Chakraborty, and Robert P Behringer. Jamming by shear. *Nature*, 480(7377):355–358, 2011. doi: 10.1038/nature10667.

SL Bilek and T Lay. Tsunami earthquakes possibly widespread manifestations of frictional conditional stability. *Geophysical Research Letters*, 29(14), 2002. doi: 10.1029/2002gl015215.

Roger Bilham. Urban earthquake fatalities: A safer world, or worse to come? *Seismological Research Letters*, 75(6):706, 2004. doi: 10.1785/gssrl.75.6.706. URL `+http://dx.doi.org/10.1785/gssrl.75.6.706`.

Peter Bird. An updated digital model of plate boundaries. *Geochemistry, Geophysics, Geosystems*, 4(3), 2003.

David Boutelier, Christoph Schrank, and Alexander Cruden. Power-law viscous materials for analogue experiments: New data on the rheology of highly-filled silicone polymers. *Journal of Structural Geology*, 30(3):341–353, 2008. doi: 10.1016/j.jsg.2007.10.009.

Jean-Pierre Brun. Deformation of the continental lithosphere: Insights from brittle-ductile models. *Geological Society, London, Special Publications*, 200(1):355–370, 2002. doi: 10.1144/GSL.SP.2001.200.01.20.

James N Brune. Earthquake modeling by stick-slip along precut surfaces in stressed foam rubber. *Bulletin of the Seismological society of America*, 63(6-1):2105–2119, 1973.

Edgar Buckingham. On physically similar systems; illustrations of the use of dimensional equations. *Physical Review*, 4(4):345, 1914. doi: 10.1103/physrev.4.345.

Charles G Bufe, Philip W Harsh, and Robert O Burford. Steady-state seismic slip–a precise recurrence model. *Geophysical Research Letters*, 4(2):91–94, 1977. doi: 10.1029/gl004i002p00091.

Andrew P. Bunger, Robert G. Jeffrey, and Emmanuel Detournay. Application of scaling laws to laboratory-scale hydraulic fractures, January 2005.

Roland Bürgmann. The geophysics, geology and mechanics of slow fault slip. *Earth and Planetary Science Letters*, 495:112–134, 2018.

Roland Bürgmann and Georg Dresen. Rheology of the lower crust and upper mantle: evidence from rock mechanics, geodesy, and field observations. *Annual Review of Earth and Planetary Sciences*, 36(1):531, 2008. doi: 10.1146/annurev.earth.36.031207.124326.

E Burov. Rheology and strength of the lithosphere. *Marine and Petroleum Geology*, 28:1402 – 1443, 2011. doi: doi:10.1016/j.marpetgeo.2011.05.008.

J. Byerlee. Friction of rocks. *pure and applied geophysics*, 116(4):615–626, Jul 1978. ISSN 1420-9136. doi: 10.1007/BF00876528. URL `https://doi.org/10.1007/BF00876528`.

Daniel E Byrne, Dan M Davis, and Lynn R Sykes. Loci and maximum size of thrust earthquakes and the mechanics of the shallow region of subduction zones. *Tectonics*, 7(4):833–857, 1988. doi: 10.1029/tc007i004p00833.

Y Caniven, S Dominguez, R Soliva, R Cattin, M Peyret, M Marchandon, C Romano, and V Strak. A new multilayered visco-elasto-plastic experimental model to study strike-slip fault seismic cycle. *Tectonics*, 2015. doi: 10.1002/2014tc003701.

F. Caruso, A. Pluchino, V. Latora, S. Vinciguerra, and A. Rapisarda. Analysis of self-organized criticality in the olami-feder-christensen model and in real earthquakes. *Phys. Rev. E*, 75: 055101, May 2007. doi: 10.1103/PhysRevE.75.055101. URL `https://link.aps.org/doi/10.1103/PhysRevE.75.055101`.

ME Cates, JP Wittmer, J-P Bouchaud, and Ph Claudin. Jamming, force chains, and fragile matter. *Physical review letters*, 81(9):1841, 1998. doi: 10.1103/physrevlett.81.1841.

C. G. B. Cole. *Gelatin*, pages 1183 – 1188. John Wiley & Wiley & Sons, N. Yo, 2 edition, 2000.

F Corbi, F Funiciello, C Faccenna, G Ranalli, and A Heuret. Seismic variability of subduction thrust faults: Insights from laboratory models. *Journal of Geophysical Research*, 116(B6), jun 2011. doi: 10.1029/2010jb007993.

F Corbi, F Funiciello, M Moroni, Y Dinther, PM Mai, LA Dalguer, and C Faccenna. The seismic cycle at subduction thrusts: 1. insights from laboratory models. *Journal of Geophysical Research: Solid Earth*, 118(4):1483–1501, 2013. doi: 10.1029/2012jb009481.

Fabio Corbi, Eleonora Rivalta, Virginie Pinel, Francesco Maccaferri, and Valerio Acocella. Understanding the link between circumferential dikes and eruptive fissures around calderas based on numerical and analog models. *Geophysical Research Letters*, 43(12):6212–6219, 2016.

WP Cox and EH Merz. Correlation of dynamic and steady flow viscosities. *Journal of Polymer Science*, 28(118):619–622, 1958. doi: 10.1002/pol.1958.1202811812.

Rod Cross. Elastic and viscous properties of silly putty. *American Journal of Physics*, 80(10): 870–875, 2012. doi: 10.1119/1.4732086.

Deshan Cui, Wei Wu, Wei Xiang, Thiep Doanh, Qiong Chen, Shun Wang, Qingbing Liu, and Jinge Wang. Stick-slip behaviours of dry glass beads in triaxial compression. *Granular Matter*, 19(1):1, 2017.

Karen E. Daniels and Nicholas W. Hayman. Force chains in seismogenic faults visualized with photoelastic granular shear experiments. *J. Geophys. Res.*, 113(B11), nov 2008. doi: 10.1029/2008jb005781. URL `http://dx.doi.org/10.1029/2008JB005781`.

P. Davy, R. Le Goc, C. Darcel, O. Bour, de Dreuzy J. R., and R. Munier. A likely universal model of fracture scaling and its consequence for crustal hydromechanics. *J. Geophys. Res.*, 115(B10), June 2010. ISSN 0148-0227. doi: 10.1029/2009jb007043. URL `https://doi.org/10.1029/2009JB007043`.

Ph Davy and PR Cobbold. Experiments on shortening of a 4-layer model of the continental lithosphere. *Tectonophysics*, 188(1):1–25, 1991. doi: 10.1016/0040-1951(91)90311-f.

Ciro Del Negro, Gilda Currenti, and Danila Scandura. Temperature-dependent viscoelastic modeling of ground deformation: application to etna volcano during the 1993–1997 inflation period. *Physics of the Earth and Planetary Interiors*, 172(3):299–309, 2009. doi: 10.1016/j.pepi.2008.10.019.

D. V. Denisov, K. A. Lörincz, J. T. Uhl, K. A. Dahmen, and P. Schall. Universality of slip avalanches in flowing granular matter. *Nature Communications*, 7:10641, February 2016. URL `http://dx.doi.org/10.1038/ncomms10641`.

Marine A Denolle and Peter M Shearer. New perspectives on self-similarity for shallow thrust earthquakes. *Journal of Geophysical Research: Solid Earth*, 121(9):6533–6565, 2016.

E Di Giuseppe, F Funiciello, F Corbi, G Ranalli, and G Mojoli. Gelatins as rock analogs: A systematic study of their rheological and physical properties. *Tectonophysics*, 473(3):391–403, 2009. doi: 10.1016/j.tecto.2009.03.012.

E Di Giuseppe, F Corbi, F Funiciello, A Massmeyer, TN Santimano, M Rosenau, and A Davaille. Characterization of carbopol® hydrogel rheology for experimental tectonics and geodynamics. *Tectonophysics*, 642:29–45, 2015. doi: 10.1016/j.tecto.2014.12.005.

Erika Di Giuseppe, Anne Davaille, Eric Mittelstaedt, and Marc François. Rheological and mechanical properties of silica colloids: from newtonian liquid to brittle behaviour. *Rheologica acta*, 51(5):451–465, 2012. doi: 10.1007/s00397-011-0611-9.

Giulio Di Toro, Raehee Han, Takehiro Hirose, Nicola De Paola, Stefan Nielsen, Kazuo Mizoguchi, Fabio Ferri, Massimo Cocco, and Tosihiko Shimamoto. Fault lubrication during earthquakes. *Nature*, 471(7339):494–498, 2011. doi: 10.1038/nature09838.

Dieterich. Time-dependent friction and the mechanics of stick-slip. *Pageoph*, 116, 1978.

James H Dieterich. Modeling of rock friction: 1. experimental results and constitutive equations. *Journal of Geophysical Research: Solid Earth*, 84(B5):2161–2168, 1979a. doi: 10.1029/jb084ib05p02161.

James H Dieterich. Modeling of rock friction: 2. simulation of preseismic slip. *Journal of Geophysical Research: Solid Earth*, 84(B5):2169–2175, 1979b. doi: 10.1029/jb084ib05p02169.

James H Dieterich and Brian D Kilgore. Direct observation of frictional contacts: New insights for state-dependent properties. *Pure and Applied Geophysics*, 143(1-3):283–302, 1994.

James H Dieterich and Brian D Kilgore. Imaging surface contacts: power law contact distributions and contact stresses in quartz, calcite, glass and acrylic plastic. *Tectonophysics*, 256(1):219–239, 1996. doi: 10.1016/0040-1951(95)00165-4.

JH Dieterich. Applications of rate-and state-dependent friction to models of fault slip and earthquake occurrence. *Treatise on Geophysics*, 4:107–129, 2007. doi: 10.1016/b978-044452748-6.00065-1.

Y. Dinther, T. V. Gerya, L. A. Dalguer, P. M. Mai, G. Morra, and D. Giardini. The seismic cycle at subduction thrusts: Insights from seismo-thermo-mechanical models. *Journal of Geophysical Research: Solid Earth*, 118(12):6183–6202, 2013. doi: 10.1002/2013JB010380. URL `https://agupubs.onlinelibrary.wiley.com/doi/abs/10.1002/2013JB010380`.

Tim P Dooley and Guido Schreurs. Analogue modelling of intraplate strike-slip tectonics: A review and new experimental results. *Tectonophysics*, 574:1–71, 2012.

Donna Eberhart-Phillips, Peter J. Haeussler, Jeffrey T. Freymueller, Arthur D. Frankel, Charles M. Rubin, Patricia Craw, Natalia A. Ratchkovski, Greg Anderson, Gary A. Carver, Anthony J. Crone, Timothy E. Dawson, Hilary Fletcher, Roger Hansen, Edwin L. Harp, Ruth A. Harris, David P. Hill, Sigrún Hreinsdóttir, Randall W. Jibson, Lucile M. Jones, Robert Kayen, David K. Keefer, Christopher F. Larsen, Seth C. Moran, Stephen F. Personius, George Plafker, Brian Sherrod, Kerry Sieh, Nicholas Sitar, and Wesley K. Wallace. The 2002 denali fault earthquake, alaska: A large magnitude, slip-partitioned event. *Science*, 300(5622):1113–1118, 2003. ISSN 0036-8075. doi: 10.1126/science.1082703. URL `http://science.sciencemag.org/content/300/5622/1113`.

David T Eddington, John P Puccinelli, and David J Beebe. Thermal aging and reduced hydrophobic recovery of polydimethylsiloxane. *Sensors and Actuators B: Chemical*, 114(1): 170–172, 2006.

Eric R Engdahl and Antonio Villaseñor. Global seismicity: 1900–1999. In *International Geophysics*, volume 81, pages 665–cp2. Elsevier, 2002.

John D Eshelby. The determination of the elastic field of an ellipsoidal inclusion, and related problems. In *Proceedings of the Royal Society of London A: Mathematical, Physical and Engineering Sciences*, volume 241, pages 376–396. The Royal Society, 1957.

B Ferdowsi, M Griffa, RA Guyer, PA Johnson, C Marone, and J Carmeliet. Microslips as precursors of large slip events in the stick-slip dynamics of sheared granular layers: A discrete element model analysis. *Geophysical Research Letters*, 40(16):4194–4198, 2013. doi: 10.1002/grl.50813.

Yuri Fialko, Mark Simons, and Duncan Agnew. The complete (3-d) surface displacement field in the epicentral area of the 1999 mw7. 1 hector mine earthquake, california, from space geodetic observations. *Geophysical Research Letters*, 28(16):3063–3066, 2001. doi: 10.1029/2001gl013174.

Edward H. Field, Ramon J. Arrowsmith, Glenn P. Biasi, Peter Bird, Timothy E. Dawson, Karen R. Felzer, David D. Jackson, Kaj M. Johnson, Thomas H. Jordan, Christopher Madden, Andrew J. Michael, Kevin R. Milner, Morgan T. Page, Tom Parsons, Peter M. Powers, Bruce E. Shaw, Wayne R. Thatcher, Ray J. Weldon, II, and Yuehua Zeng. Uniform california earthquake rupture forecast, version 3 (ucerf3)—the time-independent model. *Bulletin of the Seismological Society of America*, 104(3):1122, 2014. doi: 10.1785/0120130164. URL `+http://dx.doi.org/10.1785/0120130164`.

David Fleet and Yair Weiss. Optical flow estimation. In *Handbook of mathematical models in computer vision*, pages 237–257. Springer, 2006.

Andrew M. Freed, Roland Bürgmann, Eric Calais, and Jeff Freymueller. Stress-dependent power-law flow in the upper mantle following the 2002 denali, alaska, earthquake. *Earth and Planetary Science Letters*, 252(34):481 – 489, 2006. ISSN 0012-821X. doi: http://dx.doi.org/10.1016/j.epsl.2006.10.011. URL `http://www.sciencedirect.com/science/article/pii/S0012821X06007321`.

THW Goebel, TW Becker, CG Sammis, G Dresen, and D Schorlemmer. Off-fault damage and acoustic emission distributions during the evolution of structurally complex faults over series of stick-slip events. *Geophysical Journal International*, 197(3):1705–1718, 2014.

Christopher Goetze and Brian Evans. Stress and temperature in the bending lithosphere as constrained by experimental rock mechanics. *Geophysical Journal International*, 59(3):463–478, 1979. doi: 10.1111/j.1365-246X.1979.tb02567.x. URL `http://dx.doi.org/10.1111/j.1365-246X.1979.tb02567.x`.

J Gomberg. Cascadia onshore-offshore site-response, submarine sediment mobilization, and earthquake recurrence. *Journal of Geophysical Research: Solid Earth*, 2018.

J Gomberg, A Wech, Kenneth Creager, K Obara, and Duncan Agnew. Reconsidering earthquake scaling. *Geophysical Research Letters*, 43(12):6243–6251, 2016. doi: 10.1002/2016gl069967.

Armin Gruen. Adaptive least squares correlation: a powerful image matching technique. *South African Journal of Photogrammetry, Remote Sensing and Cartography*, 14(3):175–187, 1985.

Sebastian Hainzl. Self-organization of earthquake swarms. *Journal of Geodynamics*, 35(1):157 – 172, 2003. ISSN 0264-3707. doi: https://doi.org/10.1016/S0264-3707(02)00060-1. URL `http://www.sciencedirect.com/science/article/pii/S0264370702000601`.

M. R. Handy, G. Hirth, and R. Bürgmann. Continental fault structure and rheology from the frictional-to-viscous transition downward. *Tectonic Faults: Agents of Change on a Dynamic Earth*, pages 139–81, 2007.

Ruth A Harris. Large earthquakes and creeping faults. *Reviews of Geophysics*, 55(1):169–198, 2017.

A. Heinecke, A. Breuer, S. Rettenberger, M. Bader, A. A. Gabriel, C. Pelties, A. Bode, W. Barth, X. K. Liao, K. Vaidyanathan, M. Smelyanskiy, and P. Dubey. Petascale high order dynamic rupture earthquake simulations on heterogeneous supercomputers. In *SC14: International Conference for High Performance Computing, Networking, Storage and Analysis*, pages 3–14, Nov 2014. doi: 10.1109/SC.2014.6.

F Heslot, T Baumberger, B Perrin, B Caroli, and C Caroli. Creep, stick-slip, and dry-friction dynamics: Experiments and a heuristic model. *Physical review E*, 49(6):4973, 1994. doi: 10.1103/physreve.49.4973.

M King Hubbert. Theory of scale models as applied to the study of geologic structures. *Geological Society of America Bulletin*, 48(10):1459–1520, 1937.

D. Hyndman and D. Hyndman. *Natural Hazards and Disasters*. Cengage Learning, 2016. ISBN 9781305888180. URL `https://books.google.de/books?id=nMgaCgAAQBAJ`.

RD Hyndman and Kelin Wang. Thermal constraints on the zone of major thrust earthquake failure: The cascadia subduction zone. *Journal of Geophysical Research: Solid Earth*, 98(B2): 2039–2060, 1993.

Satoshi Ide, Gregory C Beroza, David R Shelly, and Takahiko Uchide. A scaling law for slow earthquakes. *Nature*, 447(7140):76, 2007. doi: 10.1038/nature05780.

Yao Jiang, Gonghui Wang, Toshitaka Kamai, and Mauri J McSaveney. Effect of particle size and shear speed on frictional instability in sheared granular materials during large shear displacement. *Engineering Geology*, 210:93–102, 2016. doi: 10.1016/j.enggeo.2016.06.005.

Yan Y Kagan and Heidi Houston. Relation between mainshock rupture process and omori's law for aftershock moment release rate. *Geophysical Journal International*, 163(3):1039–1048, 2005.

Hiroo Kanamori. Quantification of earthquakes. *Nature*, 271(5644):411, 1978.

Melvin F Kanninen and Carl L Popelar. Advanced fracture mechanics. 1985. doi: 10.1115/1.3225862.

Aitaro Kato, Kazushige Obara, Toshihiro Igarashi, Hiroshi Tsuruoka, Shigeki Nakagawa, and Naoshi Hirata. Propagation of slow slip leading up to the 2011 mw 9.0 tohoku-oki earthquake. *Science*, 335(6069):705–708, 2012. ISSN 0036-8075. doi: 10.1126/science.1215141. URL `http://science.sciencemag.org/content/335/6069/705`.

Stephen H. Kirby. Rock mechanics observations pertinent to the rheology of the continental lithosphere and the localization of strain along shear zones. *Tectonophysics*, 119(1):1 – 27, 1985. ISSN 0040-1951. doi: https://doi.org/10.1016/0040-1951(85)90030-7. URL `http://www.sciencedirect.com/science/article/pii/0040195185900307`. Collision Tectonics: Deformation of Continental Lithosphere.

Matthias Klinkmüller, Guido Schreurs, Matthias Rosenau, and Helga Kemnitz. Properties of granular analogue model materials: A community wide survey. *Tectonophysics*, 684:23–38, 2016.

B. P. Kneubuehl. *Allgemeine Wundballistik*, pages 91–170. Springer Berlin Heidelberg, Berlin, Heidelberg, 2008. ISBN 978-3-540-79009-9. doi: 10.1007/978-3-540-79009-9_3. URL `https://doi.org/10.1007/978-3-540-79009-9_3`.

DL Kohlstedt, Brian Evans, SJ Mackwell, et al. Strength of the lithosphere: constraints imposed by laboratory experiments. *JOURNAL OF GEOPHYSICAL RESEARCH-ALL SERIES-*, 100:17–587, 1995.

LaVisionGmbH. Strainmaster. *Product Manual*, 2017.

JR Leeman, DM Saffer, MM Scuderi, and C Marone. Laboratory observations of slow earthquakes and the spectrum of tectonic fault slip modes. *Nature communications*, 7, 2016.

MF Linker and JH Dieterich. Effects of variable normal stress on rock friction: Observations and constitutive equations. *Journal of Geophysical Research: Solid Earth*, 97(B4):4923–4940, 1992.

David A Lockner and Paul G Okubo. Measurements of frictional heating in granite. *Journal of Geophysical Research: Solid Earth*, 88(B5):4313–4320, 1983.

Jo Lohrmann, Nina Kukowski, Jürgen Adam, and Onno Oncken. The impact of analogue material properties on the geometry, kinematics, and dynamics of convergent sand wedges. *Journal of Structural Geology*, 25(10):1691–1711, 2003.

Karen Mair, Kevin M Frye, and Chris Marone. Influence of grain characteristics on the friction of granular shear zones. *Journal of Geophysical Research: Solid Earth*, 107(B10), 2002. doi: 10.1029/2001jb000516.

James E Mark, Harry R Allcock, and Robert West. *Inorganic polymers*. Oxford University Press, 2005.

Dimitrije Marković and Claudius Gros. Power laws and self-organized criticality in theory and nature. *Physics Reports*, 536(2):41–74, 2014.

C Marone, K Mair, and KM Frye. The effect of particle dimensionality on granular friction: Comparison of laboratory and numerical approaches. In *AGU Fall Meeting Abstracts*, volume 1, page 03, 2002.

Chris Marone. Laboratory-derived friction laws and their application to seismic faulting. *Annual Review of Earth and Planetary Sciences*, 26(1):643–696, 1998. doi: 10.1146/annurev.earth.26.1.643.

Chris Marone and CH Scholz. The depth of seismic faulting and the upper transition from stable to unstable slip regimes. *Geophysical Research Letters*, 15(6):621–624, 1988. doi: 10.1029/gl015i006p00621.

Robert S Maxwell, Bryan Balazs, Rebecca Cohenour, and Elizabeth Prevedel. Aging of silica-filled pdms/pdps copolymers in desiccating environments: a dsc and nmr study. In *Macromolecular Symposia*, volume 202, pages 291–296. Wiley Online Library, 2003.

KR McClay, T Dooley, and G Lewis. Analog modeling of progradational delta systems. *Geology*, 26(9):771–774, 1998.

M-A Meier, JP Ampuero, and Thomas H Heaton. The hidden simplicity of subduction megathrust earthquakes. *Science*, 357(6357):1277–1281, 2017.

T.G. Mezger. *The Rheology Handbook: For Users of Rotational and Oscillatory Rheometers*. Coatings Compendien. Vincentz Network, 2006. ISBN 9783878701743. URL `http://books.google.de/books?id=N9Fdn0MEIDIC`.

M Moreno, Daniel Melnick, M Rosenau, John Bolte, Jan Klotz, H Echtler, J Baez, K Bataille, J Chen, M Bevis, et al. Heterogeneous plate locking in the south–central chile subduction zone: Building up the next great earthquake. *Earth and Planetary Science Letters*, 305(3-4):413–424, 2011.

Marcos Moreno, Matthias Rosenau, and Onno Oncken. 2010 maule earthquake slip correlates with pre-seismic locking of andean subduction zone. *Nature*, 467(7312):198, 2010.

S Nasuno, A Kudrolli, and Jerry P Gollub. Friction in granular layers: Hysteresis and precursors. *Physical Review Letters*, 79(5):949, 1997. doi: 10.1103/physrevlett.79.949.

S Nasuno, A Kudrolli, A Bak, and Jerry P Gollub. Time-resolved studies of stick-slip friction in sheared granular layers. *Physical Review E*, 58(2):2161, 1998. doi: 10.1103/physreve.58.2161.

BI Nelson and JM Dealy. Dynamic mechanical analysis using complex waveforms. In *Techniques in Rheological Measurement*, pages 197–224. Springer, 1993.

Kazushige Obara and Aitaro Kato. Connecting slow earthquakes to huge earthquakes. *Science*, 353(6296):253–257, 2016. doi: 10.1126/science.aaf1512.

Obermeier. Korasilon ® fluids of the m-type. *Online:*, April 2014. URL `http://www.obermeier.de/en/products/silicones/`.

Yoshimitsu Okada. Surface deformation due to shear and tensile faults in a half-space. *Bulletin of the seismological society of America*, 75(4):1135–1154, 1985.

F. Omori. On the after-shocks of earthquakes. *The University*, 1894.

Marion Panien, Guido Schreurs, and Adrian Pfiffner. Mechanical behaviour of granular materials used in analogue modelling: insights from grain characterisation, ring-shear tests and analogue experiments. *Journal of Structural Geology*, 28(9):1710–1724, 2006.

Belle Philibosian, Kerry Sieh, Jean-Philippe Avouac, Danny H. Natawidjaja, Hong-Wei Chiang, Chung-Che Wu, Hugo Perfettini, Chuan-Chou Shen, Mudrik R. Daryono, and Bambang W. Suwargadi. Rupture and variable coupling behavior of the mentawai segment of the sunda megathrust during the supercycle culmination of 1797 to 1833. *Journal of Geophysical Research: Solid Earth*, 119(9):7258–7287, 2014. doi: 10.1002/2014JB011200. URL `https://agupubs.onlinelibrary.wiley.com/doi/abs/10.1002/2014JB011200`.

Linette Prawirodirdjo, Robert McCaffrey, C. David Chadwell, Yehuda Bock, and Cecep Subarya. Geodetic observations of an earthquake cycle at the sumatra subduction zone: Role of interseismic strain segmentation. *Journal of Geophysical Research: Solid Earth*, 115(B3), 2010. doi: 10.1029/2008JB006139. URL `https://agupubs.onlinelibrary.wiley.com/doi/abs/10.1029/2008JB006139`.

Ernest Rabinowicz. The nature of the static and kinetic coefficients of friction. *Journal of applied physics*, 22(11):1373–1379, 1951.

Ernest Rabinowicz. Stick and slip. *Scientific American*, 194(5):109–119, 1956.

Friction Rabinowicz. Wear of materials, j, 1965.

HF Reid. The mechanism of the earthquake. the california earthquake of april 18, 1906: Rep. of the state investigation commiss. vol. 2. p. 1. 1910.

James R Rice. Constitutive relations for fault slip and earthquake instabilities. *Pure and applied geophysics*, 121(3):443–475, 1983. doi: 10.1007/978-3-0348-6608-8_7.

Malte C. Ritter, Karen Leever, Matthias Rosenau, and Onno Oncken. Scaling the sand box - mechanical (dis-) similarities of granular materials and brittle rock. *J. Geophys. Res. Solid Earth*, 2016a. doi: 10.1002/2016jb012915. URL `http://dx.doi.org/10.1002/2016JB012915`.

Malte Christian Ritter, Karen Leever, Matthias Rosenau, and Onno Oncken. Supplement to: Scaling the sand box - mechanical (dis-) similarities of granular materials and brittle rock. *GFZ Data Services*, 2016b. doi: 10.5880/GFZ.4.1.2016.005. URL `http://doi.org/10.5880/GFZ.4.1.2016.005`.

AJ Rosakis, O Samudrala, and D Coker. Cracks faster than the shear wave speed. *Science*, 284 (5418):1337–1340, 1999. doi: 10.1126/science.284.5418.1337.

Matthias Rosenau and Onno Oncken. Fore-arc deformation controls frequency-size distribution of megathrust earthquakes in subduction zones. *Journal of Geophysical Research: Solid Earth (1978–2012)*, 114(B10), 2009. doi: 10.1029/2009jb006359.

Matthias Rosenau, Jo Lohrmann, and Onno Oncken. Shocks in a box: An analogue model of subduction earthquake cycles with application to seismotectonic forearc evolution. *Journal of Geophysical Research: Solid Earth (1978–2012)*, 114(B1), 2009. doi: 10.1029/2008jb005665.

Matthias Rosenau, Fabio Corbi, and Stephane Dominguez. Analogue earthquakes and seismic cycles: experimental modelling across timescales. *Solid Earth*, 8(3):597, 2017. doi: 10.5194/se-8-597-2017.

M Rudolf, D Boutelier, M Rosenau, G Schreurs, and O Oncken. Supplement to: Rheological benchmark of silicone oils used for analog modeling of short-and long-termlithospheric deformation. *Services, GFZ Data*, 2016a.

M. Rudolf, M. Rosenau, and O. Oncken. Supplement to: Interseismic deformation transients and precursory phenomena: Insights from spring-slider experiments with a granular fault zone. *GFZ Data Services*, unpublished.

Michael Rudolf, David Boutelier, Matthias Rosenau, Guido Schreurs, and Onno Oncken. Rheological benchmark of silicone oils used for analog modeling of short-and long-term lithospheric deformation. *Tectonophysics*, 2016b. doi: 10.1016/j.tecto.2015.11.028.

Larry J Ruff. Dynamic stress drop of recent earthquakes: variations within subduction zones. In *Seismogenic and Tsunamigenic Processes in Shallow Subduction Zones*, pages 409–431. Springer, 1999.

Andy Ruina. Slip instability and state variable friction laws. *Journal of Geophysical Research: Solid Earth*, 88(B12):10359–10370, 1983. doi: 10.1029/jb088ib12p10359.

Andy L Ruina. *Friction laws and instabilities: A quasistatic analysis of some dry frictional behavior*. PhD thesis, Brown University, 1981.

John B. Rundle, Donald L. Turcotte, Robert Shcherbakov, William Klein, and Charles Sammis. Statistical physics approach to understanding the multiscale dynamics of earthquake fault systems. *Reviews of Geophysics*, 41(4), 2003. doi: 10.1029/2003RG000135. URL `https://agupubs.onlinelibrary.wiley.com/doi/abs/10.1029/2003RG000135`.

JC Savage and RO Burford. Geodetic determination of relative plate motion in central california. *Journal of Geophysical Research*, 78(5):832–845, 1973.

CH Scholz and Anupma Gupta. Fault interactions and seismic hazard. *Journal of Geodynamics*, 29(3):459–467, 2000. doi: 10.1016/s0264-3707(99)00040-x.

Christopher H Scholz. Earthquakes and friction laws. *Nature*, 391(6662):37–42, 1998. doi: 10.1038/34097.

Christopher H Scholz. *The mechanics of earthquakes and faulting*. Cambridge university press, 2002.

Christopher H Scholz. Large earthquake triggering, clustering, and the synchronization of faults. *Bulletin of the Seismological Society of America*, 100(3):901–909, 2010. doi: 10.1785/0120090309.

Christopher H Scholz and Theresa M Lawler. Slip tapers at the tips of faults and earthquake ruptures. *Geophysical research letters*, 31(21), 2004.

Alexandre Schubnel, Stefan Nielsen, Jacopo Taddeucci, Sergio Vinciguerra, and Sandro Rao. Photo-acoustic study of subshear and supershear ruptures in the laboratory. *Earth and Planetary Science Letters*, 308(3):424–432, 2011.

D Schulze. Development and application of a novel ring shear tester. *Aufbereitungs Technik*, 35 (10):524–535, 1994.

Dietmar Schulze. Time-and velocity-dependent properties of powders effecting slip-stick oscillations. *Chemical engineering & technology*, 26(10):1047–1051, 2003.

Bernd Schurr, Günter Asch, Sebastian Hainzl, Jonathan Bedford, Andreas Hoechner, Mauro Palo, Rongjiang Wang, Marcos Moreno, Mitja Bartsch, Yong Zhang, et al. Gradual unlocking of plate boundary controlled initiation of the 2014 iquique earthquake. *Nature*, 512(7514): 299–302, 2014. doi: 10.1038/nature13681.

David P Schwartz and Kevin J Coppersmith. Fault behavior and characteristic earthquakes: Examples from the wasatch and san andreas fault zones. *Journal of Geophysical Research: Solid Earth*, 89(B7):5681–5698, 1984.

Susan Y Schwartz and Juliana M Rokosky. Slow slip events and seismic tremor at circum-pacific subduction zones. *Reviews of Geophysics*, 45(3), 2007.

MM Scuderi, Cristiano Collettini, C Viti, Elisa Tinti, and C Marone. Evolution of shear fabric in granular fault gouge from stable sliding to stick slip and implications for fault slip mode. *Geology*, 45(8):731–734, 2017.

Kunihiko Shimazaki and Takashi Nakata. Time-predictable recurrence model for large earthquakes. *Geophysical Research Letters*, 7(4):279–282, 1980.

A Sornette and D Sornette. Self-organized criticality and earthquakes. *EPL (Europhysics Letters)*, 9(3):197, 1989.

D. Sornette, P. Davy, and A. Sornette. Structuration of the lithosphere in plate tectonics as a self-organized critical phenomenon. *Journal of Geophysical Research: Solid Earth*, 95(B11):17353–17361, 1990. doi: 10.1029/JB095iB11p17353. URL `https://agupubs.onlinelibrary.wiley.com/doi/abs/10.1029/JB095iB11p17353`.

William Spence, Stuart A Sipkin, and George L Choy. Measuring the size of an earthquake. *Earthquake Information Bulletin (USGS)*, 21(1):58–63, 1989.

Arsia Takeh and Sachin Shanbhag. A computer program to extract the continuous and discrete relaxation spectra from dynamic viscoelastic measurements. *Appl. Rheol*, 23(2):95–104, 2013.

M. Saskia Ten Grotenhuis, Sandra Piazolo, Tadeusz Pakula, Cees W Passchier, and Paul D Bons. Are polymers suitable rock analogs? *Tectonophysics*, 350(1):35–47, 2002.

Simon T. Tse, Renata Dmowska, and James R. Rice. Stressing of locked patches along a creeping fault. *Bulletin of the Seismological Society of America*, 75(3):709, 1985. URL `+http://dx.doi.org/`.

Terry E Tullis and John D Weeks. Constitutive behavior and stability of frictional sliding of granite. In *Friction and faulting*, pages 383–414. Springer, 1986. doi: 10.1007/978-3-0348-6601-9_2.

Jonathan T. Uhl, Shivesh Pathak, Danijel Schorlemmer, Xin Liu, Ryan Swindeman, Braden A. W. Brinkman, Michael LeBlanc, Georgios Tsekenis, Nir Friedman, Robert Behringer, Dmitry Denisov, Peter Schall, Xiaojun Gu, Wendelin J. Wright, Todd Hufnagel, Andrew Jennings, Julia R. Greer, P. K. Liaw, Thorsten Becker, Georg Dresen, and Karin A. Dahmen. Universal quake statistics: From compressed nanocrystals to earthquakes. *Scientific Reports*, 5:16493, November 2015. URL `http://dx.doi.org/10.1038/srep16493`.

U.S. Geological Survey and California Geological Survey. Quaternary fault and fold database for the united states. *Online:*, 2006. URL `https://earthquake.usgs.gov/hazards/qfaults/map/#qfaults`.

T. Utsu. A statistical study of the occurrence of aftershocks. *Geophysical Magazine*, 30:521–605, 1961.

W. Wang. Shear strength and fatigue crack propagation in concrete by energy method. *PhD-Dissertation*, 1995.

R. Weijermars. Finite strain of laminar flows can be visualized in sgm36-polymer. *Naturwissenschaften*, 73(1):33–34, 1986a. ISSN 0028-1042. doi: 10.1007/BF01168803. URL `http://dx.doi.org/10.1007/BF01168803`.

R Weijermars, MPA t Jackson, and B Vendeville. Rheological and tectonic modeling of salt provinces. *Tectonophysics*, 217(1-2):143–174, 1993.

Ruud Weijermars. Flow behaviour and physical chemistry of bouncing putties and related polymers in view of tectonic laboratory applications. *Tectonophysics*, 124(3):325–358, 1986b.

Ruud Weijermars and Harro Schmeling. Scaling of newtonian and non-newtonian fluid dynamics without inertia for quantitative modelling of rock flow due to gravity (including the concept of rheological similarity). *Physics of the Earth and Planetary Interiors*, 43(4):316 – 330, 1986. ISSN 0031-9201. doi: http://dx.doi.org/10.1016/0031-9201(86)90021-X. URL `http://www.sciencedirect.com/science/article/pii/003192018690021X`.

Steven G Wesnousky. Seismological and structural evolution of strike-slip faults. *Nature*, 335 (6188):340, 1988.

Jonathan E Wu, Ken McClay, Paul Whitehouse, and Tim Dooley. 4d analogue modelling of transtensional pull-apart basins. *Marine and Petroleum Geology*, 26(8):1608–1623, 2009.

Kewei Xiang, Guangsu Huang, Jing Zheng, Xiaoan Wang, Guang xian Li, and Jingyun Huang. Accelerated thermal ageing studies of polydimethylsiloxane (pdms) rubber. *Journal of Polymer Research*, 19(5):1–7, 2012.

Gui-Qing Zhang, Lin Wang, and Tian-Lun Chen. Analysis of self-organized criticality in weighted coupled systems. *Physica A: Statistical Mechanics and its Applications*, 388(7):1249 – 1256, 2009. ISSN 0378-4371. doi: https://doi.org/10.1016/j.physa.2008.12.043. URL `http://www.sciencedirect.com/science/article/pii/S0378437108010753`.

Appendix A

Data Analysis

This chapter briefly summarizes the data analysis that has been performed on the experimental data. Furthermore, the analysis for all published results is described in the respective chapters, or in the related data publications.

A.1 Rheological measurements

The analysis for the rheological description of the silicone oils is described in chapter 2 [Rudolf et al., 2016b] and the raw data is published in Rudolf et al. [2016a].

A.2 Detection of Slip Events with the Ring-Shear-Tester

This section describes the measurement procedure and data analysis that was done with the data from chapter 3.

The data has been acquired with a PCI-BUS card in combination with an A/D-converted (MAD12) using Nextview NT by BMC-Messsysteme. The acquisition frequency was 12.5 kHz with automatic averaging over 20 samples to a final frequency of 625 Hz. Using the active-X component LIBADX provided by BMC-Messsysteme, the binary data was converted into ASCII-Format and then imported into MatLab.

Firstly, the data is filtered with a low-pass Butterworth filter, usually with a cut-off frequency of 60 Hz and a filter order of 10. The filtered data is used to find the slip events with a simple peak detection algorithm (peakdet.m by Eli Billauer, public domain). For this a manually determined minimal stress drop is defined for each experiment that serves as input into the peak detection. An event is considered a peak when the value was preceded by a value that is lower by at least the minimal stress drop. This peak detection is refined to remove some local double detections due to noise. An alternative method to detect peaks uses the first derivative of the force measurement and a manually determined stress drop rate. With this detection scheme, several additional points, such as the onset of dynamic failure, can be determined. If slip events are detected in the time series, several statistical parameters are determined to be compared with earthquake statistics. Table A.1 lists all parameters and their definition in this context.

Table A.1: Parameters that are calculated from the time series of a ring shear tester experiment.

Parameter		Equation	Definition
recurrence time	t_{rec}	$t_1 - t_0$	Time difference between the detected peaks.
stress drop	$\Delta\tau$	$\tau_p - \tau_e$	Difference between peak stress τ_p and stress after the slip event τ_e.
duration	t_d	$t_e - t_p$	Time difference between peak stress and stress after slip event
drop velocity	$d\tau$	$\frac{\Delta\tau}{t_d}$	Stress drop rate over the duration of one slip event.
force drop	ΔF	$\frac{\Delta\tau r_m a_d}{r_s}$	Conversion of stress drop to force drop at the force transducers. This uses the convention given by Nextview and Schulze [1994] which uses the median radius r_m and the radius of the lever r_s in combination with the area of the lamellae on the lid a_d.
displacement	$\bar{d}$	$\frac{\Delta F r_s}{k} r_m$	Displacement along the median radius r_m calculated from the force drop at the transducers ΔF and the machine stiffness k.
slip velocity	v	$\frac{\bar{d}}{dt}$	Displacement over the duration of one slip event.
seismic moment	M_0	$\Delta\tau A^{\frac{3}{2}}$	Seismic moment as defined by the stress drop on a specified slip area A. In this case the slip area is defined to be the complete area of the shear cell.
moment magnitude	M_W	$\frac{2}{3} log_{10}(M_0) - 9.1$	Moment release as defined by Kanamori [1978] (M_0 in dyne·cm).
b-value	b	$log_{10} N = a - bM$	Relation of earthquake frequency N and earthquake magnitude M. The b-value is estimated using a maximum likelihood technique [Aki, 1965] and represents the local slope of the earthquake size distribution without the roll-off at low magnitudes and up to a certain corner magnitude.

A.3 Post-processing of digital image correlation

As a first step the individual vector output of the digital image analysis by LaVision DaVis 8 is converted into binary '*.mat'-files. During this step, all vectors outside the area of interest are removed. This reduces the amount of data to be processed, provides faster access to the data and allows for additional results to be stored within the same file for better consistency. Then all relevant properties are extracted from the accessory files that are provided by DaVis, e.g. framerates. For each vector field several statistical properties are acquired, e.g. median displacement, signal-to-noise ratios, or peak displacements.

The digital image correlation algorithm delivers a two-component vector at equally-spaced interrogation points. Each component is the displacement per picture in millimeters, or pixels if the system is not calibrated. The reference coordinate system for the algorithm is a rectangular grid, that overlies the circular experimental domain. As a result the two vector components show the horizontal (v_x) and vertical (v_y) displacement in the image (Figure A.1 A+B). To subtract the background rotation the location of the rotation centre in the vector files has to be estimated.

A reference experiment, consisting only of a rotating plate, is done with the same monitoring setup as the main experiment. The resulting displacement field is analysed with the same parameters as the experiment. This results in the displacement field shown in Figure A.1C. The orientation of the vectors is parallel to the rotation direction and as a result the contours of the orientation map are exactly perpendicular to the rotation direction and point towards the rotation centre of the plane (Figure A.1D). The contour lines are then used to fit linear functions which intersect at the rotation centre. The intersection points for all functions are calculated and the centroid of all points is determined as the rotation centre. If the 95% confidence region of the centroid location is bigger than 2 mm the centroid is picked manually. Once the rotation center is calculated, the data is stored within the script, to avoid variations due to manual picking. The background rotational field is calculated using the loading rate and the rotation center as origin.

To qualitatively compare the fault motion with a natural rectangular fault, the vectors are projected onto a rectangular plane. This is achieved using a Cartesian to polar coordinate transformation with the experimental rotation centre as origin. Afterwards the grid coordinates (x and y) are transferred to polar coordinates θ (angle to x-axis) and ρ (radius):

$$\theta = atan2(y, x) \tag{A.1}$$

$$\rho = \sqrt{x^2 + y^2} \tag{A.2}$$

The resulting grid allows a rectangular representation of the fault surface, but does not allow the calculation of parameters over larger areas because the coordinate transformation is not area preserving. The upper and lower boundary of the projected system have different lengths (Figure A.1.E). In addition, the displacements have to be transformed into the new coordinate system as well. The absolute displacement $|v|$ has to stay the same but the orientation of the vector has to be corrected by the position on the polar grid. Consequently, v_x and v_y are transformed into $|v|$ and angle α using the equations A.1 and A.2 (Figure A.1.C+D). Assuming a perfect circular motion α rotates around the circumference of the setup from 0° to 360°. Subtracting the angle θ from α reorients the vector field to the projected coordinate system. For pure rotation, all

angles α' are now 0°. From the reoriented vector field the new vector components v'_x and v'_y are calculated by:

$$v'_x = |v| \cos \alpha' \tag{A.3}$$

$$v'_y = |v| \sin \alpha' \tag{A.4}$$

Figure A.1 shows the transformation process with a measured example of pure rotation. The transformed vector field for pure rotation should show a linear increase in absolute velocity (Figure A.1E) from the bottom (inner boundary) to the top (outer boundary) and a residual angle of approximately zero (Figure A.1F), which is true for the measured example.

From the projected and unprojected displacement fields the displacements along a profile are extracted using the rotation centre and a calculated circle. The vectors close to the circle are then extracted and interpolated along the circumference.

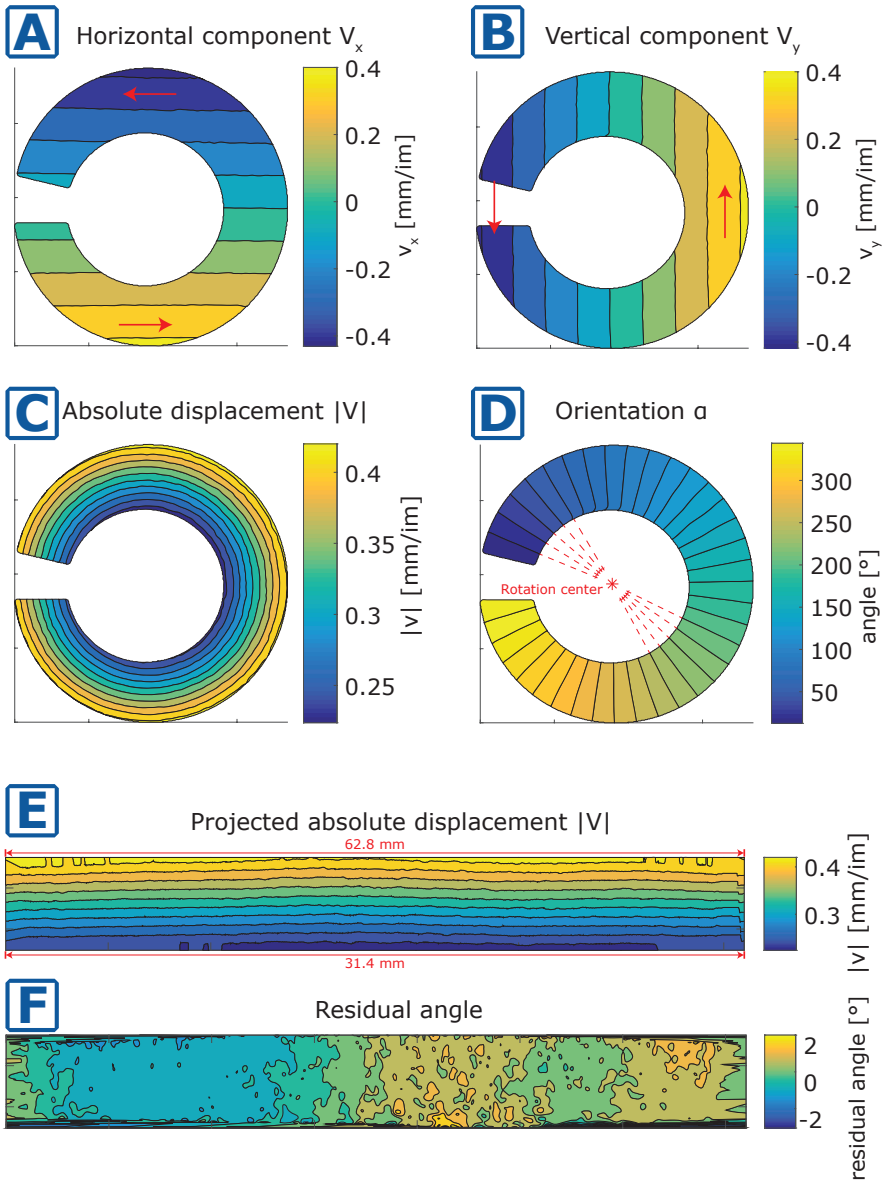

Figure A.1: Vector components derived from a measured reference experiment with a rotating disk of the same size as the setup. (A) and (B) show the two vector components that point in two different directions (±x or ±y). The amplitude increases linearly orthogonal to their direction. (C) shows the value of the absolute displacement that increases from the inner to the outer boundary of the setup. (D) The angle of displacement rotates around the rotation centre which can be approximated as the intersection of all equal-angle contours in the centre of the setup. (E) shows the unwrapped displacement field for the absolute displacement shown in (C). (F) shows the residual orientation of the vectors in the projected coordinate system. It is close to zero within the accuracy of the measurement.

Acknowledgements

I greatly acknowledge the continuous support, ideas and advice of my supervisors – Matthias Rosenau, Karen Leever, Ralf Kornhuber and Onno Oncken. Special thanks go to Frank Neumann and Thomas Ziegenhagen who facilitated the technical realization of this study by constructing and building a lot of different experimental setups. I thank all the guests and frequent visitors to our laboratory, especially Fabio Corbi and Maria Michail, who involved me in many fruitful discussions and gave me inspiration for experiments. I give thanks to all my fellow PhD-students and colleagues at the GFZ-Potsdam and within the framework of the CRC 1114, for countless hours of discussions and fun in the office.

The financial and organizational support of the SFB-1114 'Scaling Cascades in Complex Systems' and the Geo$\sum$im graduate school is acknowledged.

Finally, I want to thank my family and girlfriend for their ongoing support and encouragement.